


A	0 – 20 cm	
Eg	20 – 65 cm	
Bt	65 – 120 cm	
Bg	120 – 160 cm	
Br	> 160 cm	

Hydrological Characterization of a Forest Soil Using Electrical Resistivity Tomography

Christoph Oberdörster

Forschungszentrum Jülich GmbH
Institute of Chemistry and Dynamics of the Geosphere (ICG)
Agrosphere (ICG-4)

Hydrological Characterization of a Forest Soil Using Electrical Resistivity Tomography

Christoph Oberdörster

Schriften des Forschungszentrums Jülich
Reihe Energie & Umwelt / Energy & Environment

Band / Volume 76

ISSN 1866-1793

ISBN 978-3-89336-647-7

Bibliographic information published by the Deutsche Nationalbibliothek.
The Deutsche Nationalbibliothek lists this publication in the Deutsche
Nationalbibliografie; detailed bibliographic data are available in the
Internet at <http://dnb.d-nb.de>.

Publisher and
Distributor: Forschungszentrum Jülich GmbH
Zentralbibliothek
52425 Jülich
Phone +49 (0) 24 61 61-53 68 · Fax +49 (0) 24 61 61-61 03
e-mail: zb-publikation@fz-juelich.de
Internet: <http://www.fz-juelich.de/zb>

Cover Design: Grafische Medien, Forschungszentrum Jülich GmbH

Printer: Grafische Medien, Forschungszentrum Jülich GmbH

Copyright: Forschungszentrum Jülich 2010

Schriften des Forschungszentrums Jülich
Reihe Energie & Umwelt / Energy & Environment Band / Volume 76

D 5 (Diss., Bonn, Univ., 2010)

ISSN 1866-1793
ISBN 978-3-89336-647-7

The complete volume ist freely available on the Internet on the Jülicher Open Access Server (JUWEL) at
<http://www.fz-juelich.de/zb/juwel>

Neither this book nor any part of it may be reproduced or transmitted in any form or by any
means, electronic or mechanical, including photocopying, microfilming, and recording, or by any
information storage and retrieval system, without permission in writing from the publisher.

⁹And God said, "Let the waters under the sky
be gathered together into one place, and let
the dry land appear." And it was so. ¹⁰God
called the dry land Earth, and the waters
that were gathered together he called Seas.
And God saw that it was good.

(Genesis 1:9 - 1:10)

Hydrological Characterization of a Forest Soil Using Electrical Resistivity Tomography

Abstract

An explicit knowledge of soil properties is required in agronomy, nature conservation, and hydrology to characterize water storage and water flow processes, even more in the context of climate change. Electrical resistivity tomography (ERT) has become a more frequently used method in soil science and hydrogeology to obtain this information since the bulk soil electrical conductivity, σ_b , derived from ERT is directly linked to the soil water content, θ .

In this work, a field plot (10 m x 10 m) which was located in a forest on the premises of the Forschungszentrum Jülich (Jülich, Germany) was equipped with 36 boreholes to investigate the soil hydraulic properties of a forest stand by means of ERT.

First, the impact of the ERT data errors on σ_b was analyzed. A synthetic experiment was performed to clarify whether there is a significant difference between inverted ERT data sets once produced from a water saturated soil profile, and once from a drier profile. The related ERT data were noised in the framework of a Monte Carlo approach by means of authentic error distributions derived from field measurements. Different error models were used within the consecutive inversion process. It became obvious that data errors propagated ruthlessly into the final model, leading occasionally to an overlap of resulting σ_b distributions related to dry and wet soil conditions, respectively. The results of this study suggested to evaluate data errors precisely. If possible, data errors should be detected in dependence of the corresponding measurement geometry.

Additionally, a long-term study was performed in the field to monitor changes in soil water content by means of ERT. A period of dewatering was chosen to calibrate the relationship between σ_b obtained from ERT and θ derived from TDR. This petrophysical relationship was used to derive water contents in an ERT image plane for a period of nine months. The plausibility of the imaged spatial distributions of soil water content changes could be verified by different independent measurements (e.g., by TDR). The agreement with those measurement techniques as well as the plausibility of spatial soil water changes caused by root water uptake of the trees demonstrated the additional benefit when a median filter was applied to noisy time-lapse inversion results.

Finally, a saline tracer experiment was performed in order to investigate the transport behavior of the soil. To parameterize solute transport processes, the convection-dispersion equation (CDE) and the mobile-immobile model (MIM) were fitted to ERT and TDR data. Although σ_b derived from ERT was lower than TDR measurements in almost all depths, estimated pore water velocities of the CDE model were very similar. Early peak arrival times at lower depths and long tailings of the breakthrough curves (BTCs) clearly indicated preferential flow phenomena which could not be described with an appropriate parameterization using classical transport approaches such as the CDE. Also the adaption of the MIM model did not lead to more reasonable solute transport parameters. However, typical features of preferential transport could be detected and the spatial variability of the preferential transport process could be imaged by ERT.

Hydrologische Charakterisierung eines Waldbodens mittels Elektrischer Widerstandstomographie

Kurzfassung

Eine genaue Kenntnis der Bodeneigenschaften wird in der Landwirtschaft, Hydrologie und im Naturschutz benötigt, um Wasserspeicherung und Flussprozesse zu charakterisieren, insbesondere im Hinblick auf den fortschreitenden Klimawandel. Die elektrische Widerstandstomographie (ERT) ist eine immer häufiger genutzte Methode in der Bodenkunde und Hydrogeologie, um diese Informationen zu erhalten, denn die von ERT abgeleitete elektrische Leitfähigkeit des Bodens, σ_b , ist direkt abhängig vom Bodenwassergehalt, θ .

In dieser Arbeit wurde ein Versuchsfeld (10 m x 10 m), das in einem Waldgebiet auf dem Gelände des Forschungszentrums Jülich eingerichtet wurde, mit 36 Bohrlöchern ausgestattet, um die bodenhydraulischen Eigenschaften eines Waldbestands mittels ERT zu untersuchen.

Zunächst wurde der Einfluss der ERT-Datenfehler auf σ_b analysiert. Ein synthetisches Experiment wurde durchgeführt, um zu überprüfen, ob ein signifikanter Unterschied zwischen invertierten ERT-Datensätzen besteht, die einerseits von einem wassergesättigten Profil abgeleitet wurden und andererseits von einem trockenerem. Die jeweiligen ERT-Daten wurden im Rahmen eines Monte Carlo Ansatzes verrauscht mittels einer authentischen Fehlerverteilung, die von Feldmessungen abgeleitet wurde. Offensichtlich pflanzten sich die Fehler unmittelbar in das finale Modell fort, was gelegentlich zu einer Überlappung der resultierenden σ_b -Verteilungen unter trockenen beziehungsweise feuchten Bedingungen führen konnte. Die Ergebnisse zeigten, dass es wichtig ist, Datenfehler präzise abzuschätzen. Falls möglich, sollten sie in Abhängigkeit von der jeweiligen Messgeometrie bestimmt werden.

Des Weiteren wurde im Wald eine Langzeituntersuchung durchgeführt, um Änderungen des Bodenwassergehalts mittels ERT zu beobachten. Eine im Testfeld kalibrierte petrophysikalische Beziehung wurde genutzt, um den Wassergehalt in einer von ERT dargestellten Bildebene während eines Zeitraums von neun Monaten darzustellen. Die Plausibilität der räumlichen Wassergehaltsverteilungen konnte durch verschiedene unabhängige Messungen (z.B. durch TDR) verifiziert werden. Die Übereinstimmung mit diesen Messmethoden und die Glaubhaftigkeit der lokalen Bodenwasseränderungen belegt durch die Wurzelaktivität der Bäume zeigte den Mehrwert eines Medianfilters, der genutzt wurde, um die zeitlich rauschenden Inversionsergebnisse zu glätten.

Letztlich wurde ein Tracerversuch mit einer Salzlösung durchgeführt. Zur Parametrisierung der Transportprozesse im Boden wurden die Konvektions-Dispersions-Gleichung (CDE) und das Mobil-Immobil-Modell (MIM) an die ERT- und TDR-Daten gefittet. Kurze Transportzeiten des Konzentrationsmaximums in unteren Tiefen und lange Schwänze der Durchbruchkurven (BTCs) wiesen auf präferenziellen Fluss hin, der nicht mit einer realistischen Parametrisierung durch die Transportmodelle beschrieben werden konnte. Aber es konnte gezeigt werden, dass ERT geeignet ist, um die räumliche Variabilität präferenzieller Transportprozesse darzustellen.

Danksagung

Die vorliegende Dissertation ist das Ergebnis umfangreicher Feld-, Labor- und Auswertearbeiten und konnte nur deshalb erfolgreich abgeschlossen werden, weil mich diverse Personen aktiv unterstützt haben. Auch wenn ich an dieser Stelle nicht alle aufführen kann, so möchte ich einigen dennoch persönlich danken.

Zunächst danke ich Herrn Prof. Dr. H. Vereecken, Leiter des Instituts Agrosphäre (ICG 4) der Forschungszentrum Jülich GmbH für die Übernahme des Referats und die äußerst verbindliche Betreuung. Meinem jetzigen Vorgesetzten Herrn Prof. Dr. A. Kemna, Leiter der Arbeitsgruppe Angewandte Geophysik im Steinmann Institut der Universität Bonn, danke ich für die Übernahme des Korreferats sowie für die Freiheit, auch nach dem Antreten meiner neuen Arbeitsstelle Zeit in die Fertigstellung der Promotion investieren zu dürfen. Weiterhin waren die fachlichen Diskussionen mit ihm sehr fruchtbar. Mein ganz besonderer Dank gilt auch Herrn Prof. Dr. J. Vanderborght (ICG 4), der diese Arbeit konzeptionell gestaltet hat und mich während der gesamten Promotion mit sehr viel Zeit, Fachkompetenz und Verständnis betreut hat.

Außerdem möchte ich Herrn Dr. R. Kasteel meinen Dank aussprechen, der als Verantwortlicher des Bodenphysikalischen Labors die Koordination aller Laboranalysen übernommen hat und mich diesbezüglich auch fachlich beraten hat. Weiterhin danke ich Herrn Dr. A. Graf sowie Herrn Dr. A. Knaps für die unverzichtbare Hilfe bei der Auswertung der Eddy-Kovarianz Messungen. Besonders dankbar bin ich Herrn J. Höltkemeier, der mich von Beginn an in allen technischen Fragen mit seiner väterlichen Art intensiv betreut hat. Außerdem danke ich auch den Ingenieuren bzw. Administratoren F. Engels, J. Heidbüchel, N. Hermes, T. Schuster und A. Weuthen für die vielfältige technische Unterstützung und nicht zuletzt auch für die unterhaltsamen Kaffee- und Mittagspausen. Mein Dank gilt auch Frau A. Langen, Frau O. Esser und Herrn R. Harms für die tatkräftige Hilfe bei den Labor- und Feldarbeiten sowie allen Mitarbeitern des Instituts Agrosphäre für die stets gute Arbeitsatmosphäre.

Den Mitarbeitern der Werksfeuerwehr danke ich für die Beratung zur Durchführung des Beregnungsversuches sowie für diverse Einsätze, um festgefahrene Fahrzeuge zu den unmöglichsten Tageszeiten aus dem Wald zu bergen.

Herrn A. Dickhof vom Geologischen Dienst NRW danke ich für die Hilfe bei der Ansprache des Bodens.

Ein tiefes Anliegen ist es mir, Dr. S. Finsterle und Dr. M.B. Kowalsky zu erwähnen. Während meines dreimonatigen Aufenthalts am Lawrence Berkeley National Laboratory durfte ich sowohl fachliche als auch persönliche Erfahrungen machen, die ich nicht missen möchte und die ich allein ihrem Einsatz zu verdanken habe.

Schließlich möchte ich mich in ganz besonderer Weise bei meiner Familie bedanken. Meine Eltern, Schwestern und deren Partner standen mir in allen Phasen der Arbeit bedingungslos zur Seite und haben mir gegebenenfalls immer wieder Mut zugesprochen. Außerdem danke ich meinem Vater für manche schöne Wanderung, die in der Regel mit einer effektiven Nachhilfestunde in Algebra und Analysis verbunden war. Meinen beiden Neffen bin ich für die „Inspiration“ während der Endphase meiner Promotion dankbar.

Letztlich danke ich der Deutschen Forschungsgemeinschaft (DFG) für die finanzielle Unterstützung.

Contents

1	Introduction.....	1
1.1	Background and State-of-the-Art	3
1.2	Motivation and Structure.....	5
2	Field Site Description	9
2.1	Geology	11
2.2	Experimental Setup	14
3	Theory of Electrical Resistivity Tomography (ERT).....	19
3.1	Measurement Principle.....	21
3.2	Modeling	24
3.2.1	Physical Fundamentals	24
3.2.2	Modeling Concepts	25
3.2.3	The Forward Problem.....	26
3.2.4	The Inverse Problem.....	26
3.2.5	Error Model	28
3.2.6	Robust Inversion	29
3.2.7	Accumulated Sensitivity	30
3.2.8	Temperature Correction	30
4	Characterization of Data Noise and its Implementation in Electrical Resistivity Tomography for Imaging Bulk Electrical Conductivity in the Vadose Zone	33
4.1	Abstract	35
4.2	Introduction	36
4.3	Materials and Methods.....	38
4.3.1	Forward Simulation	38
4.3.2	Generating Noisy Data.....	39
4.3.3	Error Model Dependent on Resistance	44
4.3.4	Error Model Dependent on Electrode Configuration	44
4.3.5	Inversion	45
4.4	Results and Discussion	46
4.4.1	Reproduction of the Earth Model	46

4.4.2	Uncertainty in Resistivity	50
4.4.3	Comparison Between wet and dry Conditions.....	52
4.5	Conclusions	57
5	Determination of Seasonal Water Content Dynamics in a Forest Soil	
	Using Electrical Resistivity Tomography	59
5.1	Abstract	61
5.2	Introduction	62
5.3	Materials and Methods.....	65
5.3.1	ERT Data Processing.....	65
5.3.2	Calibration of Field-Scale Petrophysical Relationship.....	67
5.3.3	Application of Field-Scale Petrophysical Relationship.....	68
5.4	Results and Discussion	76
5.4.1	ERT Data Processing.....	76
5.4.2	Calibration of Field-Scale Petrophysical Relationship.....	81
5.4.3	Application of Field-Scale Petrophysical Relationship.....	86
5.5	Conclusions	101
6	Investigating Preferential Flow Processes in a Forest Soil Using Time	
	Domain Reflectometry and Electrical Resistivity Tomography	105
6.1	Abstract	107
6.2	Introduction	108
6.3	Materials and Methods.....	111
6.3.1	Experimental Setup	111
6.3.2	Data Analysis	113
6.4	Results and Discussion	117
6.5	Conclusions	133
7	Summary and Conclusions	137
8	Bibliography	143

List of Figures

Fig. 2.1:	a) Satellite image of the investigated area (Google Maps, 2009). b) Soil map (German soil classification) of the investigated area (Schalich, 1972).	11
Fig. 2.2:	a) Soil profile classified as Stagnic Luvisol (FAO/ISRIC/ISSS, 1998). b) Profile of soil texture (modified after Linnemann (2001)).....	12
Fig. 2.3:	Borehole and trench positions at the experimental site. Electrodes are numbered for each plane in x-direction. Trees are marked by green circles.	14
Fig. 2.4:	View on trenches 2 and 3 after installation of instrumentation.	16
Fig. 3.1:	a) Current waveform injected for a four-electrode measurement. b) Voltage waveform resulting from current according to a).	22
Fig. 3.2:	Definition of the electrical forward and inverse problems after Binley and Kemna (2005).	25
Fig. 4.1:	Volumetric soil water content, θ , (left) and bulk soil electrical conductivity, σ_b , (right) measured by TDR. Dashed red lines represent dates when profiles were taken to generate an earth model for the synthetic ERT study.	38
Fig. 4.2:	Resulting earth models derived from TDR measurements. TDR positions are indicated by white dots, ERT electrodes by black dots.	39
Fig. 4.3:	Selection of a certain electrode configuration across the first two boreholes (see cut-out in the upper left corner) and recovery within the remaining boreholes.....	40
Fig. 4.4:	Distribution of normal-reciprocal errors for measurements with similar resistance but different geometry.....	41
Fig. 4.5:	Error level dependent on resistance, each point represents one electrode configuration. Red line illustrates the error calculated by the resistance dependent error model Eq. [3.24].	41
Fig. 4.6:	Exemplary histogram of normal-reciprocal errors taken from a certain electrode configuration of 30 data sets, the resulting sample consists of 1690 error values.	42
Fig. 4.7:	Original earth model constructed during wet conditions compared with mean resistivity distributions calculated by non-robust inversion,	

electrode positions are depicted by black dots.	47
Fig. 4.8: Original earth model constructed during wet conditions compared with mean resistivity distributions calculated by robust inversion, electrode positions are depicted by black dots.....	49
Fig. 4.9: Distributions of coefficient of variation (CV) compared with accumulated sensitivity. CV's are depicted again for wet conditions and the non-robust inversion scheme.....	51
Fig. 4.10: Histogram plotted for an exemplary set of model parameters calculated by means of fCEM.	52
Fig. 4.11: Comparison of mean resistivity distributions between dry and wet conditions.	53
Fig. 4.12: Distribution of the relation between the mean resistivities of the dry and wet conditions, ζ	54
Fig. 4.13: Distributions of test statistic τ for different treatments of data sets, results are shown for the non-robust inversion scheme.....	55
Fig. 5.1: Exemplary grid illustrated for plane $y=6$ m. Red dots indicate electrode positions.	67
Fig. 5.2: Relationship between free precipitation rate, P_f , and throughfall, P	70
Fig. 5.3: a) Observation tower for eddy covariance measurements. b) Ultrasonic anemometer and open path analyzer mounted on top of the tower.....	71
Fig. 5.4: Time series of evapotranspiration flux, ET , derived from eddy covariance measurements in the period June 2006 to April 2007.....	72
Fig. 5.5: Error distribution derived from normal-reciprocal measurements for a certain electrode configuration: C1: 20, C2: 23, P1: 35, P2: 39 in plane $y=0$ (n=72) a); $y=6$ m (n=82) b); $y=10$ m (n=72) c).....	77
Fig. 5.6: Robust estimated standard deviation of normal-reciprocal error, $\sigma(\Delta \ln R)$, in dependence on geometric factor, K , in plane $y=0$ a); $y=6$ m b); $y=10$ m c).....	79
Fig. 5.7: Robust estimated standard deviation of normal-reciprocal error, $\sigma(\Delta \ln R)$, in dependence on the inverse of mean resistance, R^{-1} , in plane $y=0$ a); $y=6$ m b); $y=10$ m c).....	80
Fig. 5.8: Calibration of the CEM model.	82
Fig. 5.9: Calibration of the REM model.	85
Fig. 5.10: Median of filtered water content from ERT with CEM, $\theta_f^{ERT_{CEM}}$, compared with median of filtered water content from ERT with REM, $\theta_f^{ERT_{REM}}$	87
Fig. 5.11: Plots of θ_f^{TDR} versus θ_f^{ERT} obtained from inversions with CEM model at	

different depths in the soil profile.....	89
Fig. 5.12: Plots of θ_f^{TDR} versus θ_f^{ERT} obtained from inversions with REM model at different depths in the soil profile.....	90
Fig. 5.13: Cumulative height of supplied water at the upper bound, PET , and cumulative change in height of water in the soil, H , drawn from both ERT (H^{ERT}) and TDR (H^{TDR}).	93
Fig. 5.14: a) Throughfall during the investigated period. b) Change in filtered water content derived from ERT for plane $y=6$ m. c) Peak velocities, v_p , derived from a tracer experiment (chapter 6).	96
Fig. 5.15: Water balance during the passage of the rainstorm.....	97
Fig. 5.16: a) Cumulative height of supplied water at the upper bound, PET , and depth to groundwater table, GWL , taken over from Fig. 5.13. b) Soil water content changes in the period between June 2006 and September 2006 for plane $y=6$ m with respect to a background taken at 2006/06/13.	98
Fig. 5.17: Soil water content changes in the period between October 2006 and March 2007 for plane $y=6$ m with respect to a background taken at 2006/06/13.	100
Fig. 6.1: Overview of field site with installed trenches, sprinklers, and irrigated area.	111
Fig. 6.2: a) Dipole-dipole configuration taken for the ERT measurements. C1, C2 denote current electrodes separated in two boreholes, and P1, P2 potential electrodes within one borehole. b) Experimental setup of the tracer experiment.	112
Fig. 6.3: Mean flux density, q_f , of tracer and tap water irrigation, respectively. Pentagrams denote rain gauges, open circles sprinklers, and closed circles trees.	113
Fig. 6.4: Measured tracer breakthrough (symbols) derived from TDR and ERT. ERT values are taken from grid elements next to TDR probes. Lines indicate CDE model fits.	118
Fig. 6.5: Measured tracer breakthrough (symbols) derived from TDR and ERT, respectively. ERT conductivities are averaged values calculated from all grid elements of the respective depth. Range between 5 th and 95 th percentiles is plotted as shaded area. Lines indicate CDE model fits.	120
Fig. 6.6: a) Linear regression between peak velocities, v_p , derived from ERT and TDR, respectively. Noisy TDR data in a depth of 0.84 cm are omitted. b) Depth profile of peak velocities, v_p , derived from ERT and TDR,	

	respectively. Shaded area denotes Bt horizon.	122
Fig. 6.7:	Measured tracer breakthrough (open circles) derived from ERT. Conductivities are averaged values calculated from all grid elements of the respective depth. Solid lines represent fits of the CDE model, dashed lines fits of the MIM model, where pore water velocity is fixed to piston flow velocity.....	124
Fig. 6.8:	Depth profile of mass transfer coefficient, α , taken from Tab. 6.2. Shaded area denotes the Bt horizon.	126
Fig. 6.9:	Measured resident concentrations (open circles) and flux concentrations predicted by CDE and MIM models that were fitted to resident concentrations. Concentrations are expressed in terms of σ_b , resident concentrations are denoted by index “r”, flux concentrations by index “f”.	127
Fig. 6.10:	a) Corrected mean peak conductivity, $\sigma_{b,p} - \sigma_{b,in}$, and its 10 th and 90 th percentiles, indicated by P10 and P90, respectively. Thick black line represents a reference illustrating a decrease with $1/z^{0.5}$. b) Mean peak velocity, v_p , and its 10 th and 90 th percentiles, indicated by P10(v_p) and P90(v_p), respectively. Piston flow velocity, v_q , is shown for comparison.....	129
Fig. 6.11:	Two-dimensional distributions of corrected peak electrical conductivities, $\sigma_{b,p} - \sigma_{b,in}$, (left) and peak velocities, v_p , (right). v_p related to $\sigma_{b,p} - \sigma_{b,in} < 8.4 \cdot 10^{-4} \text{ S m}^{-1}$ (denoted by σ_t in the left colorbar) are blanked out. Mean piston flow velocity ($v_q = 22 \text{ cm d}^{-1}$) is marked in the right colorbar. Maps are shown exemplary for planes in x-direction. Black dots represent electrode positions, Bt horizon is denoted by red lines.....	131

List of Tables

Tab. 2.1: Soil physical properties of the profile estimated from undisturbed soil samples (100 cm ³): geometric mean of saturated hydraulic conductivity, \tilde{k}_s , related variance, $s^2(\ln(k_s))$, dry bulk density, $\rho_{d,b}$, and porosity, Φ . $\rho_{d,b}$ and Φ are calculated from sample weights after wetting and drying.....	13
Tab. 2.2: Depths of different measurement devices.	15
Tab. 5.1: Derivation of compartment thickness, Δz_ω , for the derivation of the water balance.	74
Tab. 5.2: Robust estimated standard deviations from error distributions according to Fig. 5.5 calculated for different planes, $\sigma(\Delta \ln R_{\text{examp}})$. $\bar{\sigma}(\Delta \ln R)$ and $std(\sigma(\Delta \ln R))$ are mean and standard deviation of robust estimators of all configurations in the given plane.....	78
Tab. 5.3: Parameterization according to error model (REM) given in Eq. [3.24] for different planes.	81
Tab. 5.4: Parameters, a and b , of a linear petrophysical relationship and related correlation coefficients, r_c , between θ_f^{ERT} and θ_f^{TDR} taken during the calibration period.	84
Tab. 5.5: Correlation coefficient, r_v , between θ_f^{ERT} and θ_f^{TDR} taken during the validation period and normalized root mean square error, $RMSE$, for each depth.	88
Tab. 6.1: Flow velocities: piston flow velocity, v_q , peak velocity, v_p , and fitted CDE parameters: pore water velocity, v , dispersion coefficient, D , and the input conductivity, $[\sigma_{b,0} - \sigma_{b,in}] t_0$, derived from ERT and TDR measured BTCs at different depths, z	121
Tab. 6.2: CDE (v pore water velocity, D dispersion coefficient, and $[\sigma_{b,0} - \sigma_{b,in}] t_0$ input conductivity) and MIM transport parameters (D dispersion coefficient, $[\sigma_{b,0} - \sigma_{b,in}] t_0$ input conductivity, α mass transfer coefficient, and β relative mobile water content) derived from fits to average BTCs at different depths, z , obtained with ERT. For the MIM model, v was not fitted but fixed to piston flow velocity.	125

List of Symbols

Abbreviations

BTC	Breakthrough Curve
CDE	Convection Dispersion Equation
CEM	inversion with error model dependent on electrode configuration
ERT	Electrical Resistivity Tomography
f	based on flux concentrations
fCEM	equal to CEM but using filtered data
FE	finite element
fREM	inversion with error model dependent on resistance using filtered data
IQR	interquartile range
MIM	Mobile-Immobile Model
r	based on resident concentrations
RMS	root mean square
RMSE	root mean square error
TDR	Time Domain Reflectometry

Symbols

a	slope of linear petrophysical relationship [m S^{-1}]
a_e	relative error parameter [-]
a_{ij}	matrix element
b	intercept of linear petrophysical relationship [-]
b_e	absolute error parameter [Ω]
\mathbf{b}_q	right hand sight vector
\mathbf{B}_q	matrix in the inverse problem
C	resident concentration [g cm^{-3}]
C_0	input concentration [g cm^{-3}]
C_b	salt tracer concentration [g cm^{-3}]
$C(t)$	resident concentration at time t [g cm^{-3}]
C_{im}	resident concentration of immobile pore water [g cm^{-3}]
C_{in}	background concentration [g cm^{-3}]

C_m	resident concentration of mobile pore water [g cm^{-3}]
$CV(RMSE)$	normalized root mean square error of θ_f^{ERT} [$\text{cm}^3 \text{cm}^{-3}$]
CV_i	coefficient of variation of voltage trace [-]
d	data vector
D	dispersion coefficient [$\text{cm}^2 \text{d}^{-1}$]
D_{im}	dispersion coefficient of immobile pore water region [$\text{cm}^2 \text{d}^{-1}$]
D_m	dispersion coefficient of mobile pore water region [$\text{cm}^2 \text{d}^{-1}$]
e_i	normal-reciprocal error of i -th datum
E	electric field strength with $[E_i]=[\text{V m}^{-1}]$
ET	evapotranspiration flux [cm h^{-1}]
f	forward operator
f_T	temperature correction factor [-]
F_c	net vertical flux of trace gases [$\text{g cm}^{-2} \text{h}^{-1}$]
GWL	depth to groundwater table [cm]
h	number of measurement time of soil data
H	cumulative change in soil water content [cm h^{-1}]
H^{ERT}	cumulative change in soil water content derived from ERT [cm h^{-1}]
H^{TDR}	cumulative change in soil water content derived from TDR [cm h^{-1}]
I	electric current [A]
j	electric current density with $[j_i]=[\text{A m}^{-2}]$
J_q	Jacobian matrix
k	wavenumber
\tilde{k}_s	geometric mean of saturated hydraulic conductivity [cm d^{-1}]
K	geometric factor [m]
m	model vector
m₀	starting model
M	number of elements
n	outward normal
N	number of measurements
p	number of measurement time of atmospheric data
P	throughfall [cm h^{-1}]
P_f	free precipitation rate [cm h^{-1}]
PET	cumulative height of supplied water at the upper boundary [cm h^{-1}]
q	Gauss-Newton iteration index
q_f	irrigation rate [cm d^{-1}]

Q	electrical charge density [C m^{-3}]
Q_{25}	lower quartile, i.e., 25 th percentile
Q_{75}	upper quartile, i.e., 75 th percentile
r_c	correlation coefficient for linear petrophysical relation during calibration
r_p	correlation coefficient between P_f and P
r_v	correlation coefficient for linear petrophysical relation during validation
R	electrical resistance [Ω]
R_K^2	coefficient of determination for linear error model dependent on K
R_{nor}	normal electrical resistance [Ω]
R_r^2	coefficient of determination for linear error model dependent on R^{-1}
R_{rec}	reciprocal electrical resistance [Ω]
$s^2(\ln(k_s))$	variance of log transformed saturated hydraulic conductivity
s_j	element of sensitivity vector
std	sample standard deviation of sample standard deviations
t	time [s]
t_0	tracer pulse application time [s]
t_p	peak arrival times [d]
T_s	soil temperature [$^{\circ}\text{C}$]
v	pore water velocity [cm d^{-1}]
v_{\max}	tracer velocity based on first arrival time [cm d^{-1}]
v_p	peak velocity [cm d^{-1}]
v_q	piston flow velocity [cm d^{-1}]
\bar{V}^+	mean voltage of positive injection [V]
\bar{V}^-	mean voltage of negative injection [V]
V_{sp}	self-potential voltage [V]
w	vertical wind speed component [cm h^{-1}]
\mathbf{W}_d	data weighting matrix
x	first Cartesian coordinate [m]
\mathbf{x}	position vector
\mathbf{x}_c	position vector of current source
y	second Cartesian coordinate [m]
z	third Cartesian coordinate [m]
z_{ω}	depth of TDR probe [cm]
Z	number of depth intervals

α	first-order mass transfer coefficient [d ⁻¹]
α_c	slope of linear concentration model [m S ⁻¹]
α_r	regularization parameter
α_T	temperature coefficient [(°C) ⁻¹]
β	relative water content of mobile pore water region [-]
β_c	intercept of linear concentration model [-]
δ	Dirac delta function
∇_{2D}	two-dimensional nabla operator
Δz_ω	thickness of the depth interval [cm]
ε_i	standard deviation of i -th datum
ε^{RMS}	root mean square error in geoelectrical modeling
ζ	factor of change in resistivity [-]
θ	soil water content [cm ³ cm ⁻³]
θ^{ERT}	soil water content derived from ERT [cm ³ cm ⁻³]
θ_f^{ERT}	filtered soil water content derived from ERT [cm ³ cm ⁻³]
$\theta_f^{ERT_{CEM}}$	filtered soil water content derived from ERT with CEM [cm ³ cm ⁻³]
$\theta_f^{ERT_{REM}}$	filtered soil water content derived from ERT with REM [cm ³ cm ⁻³]
θ_m	soil water content of mobile pore water region [cm ³ cm ⁻³]
θ_{im}	soil water content of immobile pore water region [cm ³ cm ⁻³]
θ^{TDR}	soil water content derived from TDR [cm ³ cm ⁻³]
θ_f^{TDR}	median filtered soil water content derived from TDR [cm ³ cm ⁻³]
$\theta_{\omega,0}$	initial soil water content of the ζ^{th} depth interval [cm ³ cm ⁻³]
$\theta_{\omega,h}$	water content at the h^{th} time and in the ω^{th} depth interval [cm ³ cm ⁻³]
λ	boundary parameter [-]
μ	order of median filter
Π	number of calibration datasets
ρ_a	apparent resistivity [Ω m]
ρ_b	bulk electrical resistivity [Ω m]
$\bar{\rho}_b^d$	mean resistivity of dry conditions [Ω m]
$\bar{\rho}_b^w$	mean resistivity of wet conditions [Ω m]
ρ_c	trace gas density [g cm ⁻³]
$\rho_{d,b}$	dry bulk density [g cm ⁻³]
ρ_w	density of water, 1 g cm ⁻³
σ	sample standard deviation

XX

σ^2	sample variance
σ_b	bulk electrical conductivity [S m^{-1}]
$\sigma_b(t)$	resident bulk electrical conductivity at time t [S m^{-1}]
$\sigma_{b,0}$	input bulk electrical conductivity [S m^{-1}]
$\sigma_{b,in}$	background bulk electrical conductivity [S m^{-1}]
σ_b^{ERT}	bulk electrical conductivity derived from ERT [S m^{-1}]
$\sigma_{b,f}^{ERT}$	median filtered bulk electrical conductivity derived from ERT [S m^{-1}]
σ_t	threshold electrical conductivity [S m^{-1}]
$[\sigma_{b,0} - \sigma_{b,in}] t_0$	input electrical conductivity [$\text{S m}^{-1} \text{ d}$]
τ	test statistic [-]
φ	electric potential [V]
$\tilde{\varphi}(x, k, z)$	transformed electric potential [V]
Φ	soil porosity [$\text{cm}^3 \text{ cm}^{-3}$]
$\chi_{i,q}$	individual data misfit
$\Psi(\mathbf{m})$	cost function
$\Psi_d(\mathbf{m})$	data misfit term
$\Psi_m(\mathbf{m})$	roughness term
ω	index of soil depth interval

1 Introduction

1.1 Background and State-of-the-Art

Accurate knowledge of soil water content is extremely important for agriculture, forestry, and environmental sciences. In arid regions agricultural production has to be performed as efficient as possible to conserve water and to prevent salinization in consequence of irrigation. In environmental sciences information about soil water content is requested to save nature protection areas and to understand natural processes. In all fields climate change plays a major role in presence and future. Therefore, a detailed measurement of soil water content is crucial to determine the status quo and to feed forecasting models.

First reliable soil moisture measurements were performed in the early 1980s by means of time domain reflectometry (TDR) (Topp et al., 1980). Advantage of this technique is its high accuracy due to the fact that the measured dielectric permittivity is directly related to the soil water content. Furthermore, measurements can be taken in a high temporal resolution. However, to obtain information in a high spatial resolution or even more dimensional, many probes are required. This is not only difficult to manage but also very cost-intensive. Finally, the sample grid is still very coarse. Therefore, ground penetrating radar (GPR), which is based on the same measurement principle as TDR, showed to be very useful to perform a dense mapping of soil water contents at the field scale (Huisman et al., 2003). Additionally, geoelectrical methods were adapted in soil science. Actually, geoelectrics was applied in geophysics and geology to determine petroleum reservoirs by means of the identification of different electrical conductivities occurring in the subsurface. Due to the fact that the soil also consists of conducting materials (e.g., electrolytes) and isolating materials (e.g., air), it is obvious that those techniques are also applicable in the field of soil physics. First of all, geophysicists and soil physicists investigated the electrical properties of rock and soil cores by means of so-called four-electrode methods (Nadler, 1982; Daily et al., 1987). Here, two electrodes are used to inject a current and two further to measure the resulting potential difference. With the aid of these quantities, the apparent electrical resistivity or its inverse, the apparent electrical conductivity, can be calculated. This method was also applied at the field scale. Much more electrodes and sophisticated inversion algorithms enhanced the spatial resolution of this technique in the last years. Therefore, those multi electrode measurements are called electrical resistivity tomography (ERT). The disadvantage of ERT compared to GPR is that the measured resistance is not only dependent on the soil water

content but also on other soil properties such as electrical conductivity of the soil solution. Therefore, monitoring of soil water content by means of ERT requires a constant (or well-known) conductivity of the soil solution. One advantage of ERT is its applicability in areas where barriers are present (e.g., forests). Hence, resistivity methods were applied at the field scale by several authors to monitor infiltration tests (Daily et al., 1992; Park, 1998; al Hagrey and Michaelson, 1999) or natural changes in soil water content (Zhou et al., 2001; 2002; Michot et al., 2003).

Although already claimed as disadvantage, the sensitivity to the salt concentration of the soil is also advantageous to observe tracer experiments by means of ERT. Due to the impact of the soil water variation, it has to be taken care that steady state conditions are reached within the soil profile before the tracer is applied. Information obtained from tracer experiments is valuable to describe the transport behaviour of solutes as well as to demonstrate preferential flow. Conclusions derived from those experiments are highly relevant in terms of soil and groundwater pollution. Therefore, tracer experiments were investigated by means of ERT to describe solute transport processes at the laboratory scale (Binley et al., 1996; Slater et al., 2002; Köstel et al., 2009) as well as at the plot to field scale (Kemna et al., 2002; Looms et al., 2008).

1.2 Motivation and Structure

In the previous sub-section it was already outlined that there is a demand to determine soil water content and soil structure in several disciplines. The cited studies confirm that ERT is an appropriate means to cope with those requirements. However, investigations were rarely conducted at the larger scale and if they were, they focussed more on the deeper subsurface than on a good resolution within the soil. Additionally, long-term observations of the soil can be found only rarely since they are cost-intensive, difficult to manage, and exhausting for the measurement equipment as well as for the staff. Hence, the aim of the current study was to perform long-term ERT measurements at a relatively large scale. Furthermore, previous studies concentrated on simpler systems such as sandy soils or soils with low small scale variabilities. Therefore, the current investigation of a forest stand was challenged by a heterogeneous soil profile and also various anomalies caused by the tree roots. However, special emphasis was placed on a quantitative consideration, consisting of an accurate description of errors, reliable calibrations, and precise comparisons with independent techniques. Finally, the versatile facilities of ERT should be utilized comprehensively, i.e., by description of hydrological soil properties as well as of solute transport properties. Those requirements led to the following structure of the present manuscript:

In chapter 2 the site is described where the field measurements were performed. First of all, the geology is treated and the soil profile is classified. After that, the installation and dimensions of the different measurement techniques are introduced. In chapter 3 the theory of ERT is explained. The measurement principle, data acquisition, and further data processing such as inversion are shortly demonstrated. Chapter 4 to 6 are the essential parts of the thesis: When the first ERT field measurements were analyzed, it was obvious that it had to be dealt with considerable data errors in the future. Hence, chapter 4 addresses the statistical description of data errors and a synthetic experiment which proves whether ERT is capable to distinguish between dry and wet conditions in the soil given that high level of noise. In this framework, a new approach is developed to calibrate an error model which is needed for the geophysical inversion. Amongst another, this approach is tested by real data in chapter 5 where the monitoring of soil water contents during a period of nine months in 2006/2007 is analyzed: After a calibration of the petrophysical relationship water contents are derived from ERT and benchmarked by

means of several approaches. ERT based water contents are compared with those obtained from TDR and a water balance is established where the counterpart to soil water measurements is given by rain and evapotranspiration measurements. Additionally, the suitability of ERT to observe a single rain event, which occurred during the passage of a hurricane in January 2007, is analyzed. This low pressure area was termed “Kyrill” by the responsible institution (Institute of Meteorology, Freie Universität Berlin) and it became well-known due to the extensive deletion of forest stands in Europe. To utilize the sensibility of ERT to changes of ion concentration in the soil solution, chapter 6 focuses on a tracer experiment which was conducted in April 2008. On the one hand, the breakthrough curves obtained from ERT are again compared with TDR measurements. On the other hand, soil transport parameters are derived for 2D sections to demonstrate the imaging facilities of ERT at the field scale. In chapter 7 the results of all previous chapters are summarized and the overall conclusions are drawn.

2 Field Site Description

2.1 Geology

The investigated forest site (50°54'42.57"N, 6°24'45.33" E) is located on the premises of the Forschungszentrum Jülich in Jülich, Germany. The main tree species are beech (*Fagus sylvatica* L.), oak (*Quercus robur* L.), and birch (*Betula pendula* Roth). From the geographical perspective, this area belongs to the macrochore “Niederrheinische Bucht“, which is a wedge-shaped branch of the Northern Lowlands of Germany. This landscape is in its southern part surrounded by a low mountain range, the Rhenish Slate Mountains. Geologically, the investigated area is located on the upper part of a massif called “Rurscholle“ and within the river “Rur“ basin, respectively. At the next smaller scale, the area of interest is contained by the “Rur“ river itself in the South, and by the “Ellebach“ creek in the North which finally empties into the “Rur“ (Fig. 2.1).

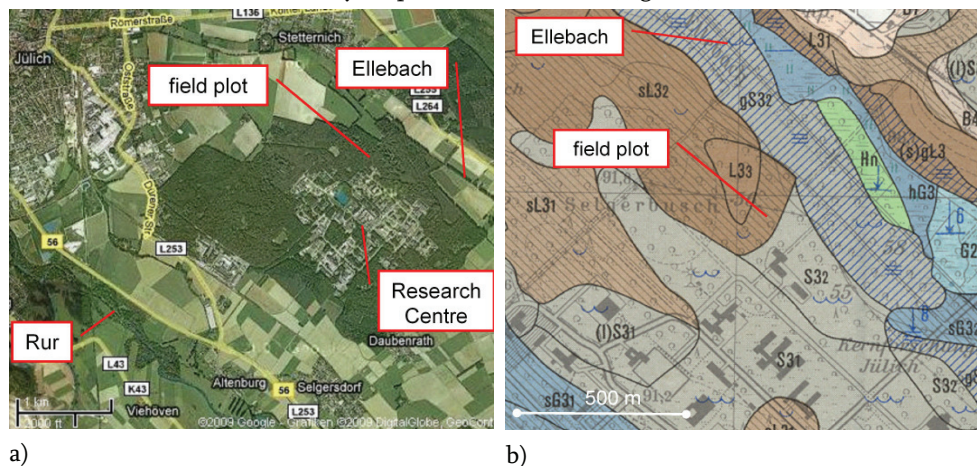


Fig. 2.1: a) Satellite image of the investigated area (Google Maps, 2009). b) Soil map (German soil classification) of the investigated area (Schalich, 1972).

Loose translation to FAO classification (FAO/ISRIC/ISSS, 1998): brown → Luvisol; blue, grey → Gleysol; green → Histosol.

The elevation of the plot is 90.0 m above sea level and the mean groundwater depth amounts 87.5 m above sea level, fluctuating between 2.0 m and 2.8 m below surface. The yearly average precipitation is 698 mm and mean temperature 9.9 °C.

The formation of recent soils in the “Niederrheinische Bucht” can be traced back to the end of the last cold stage “Weichsel” of the later glacial period when loess was deposited on the top surface as an eolian sediment (Paas and Schalich, 2005). During periglacial periods, the loess layer was relocated depending on the inclination of the landscape. An evidence for this phenomenon are small pebbles of the relictic bedrock which have been mixed in the soil above.

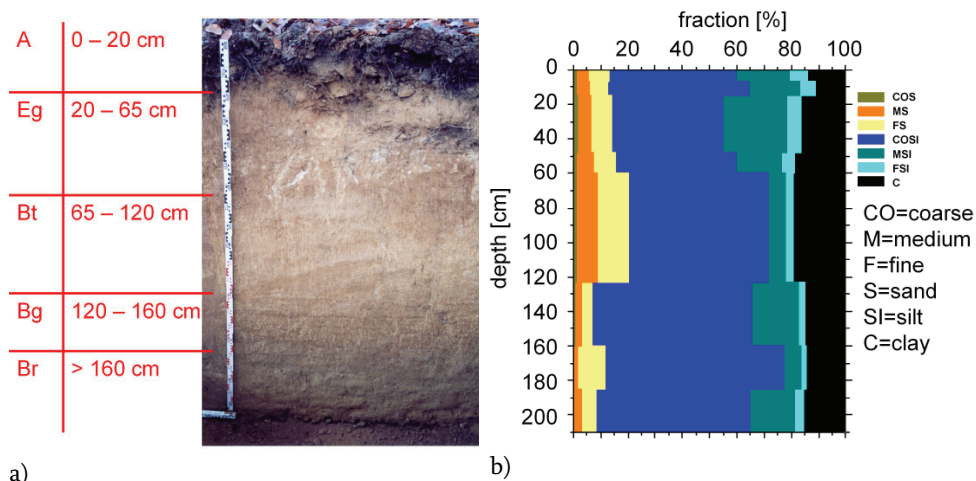


Fig. 2.2: a) Soil profile classified as Stagnic Luvisol (FAO/ISRIC/ISSS, 1998). b) Profile of soil texture (modified after Linnemann (2001)).

The soil profile (Fig. 2.2a) can be divided into five characteristic horizons which diagnostic properties lead to the classification as a Stagnic Luvisol (FAO/ISRIC/ISSS, 1998).

a) At the top, an A horizon can be found (0–20 cm) which is identified by an accumulation of organic matter. The structure can be described as crumbly at the top and more coherent at the basis of the horizon.

b) Weathering and washout led to lessivage and depletion of clay into the subsoil (supported by low clay contents of 10–16 %, Fig. 2.2b). This causes a frequent ponding in this Eg horizon (20–65 cm) which is transparent by mottling effects. The texture is dominated by loamy silt and a clay content of about 15 %, the structure is subprismatic.

c) Accumulation of clay from the horizons above characterizes the Bt horizon (65–120 cm) with a higher bulk density (Tab. 2.1). Here, the mean texture changes to silty loam due to an increased clay content of about 20 %. The structure is still subprismatic.

d) In a depth of 120–160 cm, gleyic properties (Bg horizon) are evident. Here, variations of the groundwater level cause alternating effects of oxidation and reduction, indicated by mottling with manganese and iron concretions, respectively. The texture of those

horizons is now again described by loamy silt and a clay content of about 15 %. The structure is coherent.

e) Strong reduction as a result of groundwater influence is existent in a depth below 160 cm, related to a Br horizon. Anyway, observations of a nearby well provided a mean groundwater level in a depth of about 250 cm. This discrepancy can be explained by a drawdown of groundwater for the last decades due to the activities of a nearby opencast pit.

Below a depth of 200 cm, the profile is formed by compacted sandy gravel of the main terrace of the “Rhine” river system. Detailed information about soil physical properties can be taken from Tab. 2.1 and from Fig. 2.2b, respectively.

Tab. 2.1: Soil physical properties of the profile estimated from undisturbed soil samples (100 cm³): geometric mean of saturated hydraulic conductivity, \tilde{k}_s , related variance, $s^2(\ln(k_s))$, dry bulk density, $\rho_{d,b}$, and porosity, Φ . $\rho_{d,b}$ and Φ are calculated from sample weights after wetting and drying.

sample depth [cm]	10	50	100	<i>not sampled</i>	200
related horizon	A	Eg	Bt	Bg	Br
horizon depth [cm]	0 – 20	20 – 65	65 – 120	120 – 160	> 160
no. of samples	9	9	35	-	15
\tilde{k}_s [cm d ⁻¹]	124.90	67.05	3.17	-	22.60
$s^2(\ln(k_s))$	0.85	0.69	5.15	-	6.50
$\rho_{d,b}$ [g cm ⁻³]	0.996	1.565	1.649	-	1.717
Φ [cm ³ cm ⁻³]	0.35	0.36	0.33	-	0.25
clay content* [%]	12	15	20	14	15
depth of TDR probes [cm]	5 7.5 14	24 44	84	124	184

* after Linnemann (2001)

2.2 Experimental Setup

Within the test plot of 10 by 10 m there are 36 boreholes, each of 2.84 m depth and equipped with 16 stainless steel electrodes (Fig. 2.3). Although it is common to backfill the space between electrode sticks and soil with conductive material this can lead to artifacts in the final image reconstruction (Nimmer et al., 2008). Hence, there was no backfilling performed after drilling. Since beginning of June 2005 ERT measurements were conducted by means of a dipole-dipole array (in-hole and cross-hole), since January 2006 additionally with reciprocal measurements.

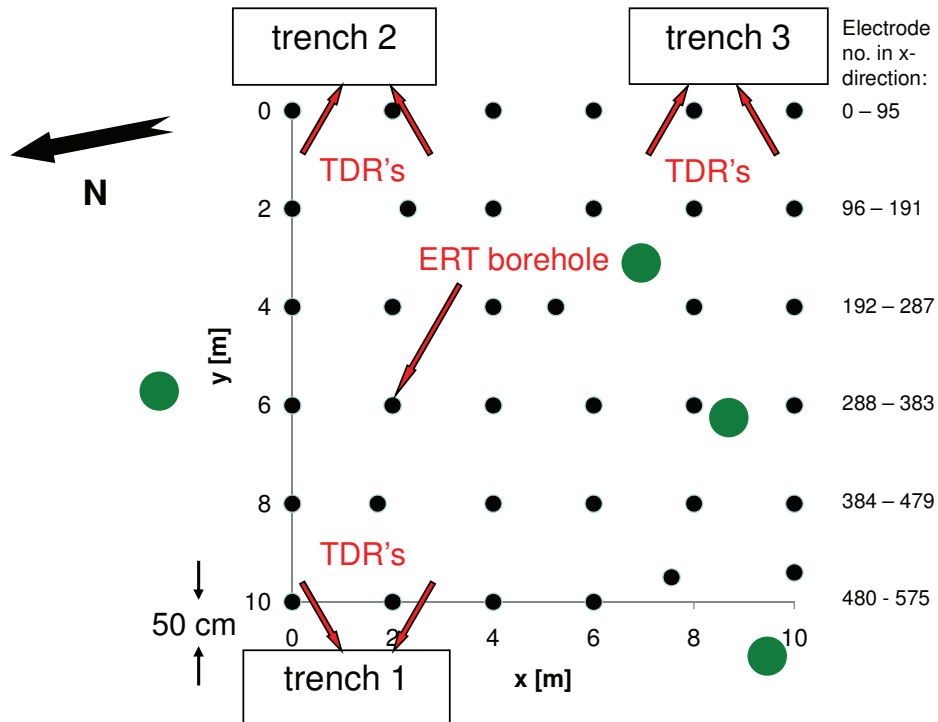


Fig. 2.3: Borehole and trench positions at the experimental site. Electrodes are numbered for each plane in x-direction. Trees are marked by green circles.

The current and voltage dipole lengths, respectively, amounted 0.56 m at the top and increased to 1.64 m at the bottom in order to increase the signal strength. Electrode

switching and data acquisition were performed with the eight channel RESECS instrument provided by GeoServe (Kiel, Germany). At three corners of the plot, trenches were dug (Fig. 2.3). Each trench wall was 50 cm distant from the ERT plot and equipped with sixteen TDR probes. These were arranged in two transects, each consisting of eight probes. TDR probes consisted of three rods with a length of 30 cm, an inter rod distance of 3 cm, and a rod diameter of 0.3 cm. Translation of dielectric permittivity to soil water content was accomplished using the relationship proposed by Topp et al. (1980). The depths of the TDR probes and of the ERT electrodes in each borehole can be taken out of Tab. 2.2.

Tab. 2.2: Depths of different measurement devices.

depth [cm]	ERT electrodes	TDR probes	pF- meters	Temp. probes	suction samplers
5		•			
7.5	•	•	•	•	•
14	•	•			
24	•	•	•	•	•
34	•				
44	•	•	•	•	•
64	•				
84	•	•	•	•	•
104	•				
124	•	•	•	•	
144	•				
164	•				
184	•	•	•	•	•
204	•				
224	•				
254	•				
284	•				

Additional soil physical measurements were taken in different depths (Tab. 2.2): Each vertical trench wall was equipped with 5 suction samplers and 6 pF-meters with integrated temperature probes (or tensiometers with separate temperature sensors in trenches 2 and 3) in different depths (Tab. 2.2).

To prevent lateral water flow into the disturbed trench domain, a plastic foil was pulled along the trench wall before the trench was refilled with soil. Soil physical data acquisition was carried out hourly. A completed installation of the trenches 2 and 3 before

refilling can be seen in Fig. 2.4. During the excavation of trenches of 2 and 3, 3 levels were constructed opposite to the trench wall in 50 cm, 100 cm, and 200 cm depth, respectively. Each level was characterized in the laboratory by means of several undisturbed and disturbed soil samples (no. of undisturbed samples per depth: 100 cm³ cores: 10 cm: 12; 50 cm: 16; 100 cm: 33; 200 cm: 30; 567 cm³ cores: 10 cm: 3; 50 cm: 2; 100 cm: 4; 200 cm: 3).



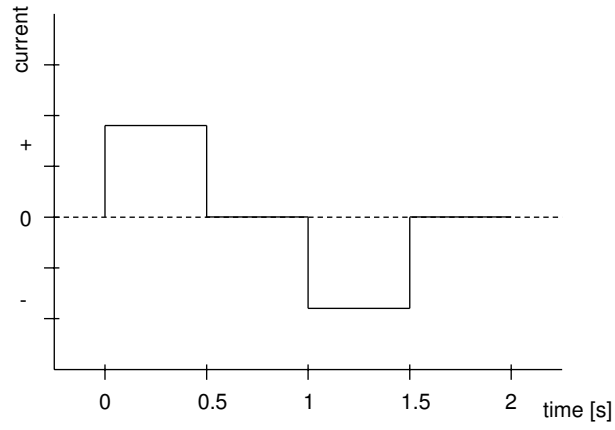
Fig. 2.4: View on trenches 2 and 3 after installation of instrumentation.

3 Theory of Electrical Resistivity Tomography (ERT)

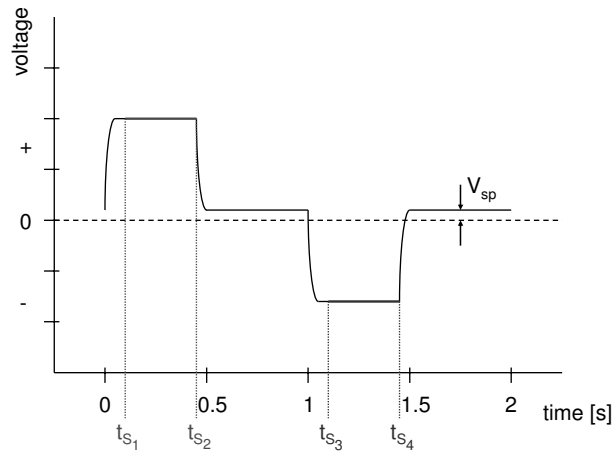
3.1 Measurement Principle

Applying ERT implies the use of at least four (commonly stainless steel) electrodes which are buried in boreholes or installed at the surface. Two electrodes (C1, C2) are needed to inject a current and two electrodes (P1, P2) to measure the resulting potential difference. According to Ohm's law the resistance can be calculated from the ratio between the injected current and the measured voltage. If the measurement geometry is also taken into account, an apparent resistivity, ρ_a , can be calculated which represents that resistivity which a fictitious homogeneous (half-)space would have to produce the same potential difference. Inverse modeling (described later) can then be used to calculate the "true" bulk electrical resistivity, ρ_b , or its inverse, the "true" electrical conductivity, σ_b , for the given parameterization.

For the measurement a direct current (DC) is used that typically has the shape of a square wave, meaning that first a positive current pulse is injected and afterwards a negative (polarity change of current electrodes) (Fig. 3.1a). In between, the current is switched off to reduce polarization effects at the electrodes. According to the injected current, an electric potential field is created and the measurement between two potential electrodes results in a voltage trace which shows a response similar to the current waveform (Fig. 3.1b). However, this voltage adds to a possible self-potential voltage, V_{sp} , which is the background voltage of the investigated system. This offset is taken into account when the polarity of the current is switched. Additionally, the resulting voltage is not established instantaneously due to capacitance effects caused by polarization mechanisms at the fluid-grain interfaces of the soil. Therefore, voltage measurements are delayed and only recorded between times t_{s_1} and t_{s_2} for positive injection and between times t_{s_3} and t_{s_4} for negative injection (Fig. 3.1b).



a)



b)

Fig. 3.1: a) Current waveform injected for a four-electrode measurement. b) Voltage waveform resulting from current according to a).

t_{s1} , t_{s2} and t_{s3} , t_{s4} represent time limits of positive and negative voltage sampling, respectively.

The mean voltages of positive injection, \bar{V}^+ , and of negative injection, \bar{V}^- , are calculated from the trace with

$$\bar{V}^+ = \frac{1}{S_2 - S_1} \sum_{s=S_1}^{S_2-1} V_s \text{ and} \quad [3.1]$$

$$\bar{V}^- = -\frac{1}{S_4 - S_3} \sum_{s=S_3}^{S_4-1} V_s, \quad [3.2]$$

where S_1 is the sample taken at time t_{S_1} , S_2 is the sample taken at time t_{S_2} , and so on.

The total voltage, \bar{V} , is calculated as arithmetic mean from \bar{V}^+ and \bar{V}^- :

$$\bar{V} = \frac{\bar{V}^+ + \bar{V}^-}{2}. \quad [3.3]$$

Accordingly, the coefficient of variation, CV_t , can be derived for each voltage trace:

$$CV_t = \frac{2}{\bar{V}^+ + \bar{V}^-} \sqrt{\frac{\sum_{s=S_1}^{S_2-1} (V_s - \bar{V}^+)^2 + \sum_{s=S_3}^{S_4-1} (V_s - \bar{V}^-)^2}{(S_2 - S_1) + (S_4 - S_3) - 1}}. \quad [3.4]$$

Both \bar{V} and CV_t are calculated internally by the RESECS measurement device which was used for this study.

3.2 Modeling

3.2.1 Physical Fundamentals

In order to survey the electric potential in dependence of the location, \mathbf{x} , the relation between electric potential, current, and electrical conductivity has to be known. According to Ohm's law the electric current density, \mathbf{j} , is given by

$$\mathbf{j} = \sigma_b \mathbf{E}, \quad [3.5]$$

where σ_b is the bulk soil electrical conductivity and \mathbf{E} the electric field. Due to the fact that the current is static for DC applications, \mathbf{E} can be written as the gradient of the scalar electric potential, φ , with

$$\mathbf{E} = -\nabla \varphi. \quad [3.6]$$

The law of charge conservation and the assumption of an idealized point source at location \mathbf{x}_c as current source with strength I , is given by

$$\nabla \cdot \mathbf{j} = -\frac{\partial Q}{\partial t} = I \delta(\mathbf{x} - \mathbf{x}_c), \quad [3.7]$$

where Q is the electrical charge density, t is time, and δ is the Dirac delta function. Combining Eqs. [3.5] to [3.7] yields the Poisson equation

$$\nabla \cdot (\sigma_b \nabla \varphi) = -I \delta(\mathbf{x} - \mathbf{x}_c). \quad [3.8]$$

Additionally, it is postulated that there is no current flow normal to the ground surface (negligible conductivity of air). In terms of the potential this is expressed by the Neumann boundary condition

$$\frac{\partial \varphi}{\partial n} = 0, \quad [3.9]$$

where n is the outward normal. At the other boundaries, generally a so-called mixed boundary condition,

$$\sigma_b \frac{\partial \varphi}{\partial n} + \lambda \varphi = 0, \quad [3.10]$$

is assumed, with some weighting parameter λ (see Kemna (2000)).

3.2.2 Modeling Concepts

The objective of resistivity tomography is to calculate the conductivity distribution with a relatively high resolution from a set of resistance measurements. This involves two steps: first, the so-called forward problem is solved, i.e., the Poisson equation [3.8] is solved for the given distribution (model) of σ_b , measurement geometry, and boundary conditions (Eqs. [3.9] and [3.10]). This results in a set of modeled resistances or apparent resistivities. In a second step, the modeled data are compared with the measured data and the model is adapted such as to minimize the residues between modeled and measured data. This task is called the inverse problem (Fig. 3.2). The procedure is repeated until the measured data are explained by the model to an acceptable degree.

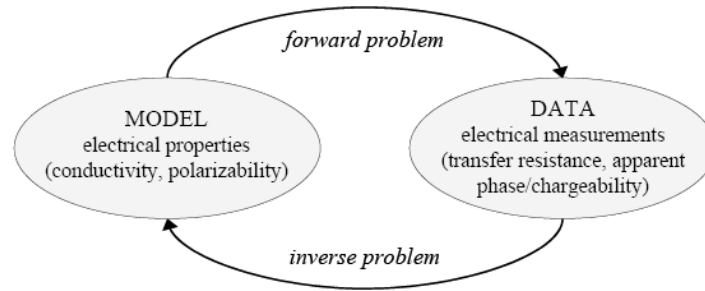


Fig. 3.2: Definition of the electrical forward and inverse problems after Binley and Kemna (2005).

3.2.3 The Forward Problem

The 3D problem given by Eq. [3.8] can be reduced to a 2D problem if it is assumed that the conductivity distribution is constant in one spatial direction (here taken as the y direction). Then the Fourier cosine transform (note that φ is even with respect to y)

$$\tilde{\varphi}(x, k, z) = \int_0^{\infty} \varphi(x, y, z) \cos(ky) dy \quad [3.11]$$

can be applied to Eq. [3.8], yielding

$$\frac{\partial}{\partial x} \left(\sigma_b \frac{\partial \tilde{\varphi}}{\partial x} \right) + \frac{\partial}{\partial z} \left(\sigma_b \frac{\partial \tilde{\varphi}}{\partial z} \right) - k^2 \sigma_b \tilde{\varphi} = -\frac{I}{2} \delta(x) \delta(z). \quad [3.12]$$

Here, k is the wavenumber corresponding to the strike direction y , and $\tilde{\varphi}(x, k, z)$ is the transformed potential, which is back-transformed into real space by means of an inverse Fourier cosine transform after Eq. [3.12] has been solved for a set of k values (Kemna, 2000).

In the current study, the code “CRMod” (Kemna, 2000) was used for the geoelectrical modeling, which solves the partial differential equation [3.12] numerically by means of the finite-element (FE) method. This means that the conductivity distribution is discretized into a finite number of elements. They all are assumed to have a constant conductivity. Based on Eq. [3.12] the electric potential is calculated for each node (that means for all vertices of each element).

For more details on the forward modeling procedure it is referred to Kemna (2000).

3.2.4 The Inverse Problem

For the solution of the inverse problem, a model vector, \mathbf{m} , is defined which contains the logarithm of the bulk soil electrical conductivity, $\sigma_{b,j}$, for each element

$$m_j = \ln \sigma_{b,j} \quad (j = 1, \dots, M), \quad [3.13]$$

where M is the number of elements. A data vector, \mathbf{d} , contains the measured, log transformed resistances, R_i , obtained from the measured voltages (Eq. [3.3]), i.e.,

$$d_i = \ln R_i \quad (i = 1, \dots, N), \quad [3.14]$$

where N represents the number of measurements. The logarithm in Eq. [3.13] and [3.14] is used due to the typically huge range of possible resistance and conductivity values. The main goal of the inversion process is to find an appropriate model \mathbf{m} which satisfies the data vector \mathbf{d} to a given degree of uncertainty. This is accomplished by minimizing the cost function (Tikhonov and Arsenin, 1977)

$$\Psi(\mathbf{m}) = \Psi_d(\mathbf{m}) + \alpha_r \Psi_m(\mathbf{m}), \quad [3.15]$$

where $\Psi_d(\mathbf{m})$ is the data misfit term, α_r is a regularization parameter responsible for the weighting of the roughness term, $\Psi_m(\mathbf{m})$. The latter is calculated by

$$\Psi_m(\mathbf{m}) = \|\mathbf{R}\mathbf{m}\|^2 \approx \iint \|\nabla_{2D} m(x, z)\|^2 dx dz, \quad [3.16]$$

where m represents the continuous model $m = \ln \sigma_b$, ∇_{2D} is the two-dimensional nabla operator, and \mathbf{R} is a roughness matrix which evaluates the first-order roughness of the discretized model \mathbf{m} . This kind of inversion, which punishes the deviation from a smooth model, is called ‘‘Occam’s inversion’’. In field applications it might make sense to account for the anisotropy of the earth model, e.g., horizontally stratified layers. This can be incorporated by separating \mathbf{R} into \mathbf{R}_x and \mathbf{R}_z , i.e. roughness matrices with respect to x and z directions, and correspondingly α_r into $\alpha_{r,x}$ and $\alpha_{r,z}$, respectively.

The first part of the objective function (Eq. [3.15]), i.e., the data misfit term, $\Psi_d(\mathbf{m})$, is defined by

$$\Psi_d(\mathbf{m}) = \|\mathbf{W}_d [\mathbf{d} - \mathbf{f}(\mathbf{m})]\|^2, \quad [3.17]$$

where \mathbf{f} represents the forward operator and \mathbf{W}_d is a data weighting matrix. Assuming that the data errors are uncorrelated, \mathbf{W}_d is a diagonal matrix containing in its i -th element the inverse of the standard deviation (error), ε_i , of the i -th datum, d_i , i.e., $\varepsilon_i = \sigma(\ln R_i)$.

Due to the non-linearity of $\mathbf{f}(\mathbf{m})$, the minimization of the objective function $\Psi(\mathbf{m})$ has to be performed in an iterative manner. In order to calculate the model update, Δm_q , the Gauss-Newton approach is applied, in which at each iteration, q , the linear system of equations

$$\mathbf{B}_q \Delta \mathbf{m}_q = \mathbf{b}_q, \quad [3.18]$$

with

$$\mathbf{B}_q = \mathbf{J}_q^T \mathbf{W}_d^T \mathbf{W}_d \mathbf{J}_q + \alpha_r \mathbf{R}^T \mathbf{R} \quad [3.19]$$

and

$$\mathbf{b}_q = \mathbf{J}_q^T \mathbf{W}_d^T \mathbf{W}_d [\mathbf{d} - \mathbf{f}(\mathbf{m}_q)] - \alpha_r \mathbf{R}^T \mathbf{R} \mathbf{m}_q, \quad [3.20]$$

is solved. Here, \mathbf{J}_q is the Jacobian matrix with entities $J_{ij} = \partial f_i / \partial m_j$, calculated for the current model \mathbf{m}_q . The model update is finally added to the previous model:

$$\mathbf{m}_{q+1} = \mathbf{m}_q + \Delta \mathbf{m}_q. \quad [3.21]$$

As starting model, \mathbf{m}_0 , usually a homogeneous half-space is adopted, i.e., the geometric mean of all measured apparent resistivities, ρ_a .

Finally, the iteration process is stopped when the data misfit $\Psi_d(\mathbf{m}_q)$ matches the misfit target value. This is evaluated using the “root mean square” (RMS) error given by

$$\varepsilon_q^{RMS}(\mathbf{m}_q) = \sqrt{\frac{\Psi_d(\mathbf{m}_q)}{N}} = \sqrt{\frac{1}{N} \sum_{i=1}^N \frac{|d_i - f_i(\mathbf{m}_q)|^2}{\varepsilon_i^2}}. \quad [3.22]$$

A final target value of $\varepsilon^{RMS}(\mathbf{m}) = 1$ is desired in order to assure that, on average, the individual data misfit, $|d_i - f_i(\mathbf{m})|$, is in the same range as the individual data error, ε_i .

In order to solve the inverse problem the code “CRTomo” was used. For more details on the inverse modeling procedure it is referred to Kemna (2000).

3.2.5 Error Model

The data error, ε_i , can be estimated by means of normal and reciprocal measurements (Daily et al., 2004). This means that a measurement with a certain four-pole electrode configuration is repeated with interchanged current and voltage dipoles. Theoretically, the resulting resistances should be identical. Therefore, the difference between these (log transformed) resistances can be interpreted as a measure of the data error:

$$e_i = \Delta \ln R_i = \ln R_{i,nor} - \ln R_{i,rec} \quad (i = 1, \dots, N), \quad [3.23]$$

where $R_{i,nor}$ and $R_{i,rec}$ denote the resistance of the normal and the reciprocal measurement, respectively. To account for these errors during the inversion, an appropriate error model has to be incorporated to weight each data misfit, $d_i - f_i(\mathbf{m})$, according to the error level of the measurement.

One commonly adopted method is the use of the dependency of ε_i on the resistance. Similar to LaBrecque et al (1996), ε_i is obtained by

$$\varepsilon_i = a_e + \frac{b_e}{R_i} \quad (i = 1, \dots, N). \quad [3.24]$$

Here, \bar{R}_i is the mean calculated from $R_{i,nor}$ and $R_{i,rec}$, and a_e and b_e are fitting parameters where a_e corresponds with a relative resistance error and b_e with an absolute resistance error, the latter accounting for a minimal resistance error level which is always present (e.g., by the limited accuracy of the measurement apparatus).

3.2.6 Robust Inversion

The individual data errors are often not known exactly, and particularly may be strongly underestimated for data outliers. This may virtually result in an attempt to fit data errors and, in turn, may produce artefacts in the inverted model. LaBrecque and Ward (1991) proposed an approach, that they referred to as robust inversion, in which errors of data with relatively large individual misfits are successively increased during the inversion process. In this approach, the individual data misfit is calculated at each iteration q :

$$\chi_{i,q} = \frac{d_i - f_i(\mathbf{m}_q)}{\varepsilon_{i,q}} \quad (i = 1, \dots, N). \quad [3.25]$$

Depending on this current data misfit, the data error is increased in a first intermediate step:

$$\varepsilon_i' = \varepsilon_{i,q} \sqrt{|\chi_{i,q}|} \quad (i = 1, \dots, N). \quad [3.26]$$

In a second step, this new data error is normalized by relating the L₁-norm of the data misfit vector containing the data errors resulting from Eq. [3.26] to the L₁-norm of the data misfit based on the original data errors at the given iteration (Eq.[3.25]):

$$\varepsilon_i'' = \varepsilon_i' \frac{\|\chi_i'\|_1}{\|\chi_q'\|_1} \quad (i = 1, \dots, N), \text{ where } \chi_i' = \frac{d_i - f_i(\mathbf{m}_q)}{\varepsilon_i'} \quad (i = 1, \dots, N) \quad [3.27]$$

Finally, the data error from Eq. [3.27] is assigned to the data error for the new iteration if it is larger than the current error:

$$\varepsilon_{i,q+1} = \begin{cases} \varepsilon_{i,q} & , \varepsilon_i'' \leq \varepsilon_{i,q} \\ \varepsilon_i'' & , \varepsilon_i'' > \varepsilon_{i,q} \end{cases} \quad (i = 1, \dots, N). \quad [3.28]$$

Since the resulting data errors are generally larger than the original input errors, the robust approach may lead to a loss of resolution if the firstly specified errors had been estimated correctly. The method of robust inversion is applied in Chapter 4.

3.2.7 Accumulated Sensitivity

One easy method to assess the quality of the inversion results makes use of the accumulated sensitivity, which gives insight into the resolution for the given electrode arrangement, measurement protocol, and conductivity distribution. It is calculated by summing the absolute or squared sensitivities of all measurements for each model parameter. If an individual error scheme is used in the inversion, it is appropriate to also involve the corresponding data errors (Kemna, 2000):

$$s_j = \sum_{i=1}^N \frac{a_{ij}^2}{\varepsilon_i^2} \quad (j = 1, \dots, M), \text{ with } a_{ij} = \frac{\partial f_i}{\partial m_j}. \quad [3.29]$$

3.2.8 Temperature Correction

Whenever a comparison of absolute σ_b values was performed in this work, both TDR and ERT based σ_b values were standardized at a temperature of 25 °C, in order to obtain measurements independent of temporal temperature variations, by means of the correction factor proposed by Franson (1985):

$$\sigma_b(25^\circ\text{C}) = f_T \sigma_b(T_s), \text{ with } f_T = \frac{1}{[1 + \alpha_T(T_s - 25^\circ\text{C})]}, \quad [3.30]$$

where α_r is a temperature coefficient, which is equal to $0.0191(^{\circ}\text{C})^{-1}$ for a standard 0.01 mol l^{-1} KCl solution, and T_s is the temperature of the soil in $^{\circ}\text{C}$.

4 Characterization of Data Noise and its Implementation in Electrical Resistivity Tomography for Imaging Bulk Electrical Conductivity in the Vadose Zone

4.1 Abstract

An approach is presented to investigate the impact of data errors on the bulk electrical conductivity in the vadose zone derived by cross-hole electrical resistivity tomography (ERT). To place emphasis on hydrological aspects, a synthetic experiment should clarify whether there is a cognizable difference between inverted ERT data sets produced under different soil moisture conditions: On the basis of actual measurements of bulk soil electrical conductivity taken from time domain reflectometry (TDR), an earth model was once constructed from a saturated soil profile, and once from a rather dry profile. After simulating the corresponding resistances of a dipole-dipole survey between two boreholes, these were noised by means of authentic error distributions derived from field data in the framework of a Monte Carlo approach. Different error models were used within the consecutive inversion process. It could be seen that the variability of the resulting resistivities could be reduced when an error model was employed which was derived specifically for each electrode configuration. It became obvious that such data errors propagated ruthlessly into the final model, leading occasionally to an overlap of resulting resistivity distributions when data sets were taken under dry and wet soil conditions, respectively. The results of this study suggest to evaluate data errors precisely. If possible, data errors should be detected in dependence of the corresponding measurement geometry.

4.2 Introduction

Electrical resistivity tomography (ERT) has become a more frequently used method in soil science and hydrogeology to obtain information about the subsurface such as water content, porosity, and ion concentration of the soil solution. ERT was employed in water infiltration experiments (Daily et al., 1992; Park, 1998), tracer observation studies (al Hagrey and Michaelson, 1999; Slater et al., 2000; Binley et al., 2002a; Kemna et al., 2002), and moisture content monitoring (Zhou et al., 2001; Binley et al., 2002b; Zhou et al., 2002; Michot et al., 2003). Several authors reported that they observed considerable data errors in resistances exceeding 10 % (Slater et al., 2000; Binley et al., 2002a). Therefore, they removed these measurements prior to the inversion. There are three different sources influencing the measured data error (Binley et al., 1995): Systematic errors caused by poor electrode contact of certain electrodes, random errors resulting from the measurement device, and sporadic errors appearing due to external effects. To account for these errors during the inversion, most codes use an error model in which the error increases linearly with the magnitude of the measured resistance (LaBrecque et al., 1996). Binley et al. (1995) inverted noised synthetic data once individually with well known data errors, and once without any prior knowledge, weighting all measurements equally. The latter inversion resulted in a much poorer image reconstruction. LaBrecque et al. (1996) also pointed out the importance to estimate data errors as correctly as possible. In synthetic experiments they found out that underestimated standard deviations lead to rough images including artifacts, whereas overestimated standard deviations dramatically reduce the image resolution. Zhou and Dahlin (2003) derived from measurements at several test sites that the relative error increases as a power with the decrease of the potential reading. Once data errors are estimated, the propagation of the data errors or uncertainty into the estimated parameters can be evaluated. Alumbaugh and Newman (2000) referred to this approach as posterior image appraisal. Park and Van (1991) concluded from synthetic studies that larger weights in the sensitivity matrix roughly corresponded to areas where the geometry of a buried conductor was matched well. Alumbaugh and Newman (2000) employed for image appraisal after electromagnetic inversion the model resolution matrix, which filters the true model spatially to yield an imaged model. Furthermore, they evaluate the model covariance matrix, the main diagonal of which shows how the data error is mapped into uncertainty in the parameter estimates. Day-Lewis et al. (2005) dealt

in their study with correlation loss, that is the phenomenon that the spatial structure of tomograms may only weakly reflect the true spatial structure of the surface. By means of synthetic cross-hole experiments they compare the resolution of images derived from GPR with that derived from ERT for different case studies. In general, they come to the conclusion that GPR performs better in the area between the boreholes, whereas ERT provides a better resolution close to the boreholes.

In this study, we mainly concentrate on the a priori analysis of data errors, but also on their impact on the resulting resistivity distribution. Therefore, two different earth models are constructed from TDR data. One is taken from a saturated soil profile, one during rather dry soil conditions. The corresponding modeled resistance measurements are noised by means of a representative error distribution. Finally, the uncertainty in resistivity is analyzed computing Monte Carlo simulations. The first aim of this study is to evaluate data errors occurring in ERT field measurements as properly as possible. The second is to investigate whether the difference between extreme soil moisture conditions can be determined by ERT even in presence of considerable data errors.

4.3 Materials and Methods

4.3.1 Forward Simulation

In order to cover a broad range of soil water contents, two points in time were selected from the TDR time series: once when the soil was nearly saturated (06/05/2006) and once when very dry conditions (07/27/2006) predominated (Fig. 4.1). According to Eq. [3.30], the selected TDR σ_b profiles were corrected for temperature variations with depth, which were measured using temperature probes.

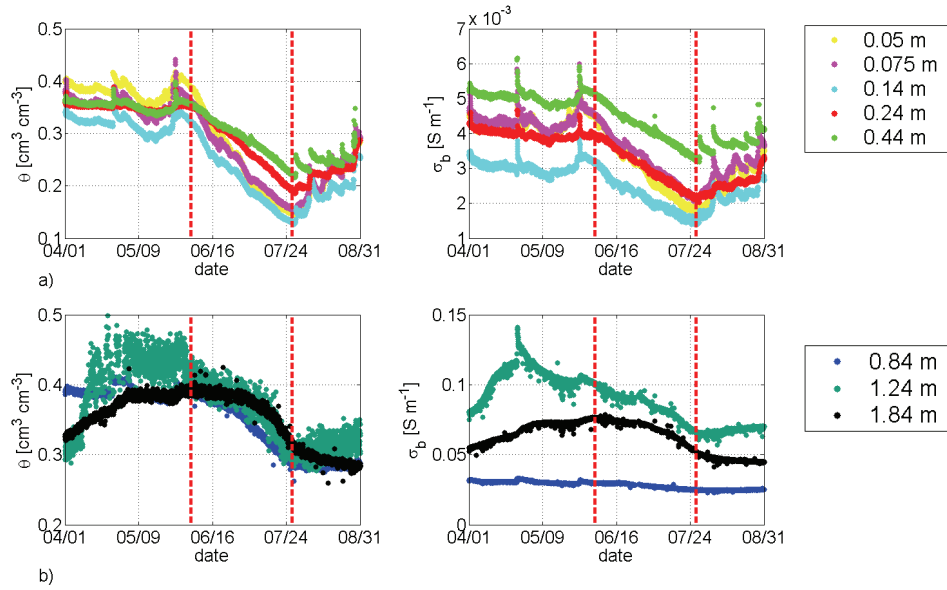


Fig. 4.1: Volumetric soil water content, θ , (left) and bulk soil electrical conductivity, σ_b , (right) measured by TDR. Dashed red lines represent dates when profiles were taken to generate an earth model for the synthetic ERT study.

a) Measurements of upper five TDR probes.

b) Measurements of lower three TDR probes.

From the vertical σ_b profiles measured by TDR, a 2D distribution of σ_b values was constructed assuming no lateral variations (Fig. 4.2). This resulted in a layered earth

model which corresponds to the soil profile at the test site, that is classified as Stagnic Luvisol. Vertically, σ_b varies by one order of magnitude, whereas it changes seasonally only by a factor of 1.5 to 2.

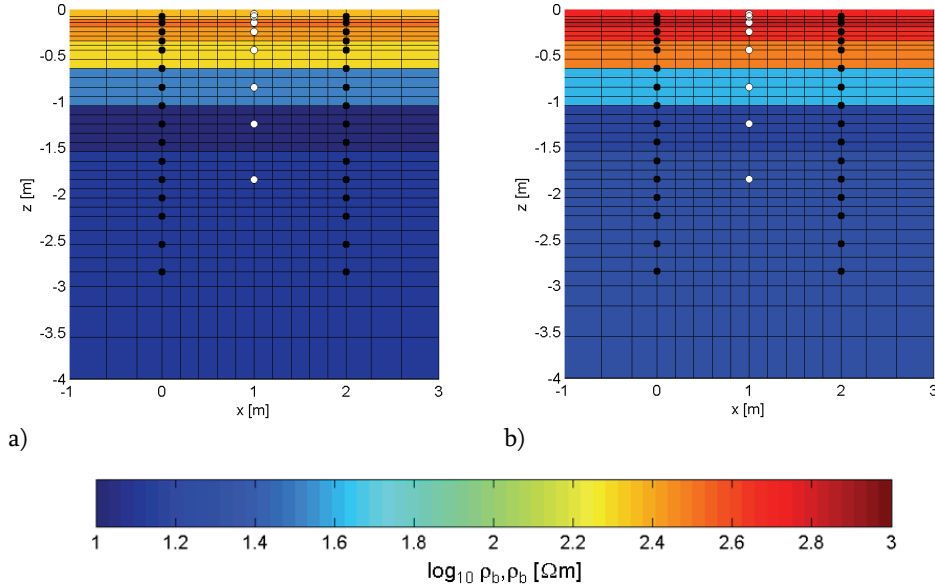


Fig. 4.2: Resulting earth models derived from TDR measurements. TDR positions are indicated by white dots, ERT electrodes by black dots.

a) Wet conditions (06/05/2006). b) Dry conditions (07/27/2006).

ERT resistances related to this earth model were calculated for 220 dipole-dipole configurations (in-hole and cross-hole), identical to the arrays used for the field measurements. This forward simulation was performed by means of the “CRMod” code (Kemna, 2000) for the wet and for the dry case, respectively.

4.3.2 Generating Noisy Data

When analyzing the data errors, the question arose whether the resistance dependent error model (Eq. [3.24]) is capable of describing the measurement errors occurring in the field. Therefore, one data set collected at August 30, 2006 was considered in more detail. The normal-reciprocal error was taken for a certain dipole-dipole configuration across the first two boreholes of the field site. Consequently, the error was determined for the same configuration occurring across the second and third borehole, across the third and fourth borehole, and so forth (Fig. 4.3). Thus, each electrode configuration led to a distribution of normal-reciprocal errors.

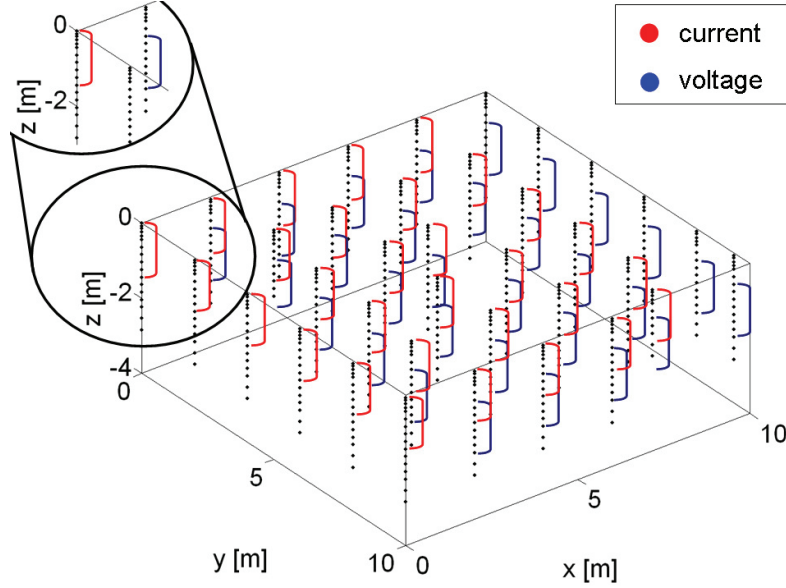


Fig. 4.3: Selection of a certain electrode configuration across the first two boreholes (see cut-out in the upper left corner) and recovery within the remaining boreholes.

Since the electrical properties are assumed to vary insignificantly in horizontal direction, each configuration was related to a mean resistance. This was given by the average of all resistances belonging to the same electrode configuration.

Following the idea of the resistance dependent error model (Eq. [3.24]), configurations with similar resistances should exhibit similar distributions of normal-reciprocal errors. Fig. 4.4 shows distributions of differences between normal and reciprocal measurements for two cross-hole configurations with similar mean resistances, but different electrode configurations. Fig. 4.4a corresponds to an electrode configuration with a current dipole at the surface and a voltage dipole at the bottom of the next borehole, resulting in a resistance of 0.111Ω . The histogram of Fig. 4.4b was derived from measurements when both dipoles were located at the bottom of the respective boreholes, resulting in a resistance of 0.106Ω . It is obvious that both distributions differ considerably from each other. Despite of that, the resistance dependent error model would suggest the same error level for both configurations.

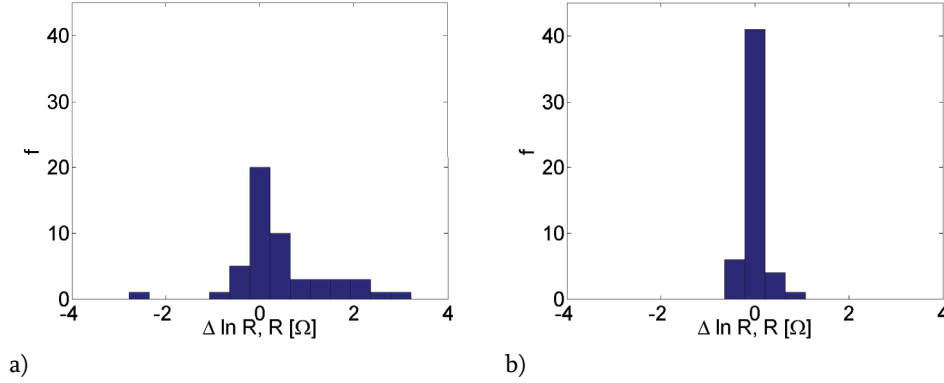


Fig. 4.4: Distribution of normal-reciprocal errors for measurements with similar resistance but different geometry.

a) Current dipole top, voltage dipole bottom.

b) Current dipole bottom, voltage dipole bottom.

In consideration of all different electrode configurations occurring within one data set, Fig. 4.5 depicts a plot of the measured error level from each electrode configuration against its particular mean resistance. In addition, the errors calculated by the resistance dependent error model Eq. [3.24] are shown (red line). This model was calibrated by thirty data sets, leading to a parameterization of $a_e = 0.126$ and $b_e = 2.76e-004 \Omega$. It is evident that, for a given resistance, the measured error levels of different electrode configurations show a rather high variation, whereas the model suggests a constant value.

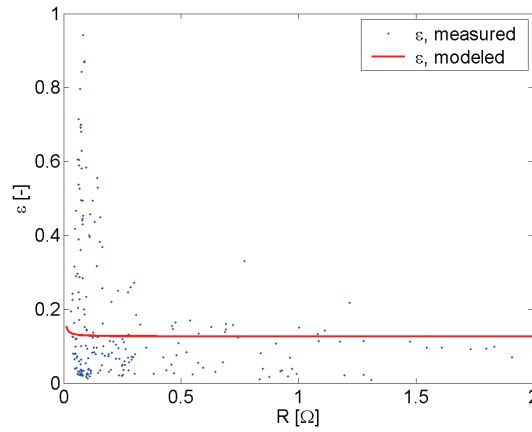


Fig. 4.5: Error level dependent on resistance, each point represents one electrode configuration. Red line illustrates the error calculated by the resistance dependent error model Eq. [3.24].

Therefore, we considered an individual error model for each electrode configuration, which is the equivalent of formulating the error dependent on the geometric factor. Due to the fact that the geometric factor is inversely related to the resistance, this error model is similar to the resistance error model given in Eq. [3.24] if a constant resistivity distribution is assumed. However, our study is based on a highly layered earth model.

The error for a certain electrode configuration was derived from normal-reciprocal measurements for thirty data sets recorded from June 2 to November 10 of the year 2006. By defining the error model in this way, we aim at the overall uncertainty of the inverted resistivity distribution between any pair of boreholes but not for the uncertainty of a distribution between a specific pair of boreholes.

The observed normal-reciprocal errors do not follow a Gaussian distribution but show very long tailings caused by some outliers (Fig. 4.6). Taking the standard deviation from that, a Gaussian model as assumed in this study would not be able to recover the high peak of this distribution (red line, Fig. 4.6).

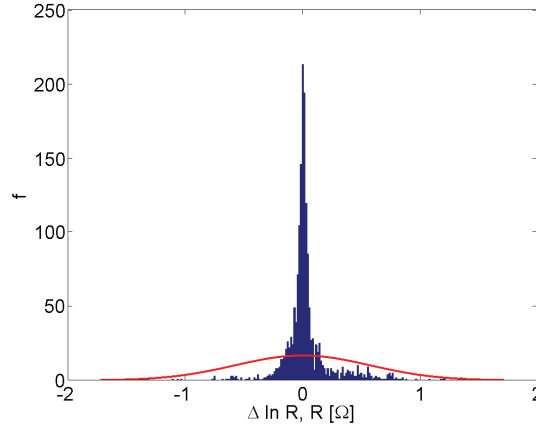


Fig. 4.6: Exemplary histogram of normal-reciprocal errors taken from a certain electrode configuration of 30 data sets, the resulting sample consists of 1690 error values.

The red line represents a fit of a Gaussian model to this distribution.

Therefore, the frequency of low-biased measurements would be highly underestimated. To derive a Gaussian model which describes the largest part of the error distribution correctly, a robust estimator of the standard deviation, $\sigma(\Delta \ln R_i)$ (Eq. [4.1]), was calculated. This is based on the interquartile range, IQR , of the sample and of the standard normal distribution, respectively. The interquartile range is derived from the upper quartile (i.e., 75th percentile) and lower quartile (i.e., 25th percentile) of the distribution. The indices s and n denote the distribution of the sampled errors, $\Delta \ln R_i$, and the standard normal distribution, respectively.

$$\sigma(\Delta \ln R_i) = \frac{IQR_s}{IQR_n} = \frac{Q_{75,s} - Q_{25,s}}{Q_{75,n} - Q_{25,n}} \quad (i = 1, \dots, N). \quad [4.1]$$

Assuming that the errors of the normal and reciprocal measurements are uncorrelated, the variance of the errors, $\sigma^2(\Delta \ln R_i)$, can be derived by

$$\sigma^2(\ln R_{i,nor} - \ln R_{i,rec}) = \sigma^2(\ln R_{i,nor}) + \sigma^2(-\ln R_{i,nor}) \quad (i = 1, \dots, N). \quad [4.2]$$

Furthermore, the variances are assumed to be statistically identical for a normal as well as a reciprocal measurement of one configuration. The standard deviation of the logarithmic resistance is calculated by

$$\sigma(\ln R_i) = \sigma(\Delta \ln R_i) / \sqrt{2} \quad (i = 1, \dots, N). \quad [4.3]$$

But, in the ERT inversion program that we used, the mean of the normal and reciprocal resistances,

$$\ln \bar{R}_i = (\ln R_{i,nor} + \ln R_{i,rec}) / 2 \quad (i = 1, \dots, N), \quad [4.4]$$

was used and its standard deviation was calculated from

$$\sigma(\ln \bar{R}_i) = \sigma(\Delta \ln R_i) / 2 \quad (i = 1, \dots, N). \quad [4.5]$$

The noised logarithmic resistances, $\ln \bar{R}_i'$, were finally generated by the model

$$\ln \bar{R}_i' = \ln \bar{R}_i + e_{s,i} / 2 \quad (i = 1, \dots, N), \quad [4.6]$$

where $e_{s,i}$ is randomly drawn from the i -th distribution of normal-reciprocal errors, $\Delta \ln R_i$ (e.g., Fig. 4.6). The data sets recorded from June 2 to November 10 of 2006 served here as input data as well. Actually, this distribution of the differences between normal and reciprocal measurements cannot be scaled directly to the distribution of the average of the normal and reciprocal measurements when the error distribution is not Gaussian. However, to investigate the impact of a non-Gaussian distribution on the inversion results, the normal-reciprocal errors were taken as input data for the noise generation.

Following this approach, 500 synthetic data sets were generated, each consisting of 220 measurements.

4.3.3 Error Model Dependent on Resistance

According to Eq. [3.17], an appropriate error model is required which weights the data misfit of a certain measurement to a corresponding error level used within the inversion. One commonly adopted method is to estimate the error level from the resistance using Eq. [3.24]. This model was calibrated on the basis of the above mentioned thirty data sets. First, the normal-reciprocal errors of all measurements were grouped into 100 resistance bins. Secondly, the robust estimate of the standard deviation was calculated for each bin. Finally, the error model according to Eq. [3.24] was fitted to these standard deviations in consideration of Eq. [4.5]. This approach led to a parameterization of Eq. [3.24] with $a_e = 0.126$ and $b_e = 2.76e-004 \Omega$, meaning a relative error of about 13 % regarding the mean. This error exceeds the values observed in other studies where all measurements with a normal-reciprocal error greater than 10 % could be removed (Slater et al., 2000; Binley et al., 2002a). Singha and Gorelick (2005) even found maximal discrepancies between normal and reciprocal measurements of only 5 %.

For the inversion of the synthetically generated data sets, the expected standard deviation of the measurement error was calculated using the error model Eq. [3.24]. This estimate of the measurement error standard deviation was used to filter outliers of the error distribution. Data for which the difference between normal and reciprocal measurements was larger than twice its expected standard deviation were excluded from the data set. This led to data sets with different contributing electrode configurations. The mean number of measurements used for the inversion amounted 179 out of 220 possible measurements between two boreholes.

4.3.4 Error Model Dependent on Electrode Configuration

a) Without Filter Scheme

Here, for each electrode configuration occurring within one borehole and between two adjacent boreholes, respectively, the error distribution which was the basis for the noise generation was employed: The robust estimated standard deviation of this distribution was taken and transformed to the desired standard deviation of the logarithmic mean resistance (Eq. [4.5]). These specific errors result in the data weighting matrix deployed for the individual error weighting during the inversion (Eq. [3.17]),

b) With Filter Scheme

In this approach, outliers of the measurement error distribution were excluded from the inversion. Data with a measurement error that was larger than twice the robust estimate of the configuration-specific standard deviation were excluded from the inversion. After preprocessing, there remained on average 171 out of 220 measurements.

4.3.5 Inversion

Finally, the generated data sets were inverted. Therefore, the different inversion schemes used in this study can be summarized as follows: taking a) an error model dependent on resistances with previous filtering (hereafter referred to as fREM), b) an error model dependent on the electrode configuration (hereafter referred to as CEM), and c) the same model as b), but with previous data filtering (hereafter referred to as fCEM). Additionally, all cases were conducted once by means of a non-robust inversion scheme (errors are kept constant during all iterations) and once by means of a robust inversion scheme (Eq. [3.25] to [3.28]).

The inversion of all data was performed by means of the 2.5D finite element code “CRTomo” (Kemna, 2000).

4.4 Results and Discussion

4.4.1 Reproduction of the Earth Model

To assess the reproduction of the earth model derived from TDR data, the mean of the 500 resistivity distributions was calculated pixel-wise for each kind of inversion. In Fig. 4.7 the results are shown for all scenarios of the non-robust inversion scheme, exemplary illustrated for wet soil conditions. In general, the boundary between the resistive top and the far less resistive bottom part is recovered well.

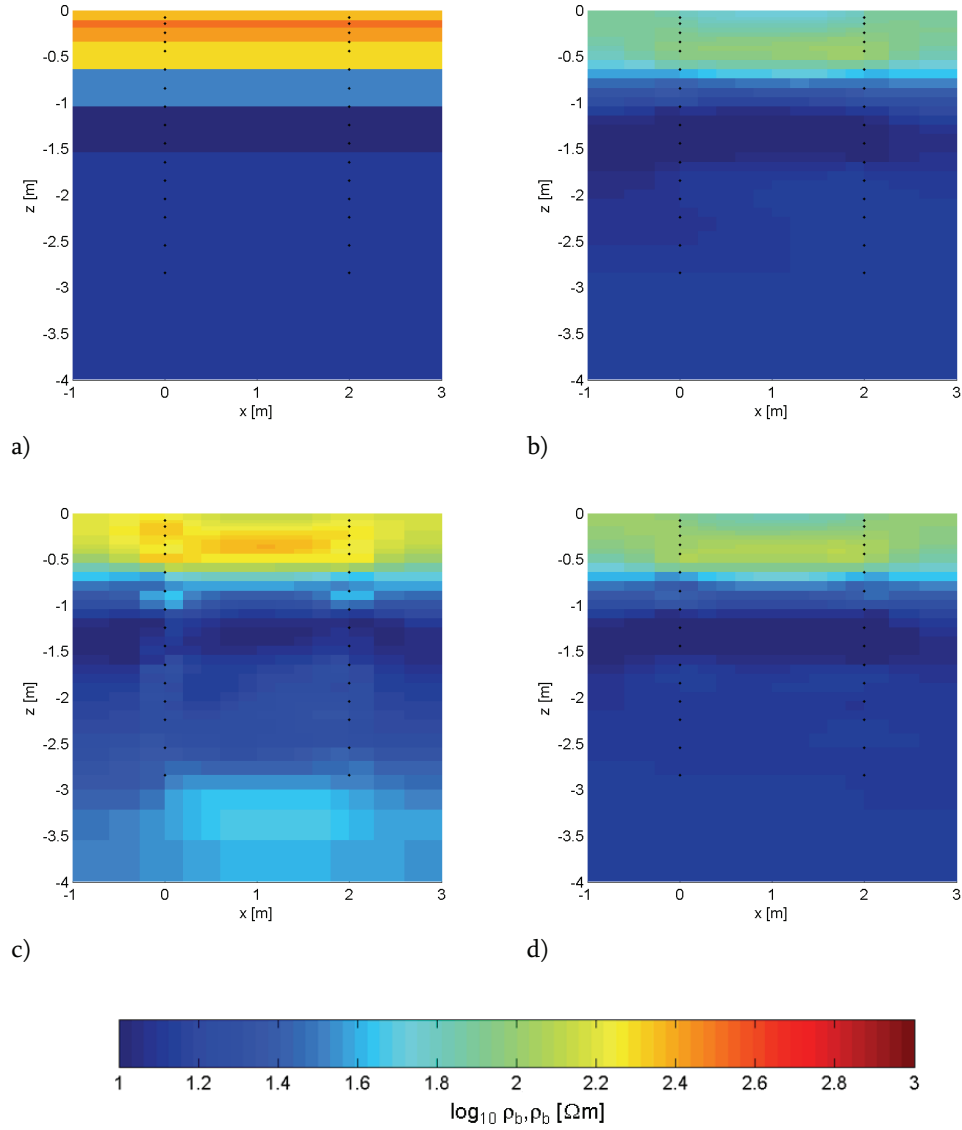


Fig. 4.7: Original earth model constructed during wet conditions compared with mean resistivity distributions calculated by non-robust inversion, electrode positions are depicted by black dots.

a) Earth model derived by TDR. b) Mean resistivity produced by fREM.

c) Mean resistivity produced by CEM. d) Mean resistivity produced by fCEM.

But the magnitude of resistivities, particularly within the uppermost part of the soil, is underestimated independent on the chosen error model. The original distribution with its sharply separated layers given by the earth model (Fig. 4.7a) cannot be reproduced correctly. This is evoked by the regularization of the Occam's inversion which causes a certain smearing between the high resistive layer at the surface and the low resistive layer in a depth below 1 m. This issue is also pointed out by Day-Lewis et al. (2005) who investigated for this reason the limitations of geophysical data. Assuming high data errors in a profile containing high resistive layers, LaBrecque et al. (1996) also observed images which were somewhat smoothed compared with the true model. They related this problem to the fact that for the simulation a grid is taken consisting of elements as small as possible to accurately approximate the geoelectrical boundaries. This leads to a highly underdetermined inversion since the number of elements is much larger than the number of measurements. However, the model derived by CEM (Fig. 4.7c) seems to recover the "truth" at the best, followed by the fCEM (Fig. 4.7d) based results. Both fREM (Fig. 4.7b) and fCEM (Fig. 4.7d) based resistivity distributions show artifacts between the boreholes at the near surface. Furthermore, the mean resistivity produced by inversions with CEM (Fig. 4.7c) contains an area with conspicuously underestimated values at the bottom of the considered grid. However, taking into account the variability of the inverted data sets (Fig. 4.9), it is obvious that all these artifacts are closely related to areas of high uncertainty (further analysis is performed in the following sub-section).

Since measurement errors are often unknown or underestimated, it is sometimes advisable to employ a robust inversion scheme (Eq. [3.25] to [3.28]). Fig. 4.8 depicts these results for each scenario and again for the saturated soil profile. Independent on the chosen error model, these calculations lead to even lower resistivities close to the surface. Therefore, in case of layered media, the robust inversion scheme causes problems and the large differences of resistivities within the profile lead to large data misfits (Eq. [3.25]) nearby the surface.

This is particularly the case when a homogeneous starting model (in this study, the mean of all measured apparent resistivities was chosen) is used, which value is dominated by the two lowest thirds of the profile that exhibit a rather low resistivity. Finally, the iterative rise of the error level leads to a loss of resolution and a reduction of the resistivity in the near surface area.

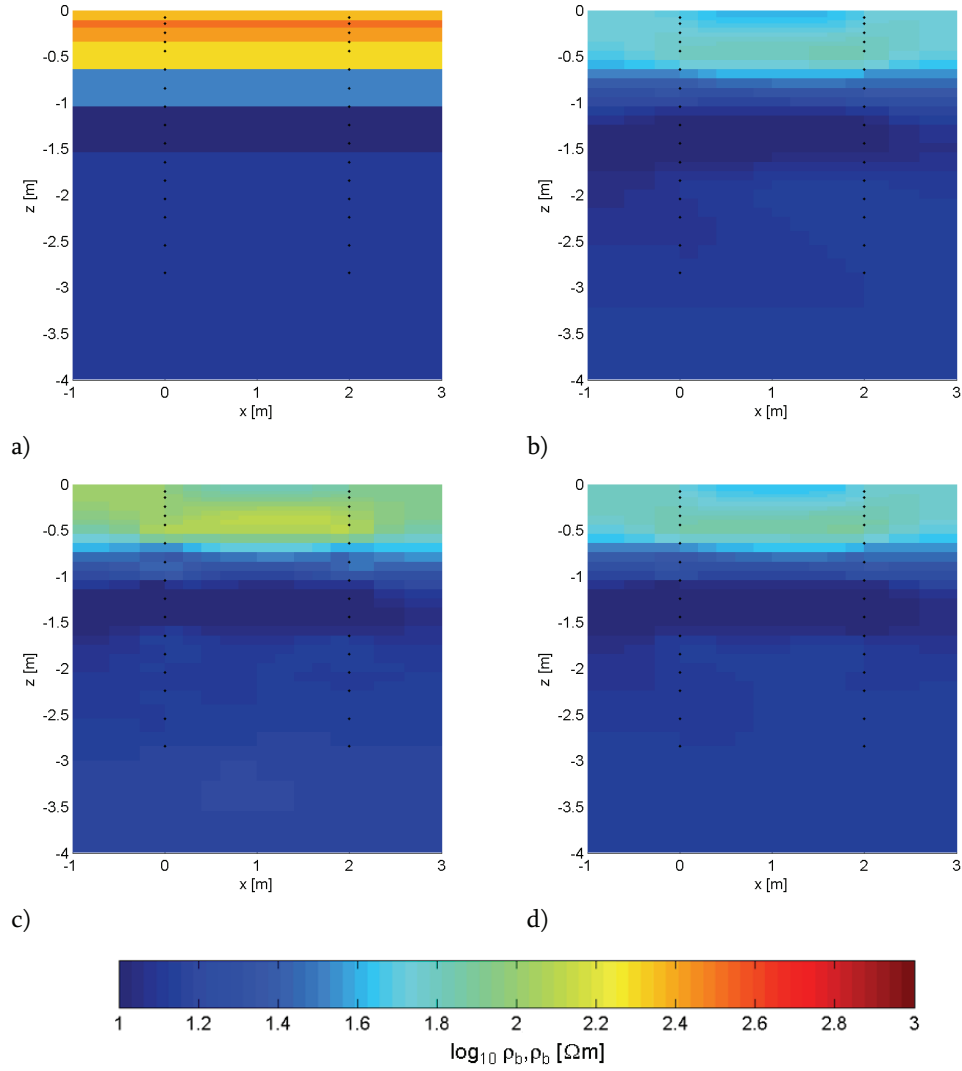


Fig. 4.8: Original earth model constructed during wet conditions compared with mean resistivity distributions calculated by robust inversion, electrode positions are depicted by black dots.

a) Earth model derived by TDR. b) Mean resistivity produced by fREM.

c) Mean resistivity produced by CEM. d) Mean resistivity produced by fCEM.

4.4.2 Uncertainty in Resistivity

To get an idea concerning the uncertainty in resistivity, the coefficient of variation (CV) was calculated pixel-wise. Since it was identified to be most feasible, we focus on the non-robust inversion scheme in the following. When the linear error model with a data filter (fREM) is used, highest variabilities can be found midway the boreholes at the surface and in a depth of about 1 m (Fig. 4.9a). In case of CEM, huge variabilities are observed (Fig. 4.9b, be aware of the different plot scale), reaching maximum values at the bottom of the grid. However, when the filtered data sets for the inversion (fCEM) are used, the variability can effectively be reduced (Fig. 4.9c). The resulting variabilities are even lower than in case of fREM which shows again a better reproduction of the data errors when employing the fCEM model.

In general, it is obvious that particularly regions at the surface located between the boreholes as well as elements in the immediate vicinity of the boreholes represent highest CV's. When these results are compared with the plot of the accumulated sensitivity (Eq. [3.29]), these highly variable regions are evidently related to areas of high sensitivity (Fig. 4.9d). At first notice, this might seem to be contradictory. But, when performing the inversions, regions with higher sensitivity are dominated by the data misfit term (Eq. [3.15]). Therefore, the inversion results in the highly sensitive regions are more sensitive to the measurements and consequently more influenced by the measurement errors. This causes higher variabilities calculated from a series of resistivity distributions. The opposite is the case for the low sensitivity regions: Here, the regularization term is dominating which introduces a smoothing of the model. Hence, the elements of these areas show more similar resistivities within the different realizations, resulting in lower variabilities. Taking into account the reproduction of the true model as well as the uncertainty, it can be concluded that the inversions based on fCEM lead to a model with lowest variability and still recover the truth to an acceptable degree.

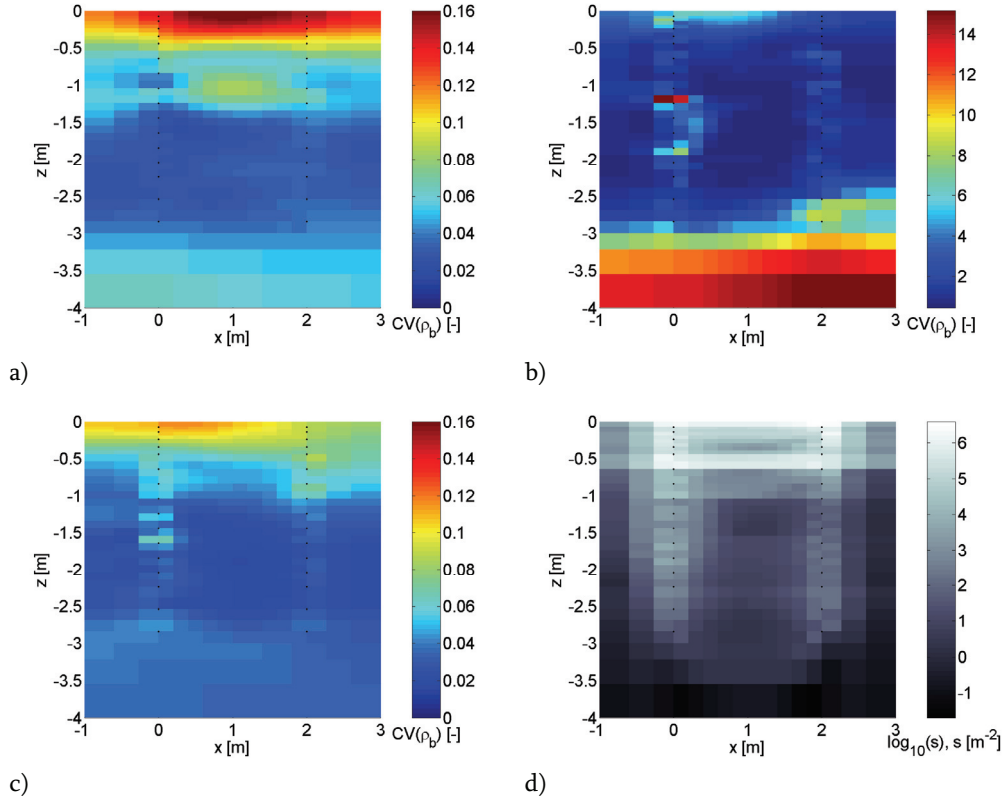


Fig. 4.9: Distributions of coefficient of variation (CV) compared with accumulated sensitivity. CV's are depicted again for wet conditions and the non-robust inversion scheme.

a) CV derived from fREM-based inversions. b) CV derived from CEM-based inversions (be aware of the different plot scale).

c) CV derived from fCEM-based inversions. d) Accumulated sensitivity (in consideration of CEM in Eq. [3.29]).

Finally, an interesting outcome is the fact that most of the distributions of logarithmic resistivities considered for one element show approximately a Gaussian behaviour (Fig. 4.10). However, the error distributions which were used to produce the synthetic data were non-Gaussian (e.g., Fig. 4.6). This indicates a kind of smoothing introduced by the inversion process.

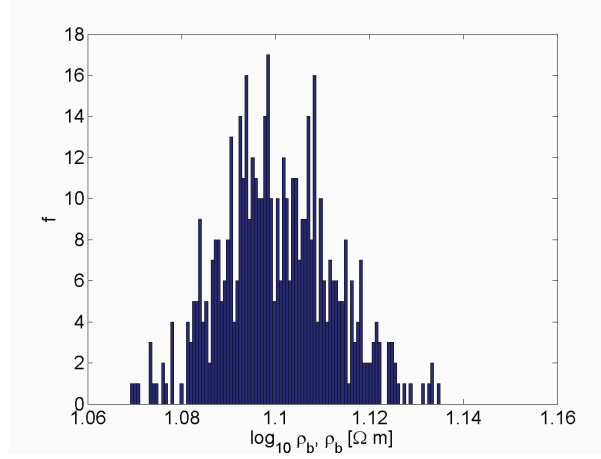


Fig. 4.10: Histogram plotted for an exemplary set of model parameters calculated by means of fCEM.

4.4.3 Comparison Between wet and dry Conditions

To receive an optical impression of the difference between dry and wet conditions resulting from the synthetic experiment, the mean resistivity distributions are depicted again together with the “true” model derived from the TDR measurements (Fig. 4.11).

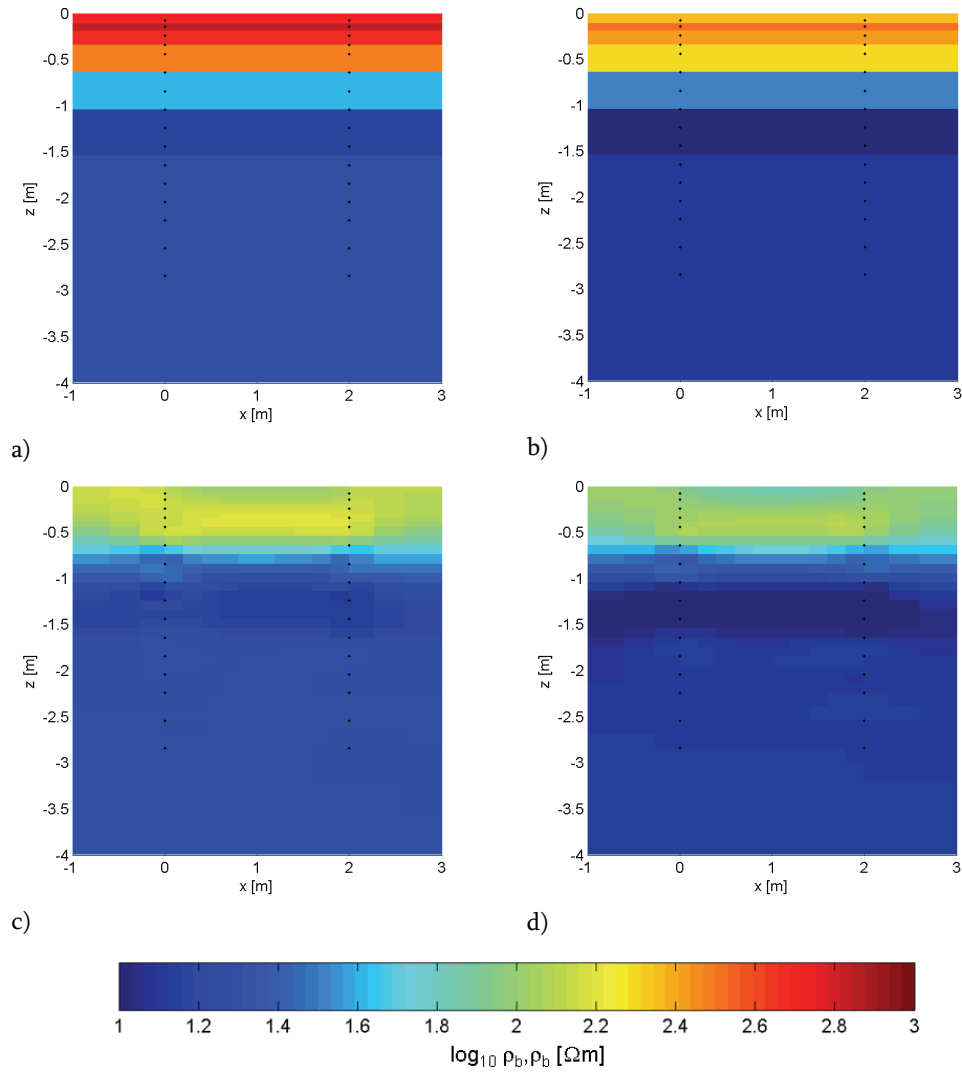


Fig. 4.11: Comparison of mean resistivity distributions between dry and wet conditions.
a) Dry conditions, original earth model b) Wet conditions, original earth model.
c) Dry conditions, mean resistivity based on fCEM, non-robust inversions.
d) Wet conditions, mean resistivity based on fCEM, non-robust inversions.

According to the previous results, we consider here only the most feasible case, namely the non-robust scheme calculated by means of fCEM. It can already be seen that visible differences between the distributions calculated from the inversions seem to be small.

To quantify the differences more precisely, Fig. 4.12 shows the factor of change,

$$\zeta = 10^{\log_{10}(\bar{\rho}_b^d) - \log_{10}(\bar{\rho}_b^w)} = \frac{\bar{\rho}_b^d}{\bar{\rho}_b^w},$$

which relates the mean resistivity of the dry condition, $\bar{\rho}_b^d$, to the mean resistivity of the wet condition, $\bar{\rho}_b^w$. Comparing the changes derived from the original earth models (Fig. 4.12a) with that derived from the fCEM inversions (Fig. 4.12b), it is evident that the values are highly underestimated within the uppermost layer. This is mainly caused by the underestimation of the “true” resistivities when considering dry conditions (Fig. 4.11a and c). Anyway, the ratio ζ calculated from the fCEM inversions reaches its maximum value of about 1.5 to 1.7 in two regions: On the one hand, within the uppermost half meter, on the other hand, in a depth of 1.2 to 1.5 m. In the vicinity of the left borehole, the factors of change even agree with that derived from the original earth models.

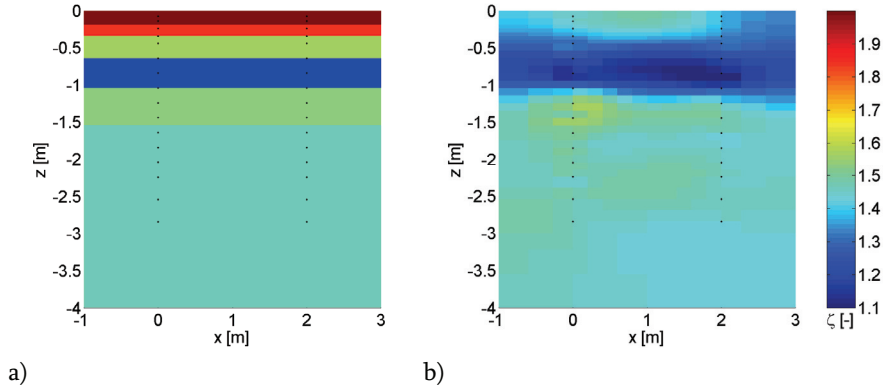


Fig. 4.12: Distribution of the relation between the mean resistivities of the dry and wet conditions, ζ .

a) Calculated from original earth models.

b) Calculated from non-robust inversions and fCEM.

For further investigation it is important to take also the variance into account. Thus, eventual overlaps between resistivities belonging to dry and wet conditions, respectively, can be evaluated. Therefore, the difference between the logarithmic mean resistivities of both conditions was related to the standard deviation of this difference. The standard deviation can be expressed in terms of the sum of the variances of the resistivities:

$$\tau_j = \frac{\log_{10}(\bar{\rho}_{b,j}^d) - \log_{10}(\bar{\rho}_{b,j}^w)}{\sigma_j(\log_{10}(\bar{\rho}_{b,j}^d) - \log_{10}(\bar{\rho}_{b,j}^w))} = \frac{\log_{10}(\bar{\rho}_{b,j}^d) - \log_{10}(\bar{\rho}_{b,j}^w)}{\sqrt{\sigma_j^2(\log_{10}(\bar{\rho}_{b,j}^d)) + \sigma_j^2(\log_{10}(\bar{\rho}_{b,j}^w))}} \quad j = 1, \dots, M \quad [4.7]$$

This parameter is also used as test statistic when employing a Student's t-test. The calculation was again performed pixel-wise for the non-robust inversion schemes, the results are presented in Fig. 4.13.

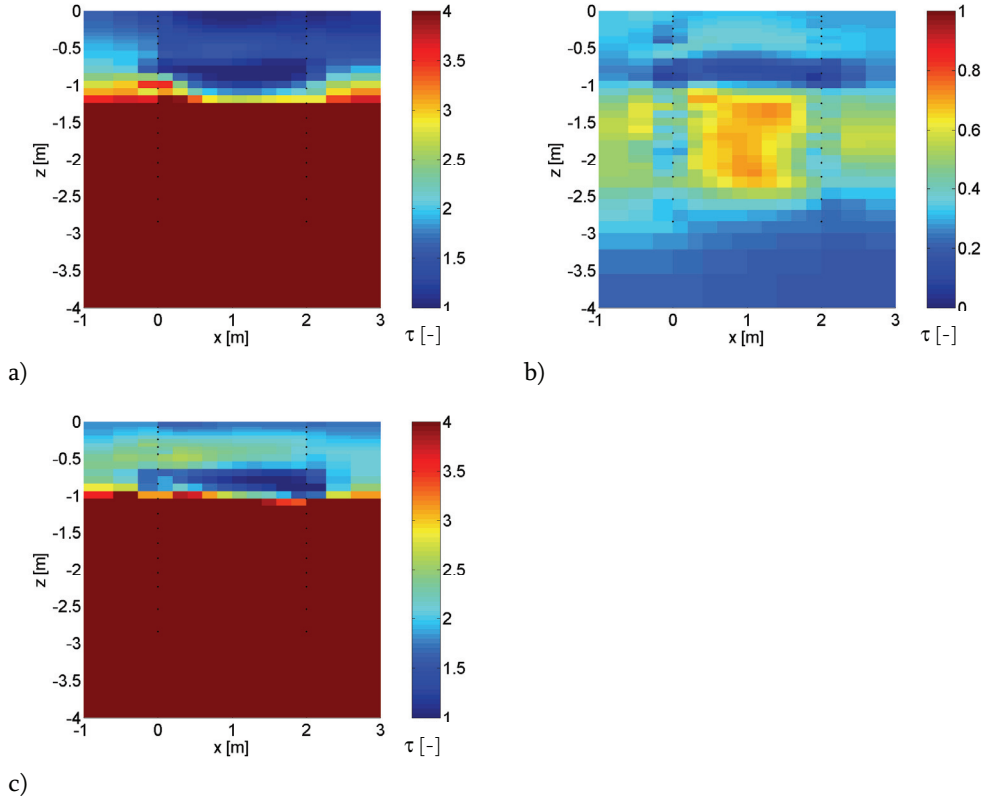


Fig. 4.13: Distributions of test statistic τ for different treatments of data sets, results are shown for the non-robust inversion scheme.

a) Based on fREM. b) Based on CEM (be aware of different plot scale). c) Based on fCEM.

Assuming the difference between mean dry and wet resistivity to be in the same magnitude of order as its standard deviation, we expect τ to be in the range of one. Therefore, τ is generally desired to be much greater than 1. Lowest values (even much smaller than 1) are obtained in case of the CEM treatment (Fig. 4.13b). This result is not surprising when remembering the huge variabilities occurring in that case (Fig. 4.9b). Regarding the plots based on fREM (Fig. 4.13a) and fCEM (Fig. 4.13c), the upper limit of

the plotscale is fixed at $\tau = 4$ so that significant changes are indicated by the dark-red color. The general pattern of both cases is rather similar: Significant changes are given only in a depth below 1 m. Here, the difference between the means exceeds the standard deviation often by a factor of 10 (not recognizable from the Fig.). Above 1 m depth, the results produced by the fCEM method lead to τ -values of about 2, whereas the distribution from the fREM method is dominated by mean resistivities which difference is in the range of their standard deviation, i.e., $\tau \approx 1$. This phenomenon is particularly important with regard to hydrologic aspects, since changes in soil water content become most evident close to the surface. Due to the fact that extreme soil moisture conditions were taken as basis for this study, it is questionable whether the near surface resistivities obtained by ERT are an appropriate mean to derive soil water contents in this specific survey when high data errors are present. However, it is obvious that the sensitivity to changes in water content within the soil profile (Fig. 4.13c) is related to the vertical distribution of the electrical conductivities (Fig. 4.12a): The obtained τ -values are larger in the region of higher electrical conductivities. Therefore, the detection of changes in water content nearby the surface might be more effective when investigating a more homogeneous soil profile regarding the vertical distribution of resistivities.

4.5 Conclusions

In this study, the impact of data errors on the uncertainty in bulk soil electrical conductivity, σ_b , derived from ERT borehole measurements was assessed. Mean and coefficient of variation of σ_b were calculated by means of a Monte Carlo approach for two earth models, a saturated and a dry soil profile. For both cases, a heavily layered earth model with a highly resistive top soil layer and a more conductive subsoil was obtained due to the local pedology. The corresponding resistances of 220 dipole-dipole configurations that were calculated for both earth models using a forward model were noised with random errors. The distribution of measurement errors was derived from normal-reciprocal measurements and shown to depend on the electrode configuration rather than on the measured resistance as it is usually assumed in ERT error models. The error distribution was characterized by long tails, which could not be reproduced by a Gaussian distribution.

The results of the Monte Carlo analysis show that the high resistive horizon at the surface is not properly reproduced but underestimated by the inversion. Using a robust inversion scheme even resulted in smaller estimates of the resistivities in the top soil layer. The variability of inverted resistivity distributions could be reduced effectively by filtering measurements with high data errors. Regarding the first aim of this study, to evaluate data errors as correctly as possible, it must be noted that normal and reciprocal measurements are needed to identify the magnitude of error. Also an error model that depends on the electrode configuration rather than the measured resistance reduced the variability of the inverted σ_b distributions. A second aim was to check the applicability of ERT in this field survey for monitoring changes in soil moisture: A statistically based investigation of the differences between dry and wet conditions showed that the difference between the mean resistivities is in the same magnitude of order as its standard deviation in the near surface region. This might cause an overlap of resulting resistivity distributions when taking data sets under dry and wet soil conditions, respectively. Therefore, it is recommended to reduce the data errors as much as possible in the field (e.g., by reducing the transfer resistances at the electrodes) and to look for an appropriate electrode array in consideration of the error dependence on the electrode configuration. Further investigation is needed to implement this error information into the inversion process.

5 Determination of Seasonal Water Content Dynamics in a Forest Soil Using Electrical Resistivity Tomography

5.1 Abstract

A study was performed to monitor changes in soil water content by means of cross-hole electrical resistivity tomography (ERT). A period of dewatering was chosen to calibrate the relationship between bulk electrical conductivity, σ_b , obtained from ERT and the soil water content, θ , measured by time domain reflectometry (TDR). This petrophysical relationship was used to derive mean water contents in an ERT image plane for a period of nine months. Due to data noise, ERT based σ_b exhibited a high variability in time. Hence, a median filter over time was applied to σ_b before the translation in water contents was carried out. The plausibility of the imaged spatial distributions of soil water content changes was verified in three manners: a) ERT- θ was compared with TDR- θ during the given period. Additionally, the impact of two different error models (errors depending on the resistance or on the electrode configuration) in the geophysical inversion on ERT- θ was investigated. b) Using a soil water balance model, it was proven that the total ERT- θ down to a depth of 2 m was in agreement with TDR- θ as well as with the upper boundary condition determined by precipitation and eddy covariance measurements of evapotranspiration. c) The spatial distribution of θ was analyzed by ERT during a heavy rain event in January 2007, which occurred with the passage of a hurricane, as well as during a long-term period.

All of those case studies confirmed the suitability of ERT to describe dynamics in soil water content. The agreement with different measurement techniques as well as the plausibility of imaging spatial soil water changes demonstrated the additional benefit when a median filter was applied to noisy time-lapse inversion results. However, more sophisticated analyzing techniques are needed to reduce the roughness of the resulting water content distributions in space and time, respectively.

5.2 Introduction

An explicit knowledge of the stored water in soils is required by agronomic, ecological, and hydrological communities to understand water distributions and flow processes. Additionally, modified natural boundary conditions due to climate change such as heavy rainfall events and dry spells have a direct impact on the soil water balance so that reliable monitoring techniques of soil moisture are required. A detailed overview of numerous methods to measure soil moisture in the vadose zone is given by Vereecken et al. (2008) and Robinson et al. (2008). Robinson et al. (2008) pointed out that there exist significant gaps regarding the measurement scale, which are caused by two different historical directions of development: Point measurements have been predominantly developed for applications in agriculture to understand field-scale soil water dynamics, whereas satellite remote sensing has been developed to understand the hydrology up to the global scale. Hence, they concluded that new technologies and methods such as geophysical methods and sensor networks form a bridge between current sensor and remote sensing capabilities. A summary of several geophysical methods applied in hydrology is given by Vereecken et al. (2005). One geophysical method is based on a four-electrode setup to infer the electrical conductivity of soils and rocks from resistance measurements. Robinson et al. (2008) cite Briggs (1899) to be the first author who worked on the derivation of soil water contents from those measurements. When resistivity techniques were applied at the field scale, their use was first not very practical because of the difficulty to address the huge amount of electrodes manually. With further development of data acquisition systems and first inversion routines, the imaging capability of resistivity methods became suitable in environmental and engineering problems to investigate the subsurface in a high spatial resolution (Daily et al., 2004). This technique is referred to as electrical resistivity tomography (ERT). Since bulk electrical conductivity is highly affected by the moisture status of the medium, ERT was more and more implemented in hydrology to derive soil water contents in a high spatial resolution. For such applications, a detailed knowledge of the underlying petrophysical relationship between apparent electrical resistivity, texture, soluble salt concentration, and the soil volumetric water content is required. Different relationships were introduced empirically and semi-empirically by several authors (e.g., Archie, 1942; Rhoades et al., 1976; Mualem and Friedman, 1991). Those relationships permitted the derivation of spatial soil water

content distributions at the field scale during infiltration experiments (e.g., Daily et al., 1992; Park, 1998; Binley et al., 2002a; Deiana et al., 2008; Batlle-Aguilar et al., 2009; Cassiani et al., 2009). But also in studies which dealt with the monitoring of naturally occurring changes in soil moisture, ERT was applied with oftentimes promising results (Zhou et al., 2001; Binley et al., 2002b; Zhou et al., 2002; Michot et al., 2003; Amidu, 2007; Miller et al., 2008; Rings et al., 2008; Schwartz et al., 2008). However, only few authors evaluated ERT derived soil moisture quantitatively by means of a comparison with independent measurements (e.g., TDR, heat-probe-type sensors, gravimetric methods) serving as ground truth. In such comparisons, clear correlations between ERT based soil moisture and independently measured values were found. However, resulting coefficients of determination of about 0.67 (Zhou et al., 2001), 0.46 (Michot et al., 2003), and 0.57 (Schwartz et al., 2008) show that there is still a conspicuous uncertainty contained in the ERT derived water contents (assuming the comparing technique to be justified and reliable).

Uncertainty is mainly introduced by the limited resolution of ERT which depends on several factors, namely measurement physics, parameterization, regularization, measurement errors, and spatial variability (Day-Lewis et al., 2005). Oldenburg and Li (1999) have shown that particularly measurements with electrodes that are positioned at the surface exhibit a boundary below which the earth structure is no longer constrained by the data. This is mainly caused by the fact that the sensitivity is highly decreasing with distance from the electrodes (Singha and Gorelick, 2006). One solution to overcome this problem in soil science is the use of borehole electrodes to approach the object of interest. However, the information content is low in the center between two boreholes (Day-Lewis et al., 2005). A further issue with borehole measurements is an increased noise level caused by a poor contact between the electrodes and the soil. To reduce the transfer resistances it is common to backfill the boreholes with conductive material such as bentonite. However, the contrast in resistivity between the fill and the host material leads to an additional source of error (Nimmer et al., 2008). Furthermore, the resolution of ERT is influenced by the survey design (Day-Lewis et al., 2005), i.e., the relative location and distance of transmitter and receiver electrodes. Depending on the purpose of the measurement, different electrode configurations are assumed to be appropriate: For instance, dipole-dipole arrays seem to be the method of choice if lateral structures or changes in near-surface resistivity should be investigated (Barker, 1998) which is actually the purpose of soil moisture monitoring as it is presented here. But, for cross-hole dipole-dipole measurements where the current dipole is placed in one borehole and the voltage dipole in the other many data close to zero are obtained leading to a low signal-to-noise ratio (Zhou and Greenhalgh, 2000). In this regard borehole surveys are actually

counterproductive since those conspicuous measurement errors influence the image resolution negatively (Day-Lewis et al., 2005). Therefore, data with relative errors larger than 10 % must often be removed prior to inversion (e.g., Binley et al., 2002a; Deiana et al., 2008; Cassiani et al., 2009). However, cross-hole dipole-dipole measurements were used for the current study to capture also the soil water dynamics in the near-surface area. Besides the electrode configuration and the related relative measurement errors, also the quantification of the error level plays a crucial role since the inversion of the raw ERT data is affected critically by the assessment of the measurement error level. This is typically assessed using an error model which is implemented in the inversion scheme (Binley et al., 1995; LaBrecque et al., 1996).

In the current study, the quantitative analysis of a long-term monitoring of soil water contents in a forest by means of cross-hole ERT is addressed. A first objective of the paper is to use water balance calculations as an alternative verification method of ERT- θ besides correlations between ERT- θ and TDR- θ . Using a soil water balance as a means to verify ERT- θ exploits the capability of the ERT method to obtain a full coverage of the soil moisture distribution in the soil profile. The latter is obviously a limitation when sparse local soil moisture measurements must be interpolated. A second objective is to evaluate the impact of the error level assessment on the derived soil moisture distributions. Two different error models were used: a model that is commonly used and which assesses the error level based on the measured resistance (Binley et al., 1995; LaBrecque et al., 1996) and a model that assesses the error level for each measurement configuration separately. In a nutshell, the aim of the current study is the application of ERT to monitor water contents of a heterogeneous forest soil, taking into account a high level of data errors.

5.3 Materials and Methods

In the current study, the petrophysical relationship was derived from field data with σ_b obtained from ERT and TDR based θ during a wetting period. Here, TDR measurements of all trenches served as input and were related to σ_b measurements in the closest ERT planes, namely at $y=0$ and $y=10$ m (Fig. 2.3). After that, this calibration was used to transform inverted ERT resistivities of plane $y=6$ m to water contents. Finally, those water contents were evaluated by means of three criteria: a) The ERT based water contents were compared with those obtained from TDR. b) It was investigated whether precipitation and evapotranspiration were balanced by changes in soil water storage that were derived from ERT measurements. c) Changes in soil moisture due to rainfall events during the passage of a hurricane in January 2007 and due to seasonal variations caused by tree root water uptake were analyzed to demonstrate the capability of ERT to monitor soil water contents spatially.

5.3.1 ERT Data Processing

ERT Data Filtering

For the inversion, data sets were filtered previously. The first criterion was a sufficiently large injection current, so only data with injections greater than 0.09 mA were kept. The second criterion was the coefficient of variation derived from the voltage trace of each measurement, CV_i (Eq. [3.4]). Only measurements with $CV_i < 0.05$ were taken into account for the following analysis.

ERT Error Estimation

Before any inversion of ERT data was started, an accurate evaluation of measurement errors was done. Therefore, we performed all the measurements in a reciprocal manner, meaning that after each measurement the measurement is repeated with interchanged current and voltage dipoles to obtain a guess of the data error. The outcome of the synthetic error analysis performed in chapter 4 was that most accurate inversion results were obtained when an error model was defined for each individual electrode configuration (referred to as configuration dependent error model, CEM) after an appropriate approach of raw data filtering. In this case, CEM led to more precise results

than the commonly used error model in which the error level is linearly dependent on the resistance (referred to as resistance dependent error model, REM). In this chapter, the two methods are compared for real data.

Parameterization of both error models was derived separately for all planes used in this study ($y=0$; $y=6$ m; $y=10$ m). The data basis for the analysis was a set of measurements taken in the period between June 2, 2006 and April 29, 2007. Since only a beta version of the measurement software was available, the data acquisition during a survey of the entire field plot was not always complete so that for some data sets measurements in certain planes or its reciprocals were missing. This led to different numbers of normal-reciprocal data sets of the respective planes: 72, 82, and 72 for planes $y=0$, $y=6$ m, and $y=10$ m, respectively.

For both error models, the final aim was an specific error weighting for each measured datum during the inversion, where the diagonal of the data weighting matrix, \mathbf{W}_d , (Eq. [3.17]) consists of the standard deviation, ε_i , of the i -th datum, d_i , i.e., $\varepsilon_i = \sigma(\ln R_i)$. From normal-reciprocal error estimations, only the standard deviations of the normal-reciprocal differences, $\sigma(\Delta \ln R_i)$, are derived. In order to obtain a large time series of ERT data sets, either normal or reciprocal measurements were inverted later on instead of the mean, dependent on their availability. Hence, standard deviations $\sigma(\ln R_{i,nor})$ and $\sigma(\ln R_{i,rec})$ obtained by Eq. [4.3] were used.

a) Error Model Dependent on Electrode Configuration (CEM)

Similar to chapter 4, for each electrode configuration, a frequency distribution of the normal-reciprocal error (Eq. [3.23]) was derived. This led to 1130 distributions for 1130 electrode configurations of 72 and 82 normal-reciprocal measurement errors in planes $y=0$ and $y=6$ m, respectively. In case of plane $y=10$ m, the number of distributions or configurations amounted only 964 since there was a broken electrode stick, allowing no control of electrodes 551 to 555 (Fig. 2.3). A robust estimator (Eq. [4.1]) was used to derive a standard deviation of a Gaussian error distribution that approximates the real error distribution.

b) Error Model Dependent on Resistance (REM)

For each plane, the range between the minimal and the maximal resistance was divided into hundred bins. For each bin, the standard deviation of the respective difference in normal-reciprocal resistance, $\sigma(\Delta \ln R)$, was calculated according to Eq. [4.2]. Due to the deviation of the error distribution from a Gaussian (i.e., high peaks and long tailings), again a robust estimator was used for the standard deviation (Eq. [4.1]). Finally, the linear error model (Eq. [3.24]) was fitted to the bin-wise estimated standard deviations.

Geoelectrical Inversion

ERT resistances were inverted by means of the finite element code “CRTomo” (Kemna et al., 2000). To account for higher dynamics in water contents and electrical conductivity close to the soil surface, the resolution of the grid for the geoelectrical inversion was increased at the top (Fig. 5.1).

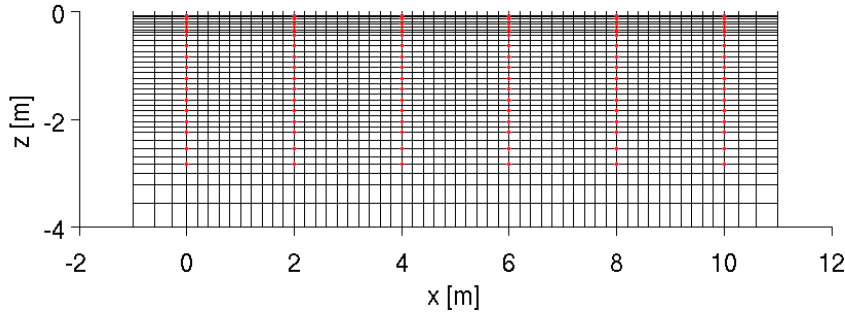


Fig. 5.1: Exemplary grid illustrated for plane $y=6$ m. Red dots indicate electrode positions.

5.3.2 Calibration of Field-Scale Petrophysical Relationship

The calibration of the petrophysical relationship was evaluated from field data with σ_b obtained from ERT and θ derived from TDR measurements. The calibration procedure was performed twice: once for the CEM and once for the REM model.

For the calibration, inverted ERT data of the planes which are nearby calibration trenches served as input (i.e., $y=0$ and $y=10$ m). The petrophysical relationship was derived from measurements during the period from November 24, 2006 until February 8, 2007, which was characterized by a continuous increase in soil water content. This resulted in 19 data sets that were used for calibration. On the basis of the classification of the soil (Fig. 2.2), the calibration was derived for each horizon. Each inverted data set was corrected for temperature according to Eq. [3.30]. Here, the mean temperature recorded by temperature probes installed in all trenches (Tab. 2.2) was calculated for each depth. Subsequently, those values were interpolated in the z -direction.

Afterwards, a calibration relation was established between σ_b and θ measurements that were both averaged in space and in time. For the spatial average, all TDR and ERT image pixels measurements at a given time and at the same depth were averaged by taking the median. This led to only one TDR water content value, θ^{TDR} , and one ERT electrical

conductivity value, σ_b^{ERT} , per depth. Subsequently, an averaging of five consecutive measurements in time was performed, i.e., using a median filter of the order $\mu = 4$:

$$\sigma_{b,f}^{ERT}(\pi) = \tilde{\sigma}_b^{ERT}(\pi - \mu/2, \pi - \mu/2 + 1, \dots, \pi - \mu/2 + \mu), \quad [5.1]$$

with

$$\pi = 1 + \mu/2, \dots, \Pi - \mu/2,$$

where f means “filtered”, $\tilde{\sigma}_b^{ERT}$ is the median, and Π is the number of data sets (here: $\Pi = 19$). The same filter was applied to θ^{TDR} .

This averaging procedure was necessary to obtain a significant relation between σ_b^{ERT} and θ^{TDR} . A direct comparison of measurements at a single location and one time showed only a weak correlation due to differences in sampling/ averaging volume of the different methods and due to data noise.

Finally, the petrophysical relationship between θ_f^{TDR} and $\sigma_{b,f}^{ERT}$ was calibrated for each soil horizon defined by the soil profile description (Fig. 2.2a). Hence, θ_f^{TDR} (and related $\sigma_{b,f}^{ERT}$, respectively,) of different depths were merged with respect to the horizon where they were located in (Tab. 2.1). Usually, a power-law equation is used to relate σ_b and θ (e.g., Archie, 1942). However, since data are noisy and the range of θ is small, the nonlinear equation was approximated by a linear relationship:

$$\theta = a \sigma_b + b, \quad [5.2]$$

where a and b are fitting parameters.

5.3.3 Application of Field-Scale Petrophysical Relationship

The petrophysical relationship was tested in three different ways:

First, ERT and TDR derived water contents were compared for a different period to investigate whether the derived petrophysical relation can also be used to describe the dynamics of the water content in the soil profile under different conditions. Second, it was investigated whether the plot-scale water balance can be closed using the fluxes that were measured at the soil surface and the changes in water content in the field plot that were derived from ERT. Third, the petrophysical relations were used to demonstrate the capability of ERT to monitor the spatial soil water content distribution during the passage of a hurricane in January 2007 as well as during a long-term period.

5.3.3.1 Comparison with TDR

A first validation was performed by applying the field based relationship to ERT data obtained from plane $y=6$ m. The period with available measurements was between June 2, 2006 and March 30, 2007, including 83 data sets. Therefore, the time window of validation extended the calibration period considerably. Additionally, in this section a comparison was performed between electrical conductivities which were inverted with the CEM and REM model, respectively. For each data set, the ERT measurements were processed in the same way as for the petrophysical model calibration and $\sigma_{b,f}^{ERT}$ was transformed to desired water contents, θ_f^{ERT} , using Eq. [5.2].

To check for reliability, the median filtered TDR water contents of all transects, θ_f^{TDR} were compared for each depth with θ_f^{ERT} . TDR based water content was obtained from averaged measurements during an ERT survey. Furthermore, the 5th and 95th percentiles of ERT derived filtered water contents were derived from all pixels of one depth related to a TDR probe. This was done in order to investigate whether any differences between θ_f^{ERT} and θ_f^{TDR} can be related to the spatial variability of the soil water content.

The correlation between θ_f^{ERT} and θ_f^{TDR} was calculated for each depth. In addition, the root mean square error, $RMSE$, was calculated. In order to compare the quality of ERT predicted water contents for different depths, the $RMSE$ was normalized by the mean TDR water content

$$CV(RMSE) = \frac{RMSE}{\frac{1}{\Pi} \sum_{\pi=1}^{\Pi} \theta_{f,\pi}^{TDR}} = \frac{\sqrt{\frac{1}{\Pi} \sum_{\pi=1}^{\Pi} (\theta_{f,\pi}^{ERT} - \theta_{f,\pi}^{TDR})^2}}{\frac{1}{\Pi} \sum_{\pi=1}^{\Pi} \theta_{f,\pi}^{TDR}}. \quad [5.3]$$

5.3.3.2 Generation of a Water Balance

An additional verification consisted of a water balance that was derived from the hydrological boundary conditions and the change in soil water storage. For the upper boundary condition, the difference between precipitation and actual evapotranspiration was calculated. Soil water storage was derived from ERT and TDR measurements. For the derivation of ERT- θ , electrical resistances were only inverted with the CEM model.

Determination of Throughfall

Precipitation data were obtained from the meteorological station of the research centre and were corrected for interception of the canopy. A calibration relation between rainfall and throughfall was established using measurements from July 1, 2005 to December 23, 2005. Throughfall was measured by means of rain gauges which were installed on top of the ERT electrode sticks. Fig. 5.2 shows the relationship derived from free precipitation rate, P_f , and throughfall, P .

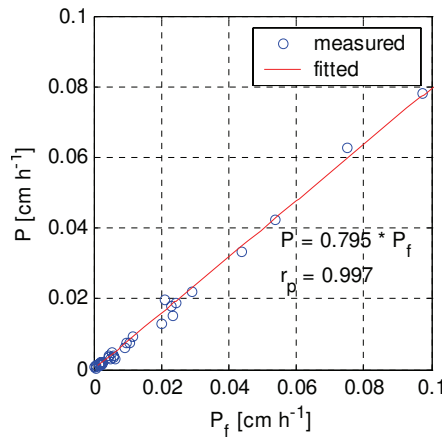


Fig. 5.2: Relationship between free precipitation rate, P_f , and throughfall, P .

Fig 5.2 shows a strong linear relationship (correlation coefficient: $r_p = 0.997$) between free precipitation and throughfall, which is 79.5 % of the free precipitation rate.

Determination of Actual Evapotranspiration

Actual evapotranspiration was derived from eddy covariance measurements. The method calculates the net vertical flux of trace gases within the atmospheric boundary layer, F_c , from the correlation between trace gas density (here: water vapor), ρ_c , and the vertical wind speed component, w , with

$$F_c = \overline{w \cdot \rho_c} . \quad [5.4]$$

Relating F_c to the density of water, ρ_w , a volume flux density is obtained which is defined as evapotranspiration flux

$$ET = -\frac{F_c}{\rho_w} . \quad [5.5]$$

Here, the minus sign is inserted since ET is assumed to be oppositely directed to the precipitation flux. A detailed description of the eddy covariance method can be found, for instance, in the works of Ammann (1999), Kaimal and Finnigan (1994), or Van Dijk et al. (2004).

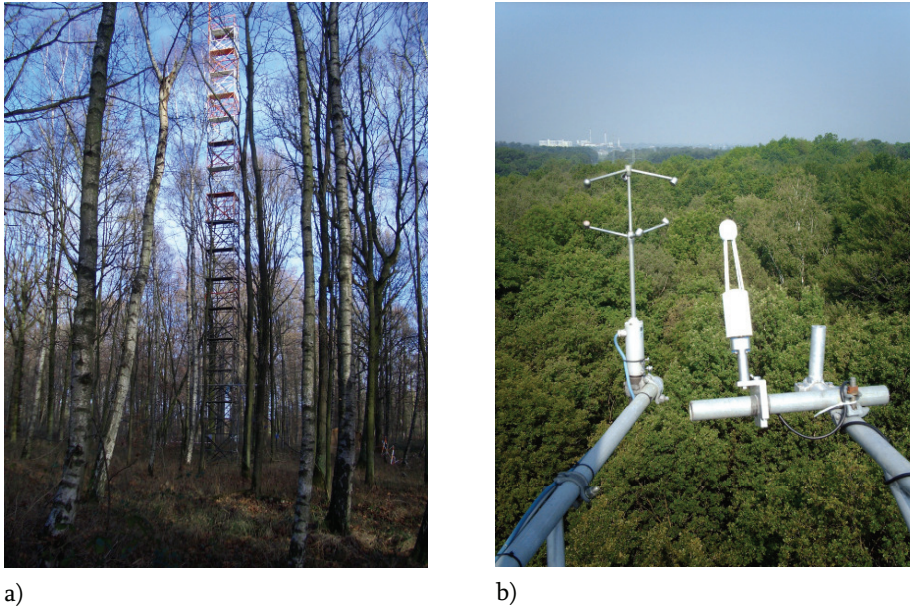


Fig. 5.3: a) Observation tower for eddy covariance measurements. b) Ultrasonic anemometer and open path analyzer mounted on top of the tower.

The eddy covariance method requires a high temporal resolution of both trace gas concentration and wind speed measurements which have to be accurately synchronized. The data acquisition was performed by an USA-1 ultrasonic anemometer (Metek, Elmshorn, Germany) and a Li-7500 open path infrared gas analyzer for CO_2 and H_2O density fluctuations (Li-Cor, Lincoln, NE, USA) which both were mounted on the top of an observation tower (height: 37 m, top 15 m above canopy) in the forest, 90 m distant from the field plot (Fig. 5.3). A sonic anemometer measures the speed of sound in air using a short burst of ultrasound transmitted via a transducer. Another transducer detects the reflections of the sound. The travel time of the sound is dependent on the wind speed. The open path analyzer samples water vapor (and also carbon dioxide) densities using absorption measurements of radiation in the infrared region of the electromagnetic spectrum. The sampling frequency of both instruments amounted 10 Hz. Device control and data logging were performed by a personal computer placed in a nearby cabin using a RS-232 connection, controlled by the software “knusalic” (Knaps, 2006). Processing of the

raw data to fluxes was performed offline with a custom software, that has been tested to provide similar results as the softwares TK2 (Mauder and Foken, 2004) and ECpack (Van Dijk et al., 2004). It included a despiking (Vickers and Mahrt, 1997), cross-correlation alignment (Mauder and Foken, 2004) and detrending of the raw data, as well as elimination of values where the AGC (automatic gain control) values of the Li-7500 indicated presence of excess rain or dew in the measurement path. Turbulence statistics were subject to a double rotation of the wind data coordinate system (Kaimal and Finnigan, 1994), frequency response correction (Moore, 1986), sonic temperature and heat flux correction (Schotanus et al., 1983), and density fluctuation correction (Webb et al., 1980) before calculating fluxes on a half-hourly basis. Only those fluxes were used here, where at least 90 % of the raw data records were present and valid, excluding the upper and lower 0.1 %-quantile. Half-hourly fluxes were then aggregated to hourly resolution. A time series of resulting ET derived from eddy covariance data performed from summer 2006 to spring 2007 is shown in Fig. 5.4. The annual course characterized by highest evapotranspiration fluxes in the mid of July and lowest at the end of December is clearly represented.

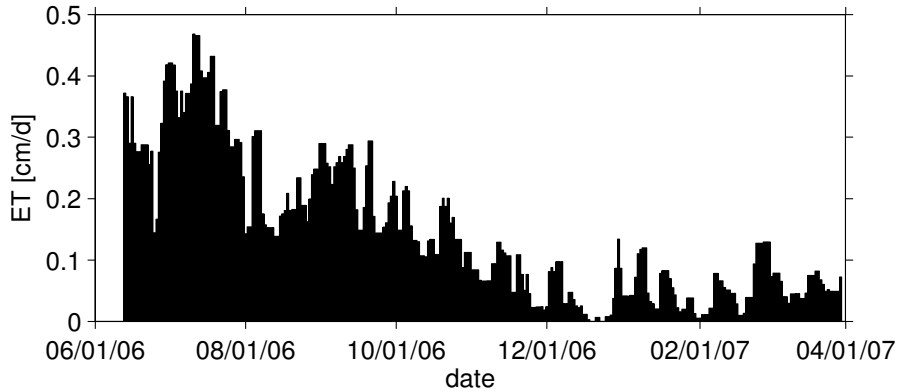


Fig. 5.4: Time series of evapotranspiration flux, ET , derived from eddy covariance measurements in the period June 2006 to April 2007.

Water balance

The cumulative height of supplied water at the upper boundary, PET , was derived from the throughfall, P , and evapotranspiration flux, ET :

$$PET_p = (P_p + ET_p)(t_p - t_{p-1}) + PET_{p-1}, \quad [5.6]$$

where PET_p was calculated between time $t_0 = 0$ (with $PET_0 = 0$) and the p^{th} measurement time t_p . P and ET data were processed on daily basis.

The change in water content within the soil profile was derived separately from TDR and ERT measurements and determined by

$$H_h = \sum_{\omega=1}^Z (\theta_{\omega,h} - \theta_{\omega,0}) \Delta z_{\omega}, \quad [5.7]$$

where $\theta_{\omega,h}$ is the water content at the h^{th} measurement time, t_h , and in the ω^{th} depth interval, Δz_{ω} , is the thickness of the depth interval, and $\theta_{\omega,0}$ is the initial water content. Note that different subscripts were used for PET_p and H_h since ERT measurements were not performed on daily basis, leading to different measurement times. The soil was divided into $Z = 8$ compartments. The compartment boundaries were at the center between the TDR depths (see table 5.1). The bottom of the lowest compartment was defined at 200 cm depth. In order to generate a closed water balance, it was assumed that there is no root water uptake below this depth. This assumption is justified since Kuhr (2000) reports on a maximal rooting depth of 120 cm for a tree population of species *Fagus sylvatica* L., also grown on a Stagnic Luvisol. Furthermore, no roots were observed below 120 cm depth in the trenches that were dug out for the installation of the TDR probes.

Tab. 5.1: Derivation of compartment thickness, Δz_ω , for the derivation of the water balance.

index of compartment, ω	depth of TDR/ bottom depth [cm], z_ω	compartment thickness, Δz_ω [cm]
1	5	6.25
2	7.5	4.5
3	14	8.25
4	24	15
5	44	30
6	84	40
7	124	50
8	184	46
	200	

Finally, PET and H were plotted in the same diagram. Assuming no lateral flow, the difference between PET and H is equal to the cumulative amount of water that crossed the bottom boundary of the soil profile. An increase of $PET - H$ with time corresponds with a period of outflow or drainage from the soil profile whereas a decrease in $PET - H$ corresponds with inflow or capillary rise. The water balance was calculated for the period between June 13, 2006 ($t = 0$) and March 30, 2007 when all data (ERT, TDR, and eddy covariance measurements) were available.

Determination of Depth to Groundwater Table

In order to compare water contents derived from ERT additionally, the depth to groundwater table, GWL , was derived from readings of an observation well 130 m apart from the field plot. Measurements were performed monthly and corrected for the elevation of the field plot. Due to the distance of the observation well relative changes in groundwater level seem to be more reliable than its absolute values.

5.3.3.3 Monitoring of Spatiotemporal Soil Water Content Changes

Observation of Soil Water Content Changes due to a Single Rainfall Event

The capability of ERT to monitor seasonal changes in soil water contents was already addressed in the previous sub-sections. In this section, it is evaluated whether single rain events can still be monitored when a median filter is applied. In addition, the spatial distribution of the soil water content changes is investigated. Therefore, a time period

between January 12 and February 8, 2007 was selected in which a heavy rain event occurred during a windstorm and in which 10 ERT data sets were recorded. For the following analysis only data from plane $y=6$ m that were inverted with the CEM model were considered.

Generally, the approach to derive water contents was similar to that described in chapter 5.3.3.1 but the order of the filter was reduced to $\mu = 2$. Otherwise the averaging time would be too large to analyze a single rain event. The filtered $\sigma_{b,f}^{ERT}$ were translated to water contents, θ_f^{ERT} , using soil horizon specific petrophysical relationships (Eq. [5.2]). In order to visualize relative changes in soil water contents, differences were related to a reference distribution taken at 2007/01/12.

Since the rainfall during the passage of the storm was large and likely much larger than the downward flux at the bottom of the soil profile, the change in soil water during and shortly after the storm should be equal to the throughfall. Hence, a water balance starting from January 12, 2007 was established in the same manner as in the previous section.

Observation of Seasonal Soil Water Content Changes

In order to investigate not only spatiotemporal changes in soil water contents during a short-term period but also during several months containing summer and winter, relative changes between June 2006 and March 2007 were computed pixel-wise for plane $y=6$ m. The procedure to derive water contents was again related to chapter 5.3.3.1 (order of median filter: $\mu = 4$). For the calculation of relative changes, the water content distribution of 2006/06/13 served as reference state and 14 distributions of water content changes were plotted exemplarily.

5.4 Results and Discussion

5.4.1 ERT Data Processing

ERT Error Estimation

a) Error Model Dependent on Electrode Configuration (CEM)

Three error distributions obtained from normal-reciprocal measurements of an exemplary electrode configuration: C1: 20, C2: 23, P1: 35, P2: 39, are shown in Fig. 5.5 for three different planes: $y=0$ m, $y=6$ m, and $y=10$ m. Both current and potential dipoles are located in the center of the borehole. In planes $y=0$ and $y=10$ m, this configuration is located in direct vicinity of a trench. For both planes, the error distribution deviates considerably from the Gaussian distribution with a regularly derived standard deviation (black line, Fig. 5.5). This illustrates that an error model that uses the standard deviation of a Gaussian error distribution largely underestimates the probability density of measurements with a small error. Since the model misfit is weighted by the measurement error in the ERT data inversion, an underestimation of the probability density of small measurement errors will lead to an acceptance of larger model misfits. In order to obtain a better description of the probability density of the small measurement errors by a Gaussian distribution, a robust estimator of the standard deviation, $\sigma(\Delta \ln R)$, was used according to Eq. [4.1]. For the exemplary distributions shown in Fig. 5.5, this results in robust estimators, $\sigma(\Delta \ln R_{\text{examp}})$, presented in Tab. 5.2.

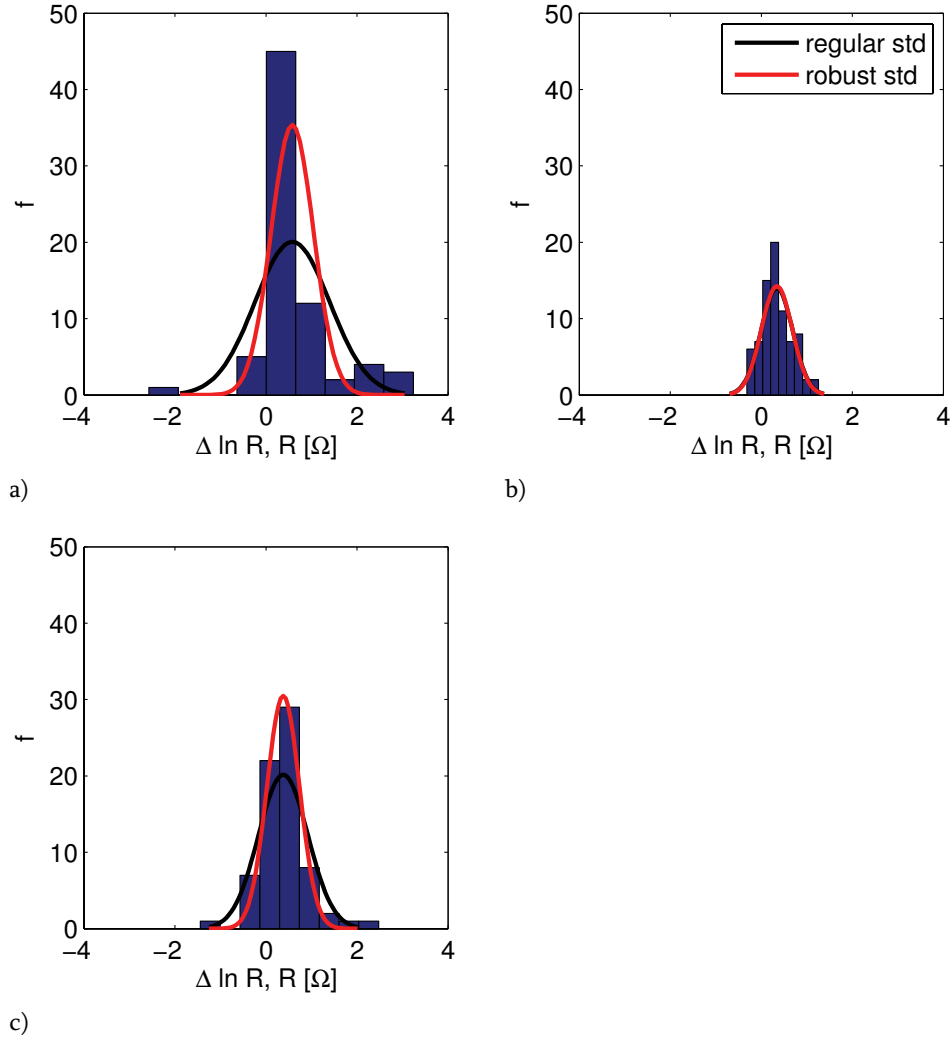


Fig. 5.5: Error distribution derived from normal-reciprocal measurements for a certain electrode configuration: C1: 20, C2: 23, P1: 35, P2: 39 in plane $y=0$ ($n=72$) a); $y=6$ m ($n=82$) b); $y=10$ m ($n=72$) c).

Black line represents a fitted Gaussian distribution with regular standard deviation, red line a fitted Gaussian with a robust estimator used as standard deviation.

Tab. 5.2: Robust estimated standard deviations from error distributions according to Fig. 5.5 calculated for different planes, $\sigma(\Delta \ln R_{examp})$, $\bar{\sigma}(\Delta \ln R)$ and $std(\sigma(\Delta \ln R))$ are mean and standard deviation of robust estimators of all configurations in the given plane.

	y=0	y=6 m	y=10 m
$\sigma(\Delta \ln R_{examp})$	0.4659	0.3389	0.3594
$\bar{\sigma}(\Delta \ln R)$	0.3228	0.2783	0.4509
$std(\sigma(\Delta \ln R))$	0.4643	0.2916	0.6465

From both the exemplary error and the mean error it is evident that the error is higher for the planes close to a trench (i.e., $y=0$, $y=10$ m). Furthermore, it is obvious that the standard deviation of the robust estimator, $std(\sigma(\Delta \ln R))$, is generally very high for all planes. In case of the central plane, $y=6$ m, it ranges within the level of the mean, whereas it even exceeds the mean considerably for the outer planes ($y=0$, $y=10$ m). Those aspects indicate that the disturbance of the soil as well as the installed instrumentation close to the outer planes could have a negative impact on the quality of ERT measurements. Additionally, it seems likely that the high level of the standard deviation is caused by different error levels depending on the electrode configuration. Therefore, a robust estimator was also derived in dependence on the geometric factor, K , in Fig. 5.6. Here, the range of K values was divided into 10 bins, spanning a width of 100 m each. It is evident that there is a distinct linear relationship between K and $\sigma(\Delta \ln R)$. Based on the coefficients of determination, R_K^2 , there can be explained on average 84.77 % of the variation in error level by this linear relationship for the given division of the bins. However, it is obvious that for the highest bin, [900 m ; 1000 m[, the error level decreases erratically in all planes. This can be explained by the lithology of the field plot: Geometric factors within the bin [800 m ; 900 m[are related to electrode configurations where the lower voltage electrode is located at the borehole bottom, i.e., within a gravel layer. The last bin, namely [900 m ; 1000 m[, is related to measurements with shorter voltage dipole lengths where the lower voltage electrode is coupled to fine textured material, leading to better electrode contact and, therefore, a lower error level.

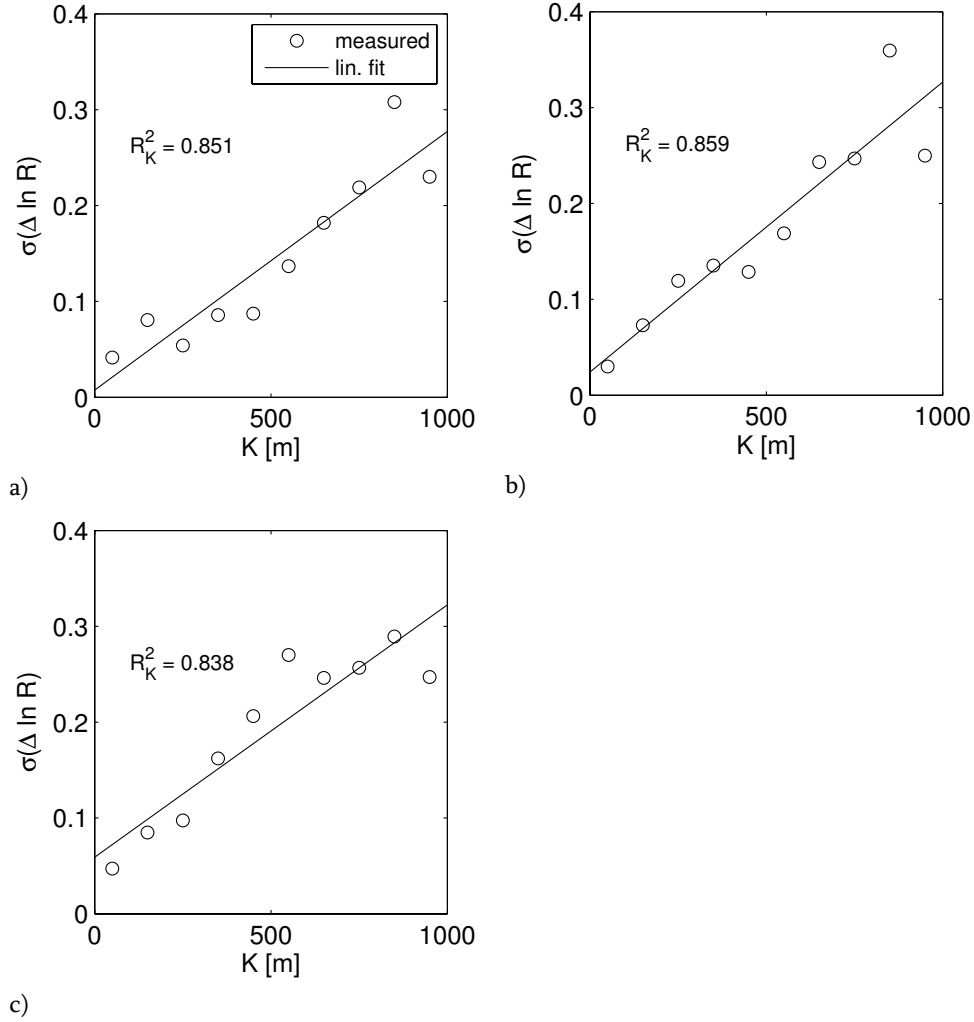


Fig. 5.6: Robust estimated standard deviation of normal-reciprocal error, $\sigma(\Delta \ln R)$, in dependence on geometric factor, K , in plane $y=0$ a); $y=6$ m b); $y=10$ m c).

R_K^2 denotes the coefficient of determination of a linear fit.

Due to the fact that measurements with the same geometric factor led to different error levels (Fig. 5.5) and that particular electrode positions exhibit particular error levels (Fig. 5.6), it is justified to apply an error model which is derived individually for each electrode configuration.

b) Error Model Dependent on Resistance (REM)

The linear error model was derived for each plane ($y=0$, $y=6$ m, $y=10$ m). Standard deviations of each class of resistances and the fitted model are depicted in Fig. 5.7. The error model parameters are given in Tab. 5.3.

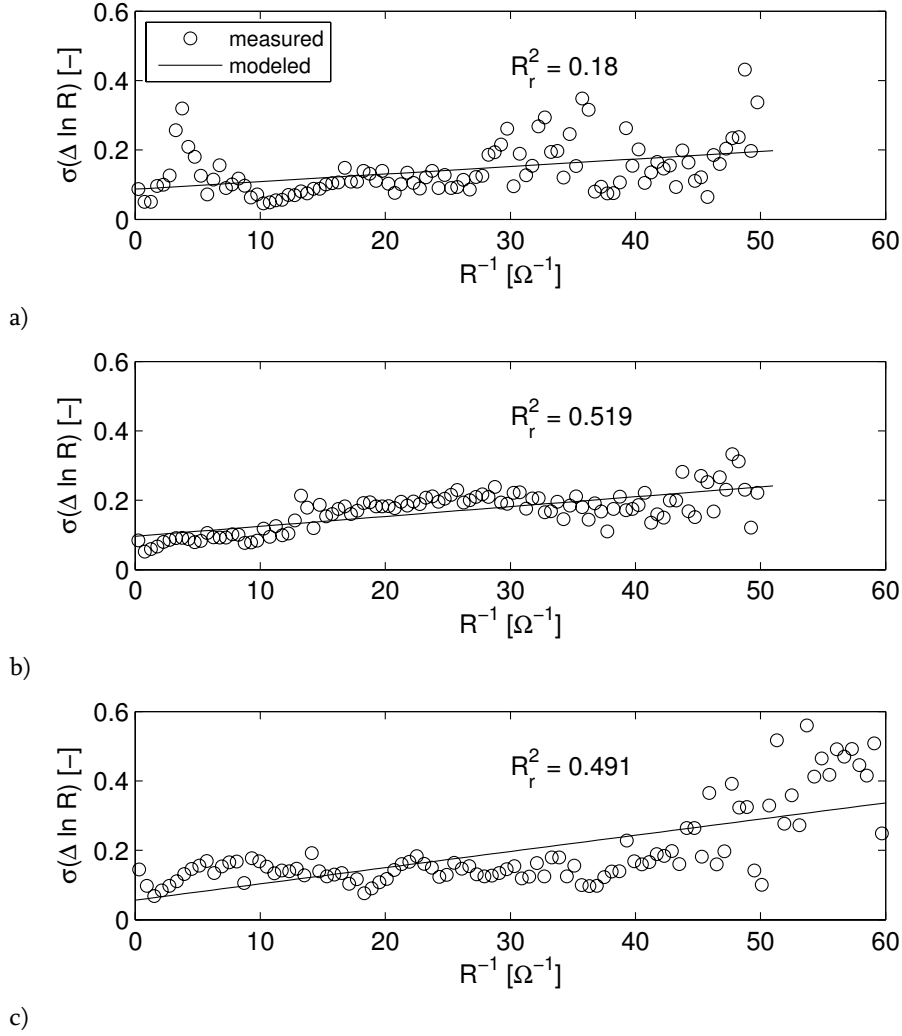


Fig. 5.7: Robust estimated standard deviation of normal-reciprocal error, $\sigma(\Delta \ln R)$, in dependence on the inverse of mean resistance, R^{-1} , in plane $y=0$ a); $y=6$ m b); $y=10$ m c).

R_r^2 denotes the coefficient of determination for the derivation of the linear error model (REM).

Tab. 5.3: Parameterization according to error model (REM) given in Eq. [3.24] for different planes.

	y=0	y=6 m	y=10 m
a_e [-]	6.16 E-02	6.83 E-02	4.00 E-02
b_e [Ω]	1.54 E-03	2.01 E-03	3.31 E-03

The error models seem to be similar for the different planes (Tab. 5.3). It must be noted that the error model does not predict the error level in each resistance class exactly. From the coefficients of determination, R_r^2 , it can be concluded that on average 39.7 % of the variation in error level is explained by this model when the given division of bins is used. As a consequence, for some electrode configurations, this model overestimates or underestimates the error level. This error model tries to describe the error level using only two parameters for each image plane. On the other hand, the number of parameters in the error model that is parameterized for each electrode configuration, CEM, is much higher. Here, the model is not only parameterized for all the configurations of the same geometry as it is in Fig. 5.6 but it is parameterized individually for each electrode configuration. As a consequence, it is obvious that the CEM should better describe the error level.

5.4.2 Calibration of Field-Scale Petrophysical Relationship

a) Error Model Dependent on Electrode Configuration (CEM)

Although data of several depths were merged for the individual horizons (different colors, Fig. 5.8), it is obvious that depths which are in the same soil horizon have more or less the same petrophysical relation. However, the petrophysical relationships seem to vary considerably between the different soil horizons.

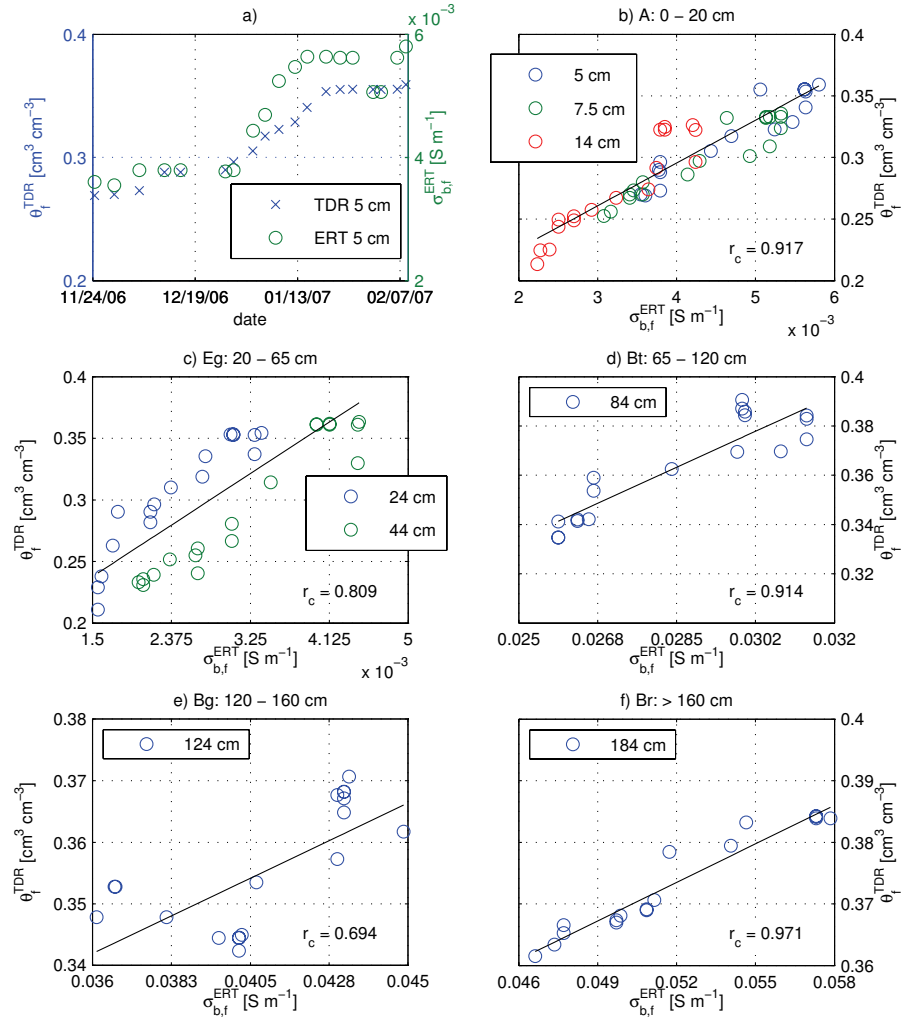


Fig. 5.8: Calibration of the CEM model.

a) Exemplary course of θ_f^{TDR} and $\sigma_{b,f}^{ERT}$ for the calibration period in 5 cm depth.
 b)–f) Petrophysical relationship obtained from θ_f^{TDR} and $\sigma_{b,f}^{ERT}$ for different horizons.

Although it is common to fit a polynomial of higher order to soil petrophysical data, it is evident from Fig. 5.8b–f that the scatter plots are sufficiently described by a linear equation in the form of Eq. [5.2]. Coefficients of linear regression analysis, a (slope) and b (intercept), as well as related correlation coefficients, r_c , are given in Tab. 5.4. Since the range of water contents is not so large, also fits of the more sophisticated Archie law (Archie, 1942) are nearly congruent with straight lines (not shown here). Michot et al. (2003) also found out that a linear relationship derived from field calibration was adequate in their case. However, the regression parameters should not be interpreted as physical parameters. For instance, a more physically based petrophysical model, which also includes the effect of the electrical conductivity of the soil particle surface, would predict a positive bulk electrical conductivity when the volumetric water content approaches the residual water content. Since the surface electrical conductivity is nearly independent on the volumetric water content, the relation between bulk electrical and water content levels off, i.e., the slope of the θ - σ_b relation becomes small for small water contents. When a linear relation is fitted to the non-linear θ - σ_b relation in the range of higher water contents, the intercept, b , of this linear fit is positive and the linear regression relation will underestimate the water contents when it is extrapolated to the drier range of soil moisture contents.

One characteristic of Fig. 5.8 is the conspicuous shift between the Eg and Bt-horizon: The range of $\sigma_{b,f}^{ERT}$ values rises by nearly one order of magnitude. This boundary is also reflected in the fitted slope, a , which decreases considerably below the Eg-horizon.

Tab. 5.4: Parameters, a and b , of a linear petrophysical relationship and related correlation coefficients, r_c , between θ_f^{ERT} and θ_f^{TDR} taken during the calibration period.

depth [cm]	0 – 20	20 – 65	65 – 120	120 – 160	> 160
horizon	A	Eg	Bt	Bg	Br
Error model dependent on electrode configuration (CEM)					
$a [m S^{-1}]$	34.75	47.72	8.34	2.71	2.09
$b [-]$	0.16	0.17	0.13	0.24	0.26
$r_c [-]$	0.92	0.81	0.91	0.69	0.97
Error model dependent on resistance (REM)					
$a [m S^{-1}]$	39.49	54.50	5.53	2.74	0.73
$b [-]$	0.19	0.19	0.22	0.25	0.35
$r_c [-]$	0.87	0.81	0.94	0.80	0.63

b) Error Model Dependent on Resistance (REM)

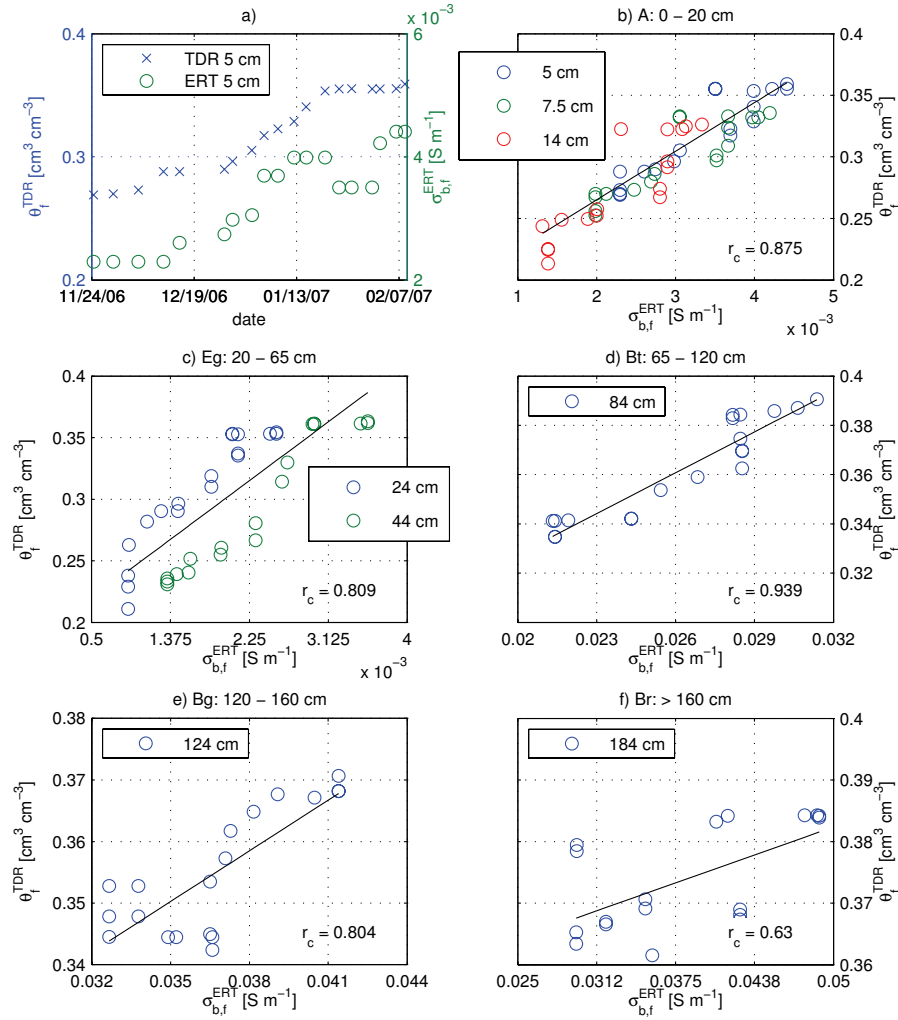


Fig. 5.9: Calibration of the REM model.

a) Exemplary Course of θ_f^{TDR} and $\sigma_{b,f}^{ERT}$ for the calibration period in 5 cm depth.

b)–f) Petrophysical relationship obtained from θ_f^{TDR} and $\sigma_{b,f}^{ERT}$ for different horizons.

Data based on the REM model (Fig. 5.9) look similar to that obtained from the CEM model (Fig. 5.8). Even the parameterizations of the derived petrophysical relationship agree well (Tab. 5.4). However, differences occur in the lowest horizons: For the Bg-Horizon (Fig. 5.8e; Fig. 5.9e), the data based on REM exhibit a reduced spread whereas for the Br-Horizon (Fig. 5.8f; Fig. 5.9f), data inverted with CEM show a stronger linear relationship. A larger spread around the fitting line within the Bg-horizon is probably induced by the TDR measurements: This horizon is characterized by mottling caused by metal concretions which obviously influence the accurate detection of the end of the TDR probe in the TDR waveform (see also Fig. 4.1, 124 cm depth). Therefore, water contents obtained by TDR are partly contaminated by errors in this horizon. Generally, the mean of correlation coefficients, r_c , of the CEM model is slightly higher.

5.4.3 Application of Field-Scale Petrophysical Relationship

5.4.3.1 Comparison with TDR

The previously derived petrophysical relationship was applied to ERT data of the plane $y=6$ m (Fig. 2.3), results are presented in Fig. 5.10. From a comparison between θ_f^{ERT} and θ_f^{TDR} it is obvious that seasonal dynamics are generally described well by ERT for all depths and for both error models. Dry spells during end of July and beginning of November 2006 are reproduced just as well as wetting phases during end of August 2006 and end of March 2007. Starting with the ERT derived water contents obtained from the CEM model, it is evident that the course runs not only in parallel with the TDR values but it also describe absolute water contents precisely. An exception is the depth of 84 cm where discrepancies between TDR and ERT are more pronounced. Furthermore, higher water contents at the beginning of the investigated period and the following decrease in soil moisture could not be captured accurately in depths of 44 cm and 124 cm, respectively. Deviations of θ_f^{ERT} from θ_f^{TDR} within the calibration period (green dashed lines, Fig. 5.10) are small and can be related to spatial variability in σ_b between the calibration planes ($y=0$; $y=10$ m) and the validation plane ($y=6$ m), which was captured by ERT. It should be noted that TDR trenches are located at the outer area of the field plot whereas the plane for the underlying validation is placed at its center.

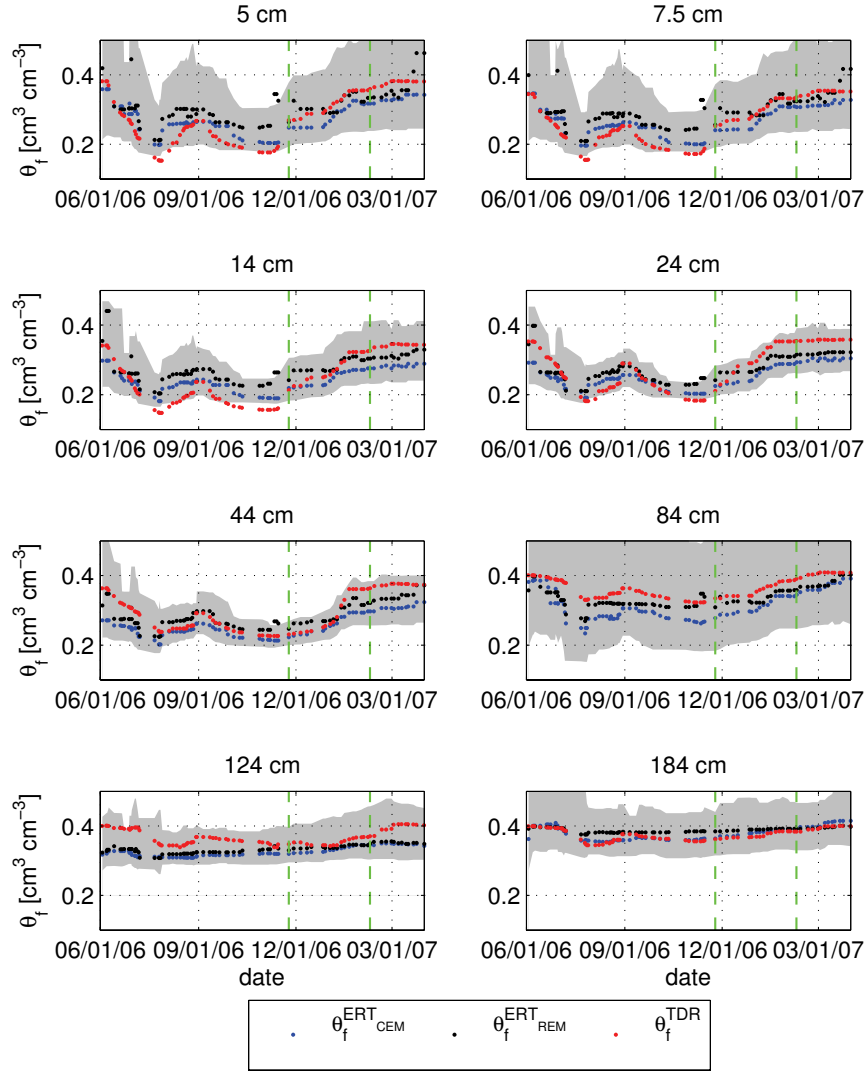


Fig. 5.10: Median of filtered water content from ERT with CEM, $\theta_f^{\text{ERT}_{\text{CEM}}}$, compared with median of filtered water content from ERT with REM, $\theta_f^{\text{ERT}_{\text{REM}}}$.

Furthermore, median of filtered water content from TDR, θ_f^{TDR} , is shown.

Shaded area represents difference between 5th and 95th percentiles of all ERT derived water contents obtained from the CEM model at the related depth. Green lines assign the calibration period of the petrophysical relationship.

However, mean water contents derived from TDR are enclosed by the range within the 5th and 95th percentiles at almost all depths for the entire period of investigation. The 5th percentile is slightly undercut in depths between 5 cm and 24 cm. Except for depths 5 cm, 7.5 cm, and 84 cm the range spanned by the percentiles is rather narrow, indicating a small spatial heterogeneity in horizontal direction. Depth 84 cm is located within the Bt-horizon, showing that here the variability is much higher in lateral direction.

The median of CEM based θ_f^{ERT} is at some depths not centered between the 5th and 95th percentile of the local water contents in one depth but is nearer to the 5th percentile. This is caused by the positive skewness of the frequency distribution of θ_f^{ERT} , indicating that there are few locations for which high water contents were derived. This might occur either due to real spatial variability of water contents in a soil horizon caused by heterogeneous water flow or due to artifacts that result from applying the same petrophysical relation to all locations in a soil horizon.

The agreement between REM based ERT and TDR water contents is also satisfying. However, the course of REM based ERT water contents is more noisy and characterized by a few outliers, which are particularly present in the uppermost depths (i.e., 5–24 cm). Those outliers were even not eliminated by the median filter.

Tab. 5.5: Correlation coefficient, r_v , between θ_f^{ERT} and θ_f^{TDR} taken during the validation period and normalized root mean square error, $RMSE$, for each depth.

depth [cm]	5	7.5	14	24	44	84	124	184
horizon	A			Eg		Bt	Bg	Br
Error model dependent on electrode configuration (CEM)								
r_v [–]	0.91	0.92	0.95	0.94	0.92	0.91	0.50	0.83
$CV(RMSE)$ [–]	0.13	0.11	0.16	0.15	0.16	0.15	0.13	0.03
Error model dependent on resistance (REM)								
r_v [–]	0.67	0.67	0.80	0.84	0.88	0.79	0.46	0.83
$CV(RMSE)$ [–]	0.27	0.26	0.21	0.13	0.10	0.09	0.11	0.05

To analyze the relationship between θ_f^{ERT} obtained from both error models and θ_f^{TDR} more quantitatively, correlation plots are given in Fig. 5.11 and Fig. 5.12, respectively. Related statistical parameters are listed in Tab. 5.5.

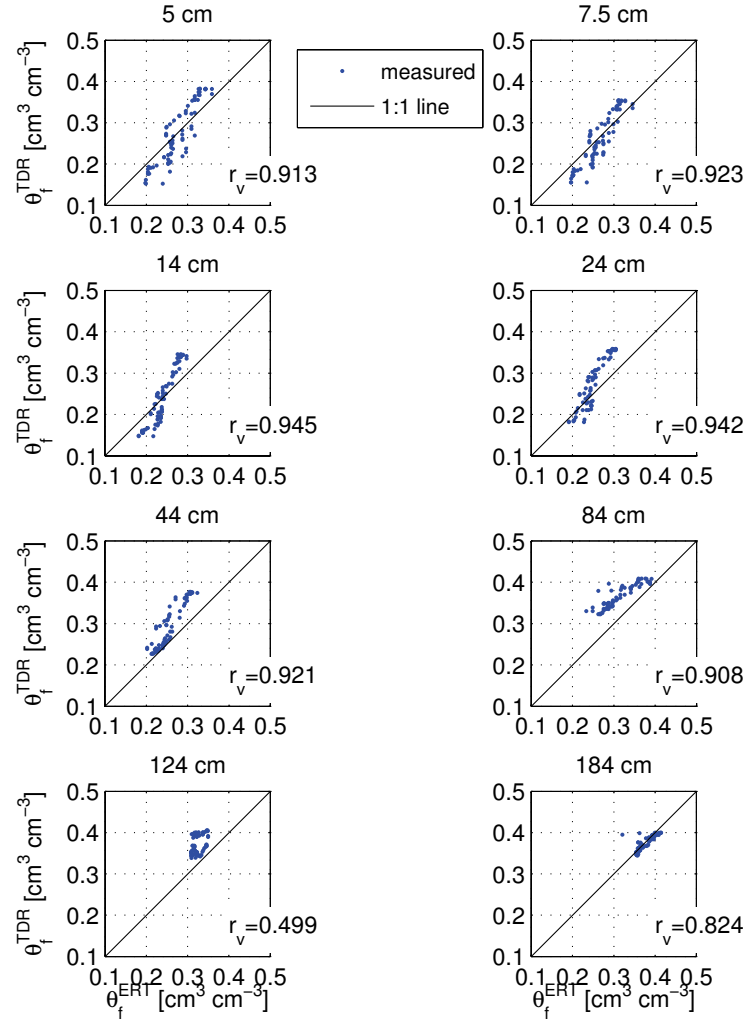


Fig. 5.11: Plots of θ_f^{TDR} versus θ_f^{ERT} obtained from inversions with CEM model at different depths in the soil profile.

r_v is the correlation coefficient and the lines represent 1:1 lines.

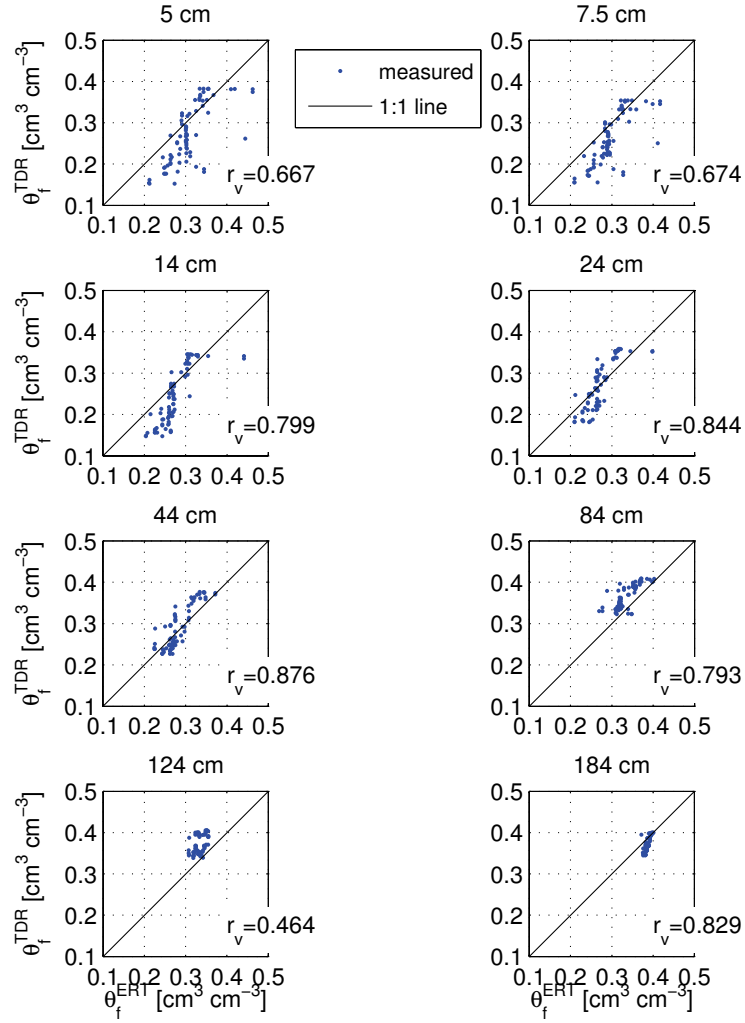


Fig. 5.12: Plots of θ_f^{TDR} versus θ_f^{ERT} obtained from inversions with REM model at different depths in the soil profile.

r_v is the correlation coefficient and the lines represent 1:1 lines.

The results obtained from the CEM model generally lead to higher r_v for all depths (except for depth 184 cm where r_v is equal, Tab. 5.5). This means that the linear relation between θ_f^{ERT} and θ_f^{TDR} is more pronounced when the CEM model is applied. Obviously, the REM sometimes fails to represent the soil water dynamics precisely, which can be seen in 84 cm depth where θ_f^{ERT} based on the REM model reach a plateau level during summer 2006 (Fig. 5.10). Another reason are the already mentioned outliers which attract attention in Fig. 5.12 in depths 5–14 cm, leading to lower r_v compared to the results derived from the CEM model. For both error models the correlation is weaker between θ_f^{ERT} and θ_f^{TDR} in a depth of 124 cm. As already mentioned, this is probably caused by erroneous TDR measurements.

The correlation coefficient quantifies the goodness of fit of a linear relation between θ_f^{ERT} and θ_f^{TDR} . However, the correlation coefficient does not quantify the systematic deviation of the relation between θ_f^{ERT} and θ_f^{TDR} from the 1:1 line. The correlation coefficient therefore does not quantify a systematic bias between θ_f^{ERT} and θ_f^{TDR} . The normalized $RMSE$, $CV(RMSE)$, is a valuable measure that also quantifies the systematic bias between θ_f^{ERT} and θ_f^{TDR} (Eq. [5.3]). $CV(RMSE)$ derived from the CEM model is considerably lower than from the REM model for the uppermost depths (5–14 cm, Tab. 5.5). On the one hand, this is caused again by outliers (5 and 7.5 cm depth). On the other hand, the general level of θ_f^{TDR} is overestimated by the values obtained from the REM model. Beneath a depth of 24 cm $CV(RMSE)$ is somewhat lower for the REM model compared to data achieved from the CEM model.

Therefore, it can be concluded that there are differences in quality of both models: The most apparent one is the presence of several outliers in θ_f^{ERT} based on the REM model. However, the bias between θ_f^{ERT} and θ_f^{TDR} is smaller compared to the CEM model in lower depths. But in general, the course of θ_f^{ERT} obtained from the CEM model is more accurate, taking into account the high correlation with θ_f^{TDR} and the robustness with respect to outliers. Furthermore, the bias between θ_f^{ERT} and θ_f^{TDR} rather reflects an inaccurate calibration relation, which can be corrected for using a recalibration, than an erroneous ERT inversion. Hence, the inversion with the CEM model is particularly the appropriate choice if relative changes in water contents should be considered accurately at the near-surface.

Although the synthetic experiments conducted in chapter 4 definitely suggested choosing the CEM model, the difference between both error models was not so clearly observed in the filtered time series of θ_f^{ERT} . The reason for the smaller effect of the choice of the error

model on the inverted θ_f^{ERT} is twofold: first, a relative error of 0.126 was used in the synthetic experiment whereas the data of the time window used for the current study had a smaller relative error of 0.04 to 0.07 (Tab. 5.3). Second, median filtered (both in space and time) inversion results were used which led to an additional reduction in the noise. Nevertheless, despite lower error level and the data filtering, the inversion results obtained from the REM model were still prone to considerably more noise and larger outliers than inversion results obtained from the CEM model.

The inversions of the following subsections were performed with the CEM model to obtain accurate relative changes in water content, particularly close to the surface.

5.4.3.2 Generation of a Water Balance

Fig. 5.13 shows a plot of PET and H calculated for the period between June 13, 2006 and March 30, 2007. H drawn from θ_f^{ERT} is denoted as H^{ERT} and H from θ_f^{TDR} as H^{TDR} . For comparison, the development of the depth to groundwater table, GWL , is shown.

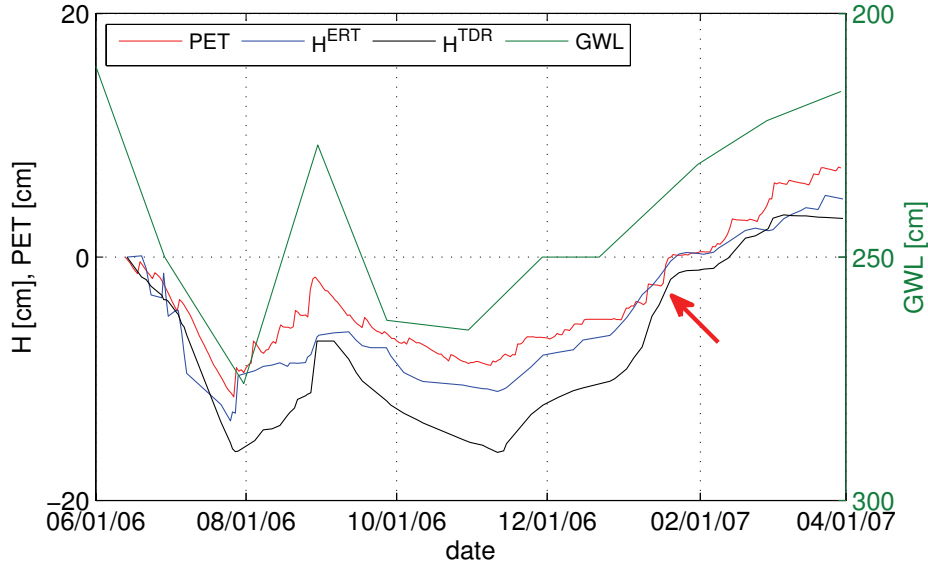


Fig. 5.13: Cumulative height of supplied water at the upper bound, PET , and cumulative change in height of water in the soil, H , drawn from both ERT (H^{ERT}) and TDR (H^{TDR}).

GWL is the depth to groundwater table. Red arrow denotes hurricane “Kyrill”, passing Germany at January 18, 2007.

Starting with the comparison between H^{ERT} and H^{TDR} , it is evident that not only the course is very similar but also absolute values are consistent. However, in August 2006 and in October 2006 to January 2007 curves deviate from each other where TDR measurements exhibit smaller values than ERT based values. This is caused by the oftentimes larger range of occurring θ_f^{TDR} compared to θ_f^{ERT} (Fig. 5.11). Hence, differences in θ_f^{TDR} are even stronger reflected in cumulative changes of water content, H^{TDR} , as they are in H^{ERT} . Apart from that, all hydrological events are well reproduced by both techniques although the course of H^{TDR} seems to be somewhat smoother.

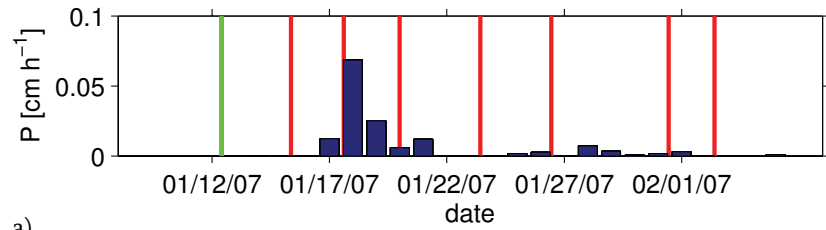
Comparing soil water storage, H , with the precipitation surplus PET , the assumption that both quantities are strongly correlated is supported. Additionally, both are clearly related to the depth to groundwater table, GWL . Dry periods during end of July 2006 and beginning of November 2006 are reproduced as well as the wetting period during August 2006. On the other hand, between July 2006 and January 2007 the soil water reduction is greater than the amount of water which is lost by evapotranspiration. This means that

during summer and autumn 2006 there must have been occurred deep percolation, leading to a stored soil water, H , that was smaller than PET . However, this is not supported by the decreasing depth to groundwater table, GWL , in August 2006. Finally, soil moisture storage rises more rapidly at the beginning of January 2007 so that both H and PET run congruently again. This suggests that during this period, water would flow into the soil profile through the bottom boundary of the profile. This corresponds with the rise of the water table during this period. At the end of January 2007, the soil water storage is again equal to the storage at the beginning of the observation period (June 13, 2006). As a consequence, the water balance suggests that water drains out the soil profile during the summer period whereas an inflow is derived for the winter period. This seems opposite to what would be expected, namely that most drainage or leaching out of the soil profile occurs during the winter period. It must however be noted that the precipitation surplus during the entire monitoring period was small (60 mm) and that this surplus went along with an increase in water storage so that the amount of drainage or groundwater recharge was even smaller (about 30–40 mm). This amount underestimates the rate which was calculated by Bogen et al. (2005) who computed a recharge of 100–150 mm/a for this area on a basis of 21 years. This cannot be explained by a lower precipitation since the sum of free precipitation amounted 624 mm in the given period of ten months which was close to the yearly average precipitation which is 698 mm (source: meteorological station, Forschungszentrum Jülich). However, it has to be considered that groundwater recharge rates under forests can be locally very low. The derived drainage and inflow during the summer/ autumn and winter periods, respectively, are consequently also small.

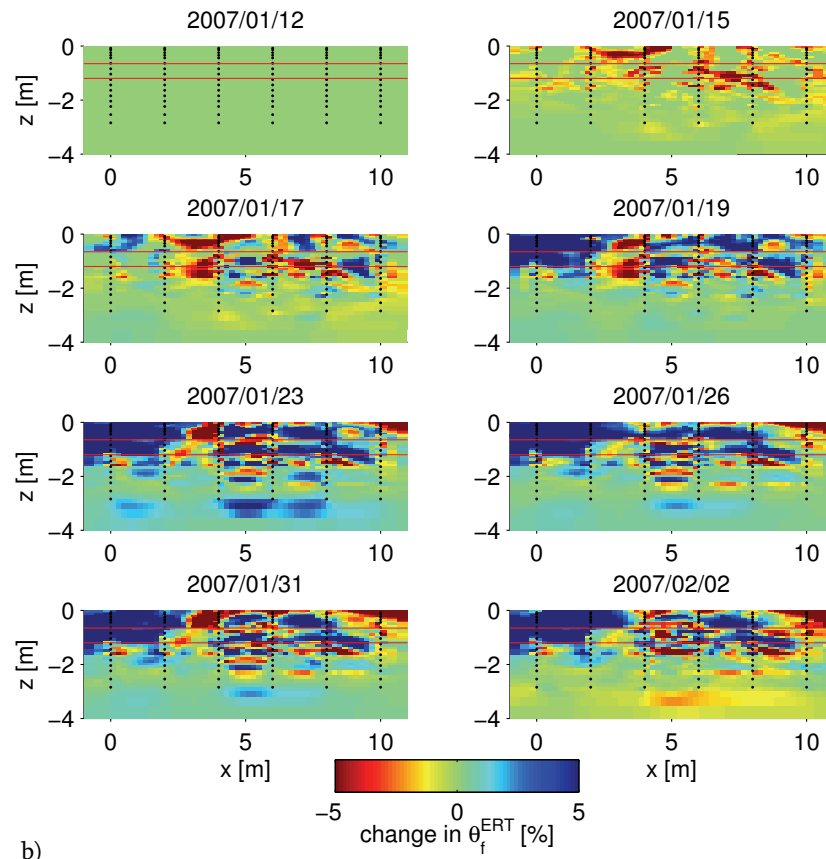
5.4.3.3 Monitoring of Spatiotemporal Soil Water Content Changes

Observation of Soil Water Content Changes due to a Single Rainfall Event

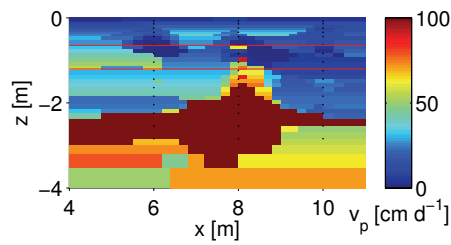
Ten ERT data sets have been taken before and after the passage of a rainstorm. The hydrograph of precipitation throughfall during the investigated period is illustrated in Fig. 5.14a. Dates of ERT measurements are marked by bars. There were ten data sets required to produce eight filtered distributions of water content if a median filter of order $\mu = 2$ was applied (last two measurements are not shown here). Changes in filtered water contents derived from ERT were calculated with respect to the background distribution on January 12, 2007 (Fig. 5.14b).



a)



b)



c)



Fig. 5.14: a) Throughfall during the investigated period. b) Change in filtered water content derived from ERT for plane $y=6$ m. c) Peak velocities, v_p , derived from a tracer experiment (chapter 6).

It should be noted that the tracer experiment was performed only on a part of the field plot.

First of all, it is obvious that the rain event occurring at January 18 is detected by the ERT measurements since there is the most evident change in water contents. Also the drying process until the beginning of February is well described. Generally, the roughness of all distributions is quite high which is caused by the petrophysical relation. Small changes in bulk electrical conductivity are mapped into large changes in water content due to high slopes, a (Tab. 5.4). However, several phenomena are clearly indicated by ERT based water contents: Obviously, there are regions which still dry out even after the main event at January 18 (e.g., region between 2nd and 3rd borehole, considered from left). On the other hand, there are locations which remain wetted all over the time (e.g., region between 1st and 2nd borehole). This shows not only the consistency of the different data sets but also the heterogeneity of the soil. Furthermore, there are signs of preferential flow, indicated by patches (lower end of boreholes 3 to 5) where water suddenly flows in at January 23 and disappears afterwards. Those regions are in close vicinity to locations which were characterized by a very fast breakthrough, i.e., high peak velocities, v_p , when a tracer experiment was performed (analyzed in chapter 6). For comparison, a distribution of v_p is given in Fig. 5.14c. Furthermore, this figure indicates a small belt of higher v_p in 0.5 m depth, located between $x=6$ m and $x=9$ m which is also reflected by a rapid rise in water content from January 17 to January 19, 2007. This layer is interrupted by a sharp-cut boundary at about 0.7 m depth. This depth is located at the top of the Bt-horizon which will also be identified as initiator of preferential flow processes in the next chapter (highlighted by red lines in Fig. 5.14b and c). That conclusion is supported by the horizontal extension of low water contents in about 0.7 m depth which remains dry even after the main rain event at January 18, 2007 (Fig. 5.14b). Additionally, higher v_p (Fig. 5.14c) as well as rapid rise in water content (Fig. 5.14b) are found consistently within the Bt-horizon due to preferential flow.

To evaluate the reliability of ERT and TDR measurements supplementary, a water balance was established for the period of the passage of the storm. Results are shown in Fig. 5.15.

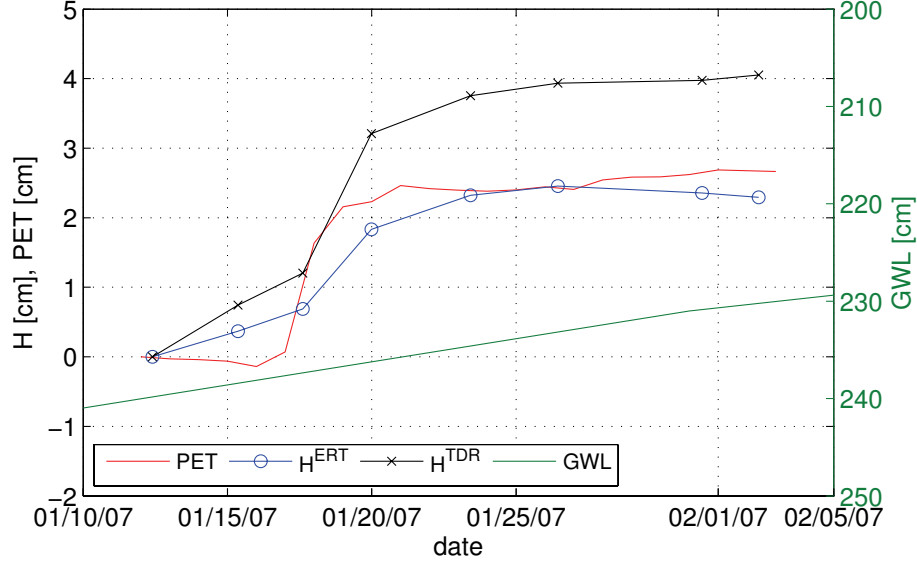
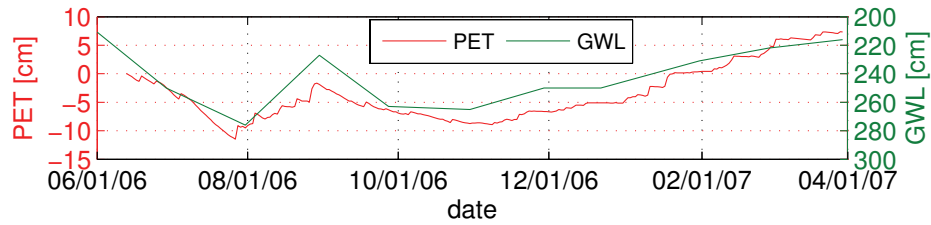


Fig. 5.15: Water balance during the passage of the rainstorm.

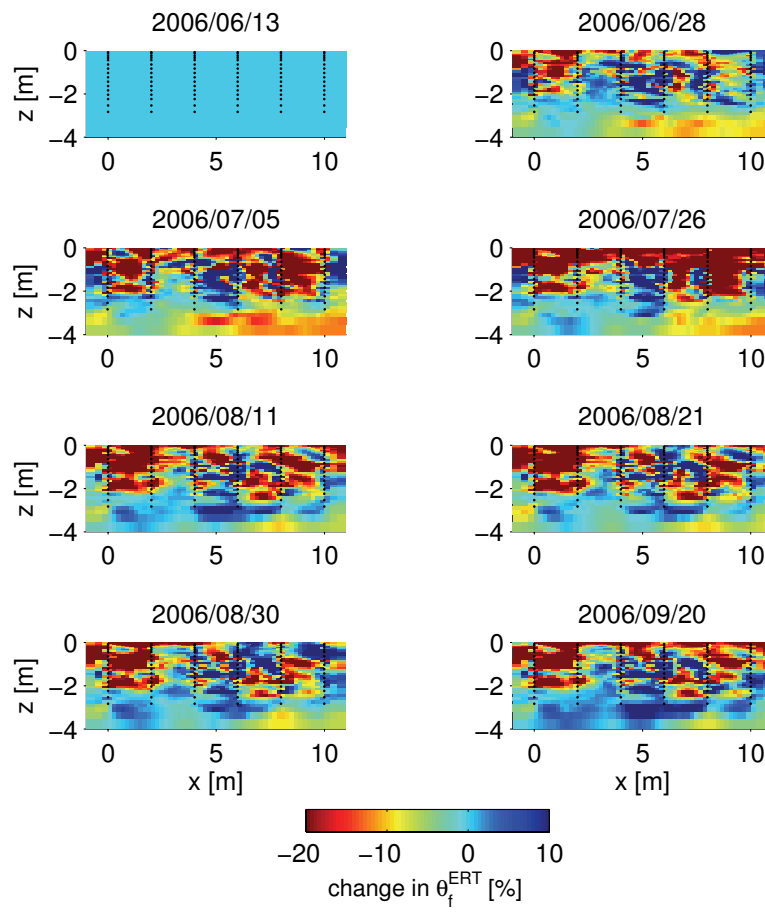
Cumulative height of supplied water at the upper bound, PET , and cumulative change in height of water in the soil, H , drawn from both ERT (H^{ERT}) and TDR (H^{TDR}). GWL is the depth to groundwater table.

It is obvious that H^{TDR} increased more than PET until January 25, leading to the assumption that there must have been an additional supply of water. This corresponds to the decreasing depth to groundwater table, GWL , during January 2007. However, H^{ERT} does not capture that additional amount of water storage. This is also reflected in the main rain event at January 18 which is described smoother by the ERT measurements. Furthermore, little rain events after January 25 cannot be recovered correctly. This is caused by the application of the median filter, which extinguishes not only outliers but also extreme values. However, ERT in combination with an appropriate filter technique turns out to be valuable to establish a water balance in a short term period with exceptional weather conditions.

Observation of Seasonal Soil Water Content Changes



a)



b)

Fig. 5.16: a) Cumulative height of supplied water at the upper bound, PET , and depth to groundwater table, GWL , taken over from Fig. 5.13. b) Soil water content changes in the period between June 2006 and September 2006 for plane $y=6$ m with respect to a background taken at 2006/06/13.

Fig. 5.16 and Fig. 5.17 show changes in soil water content during the period investigated in chapter 5.4.3.2 with respect to the background distribution taken at 2006/06/13 for plane $y=6$ m. From comparison with hydrological boundary conditions presented in Fig. 5.16a it is evident that all of the most prominent changes are captured by the water content distributions derived from ERT. In addition to Fig. 5.13, not only the temporal, but also the spatial variability of soil water contents is obvious. The top soil dries out continuously until end of July (2006/07/26, Fig. 5.16b), corresponding with the maximal evapotranspiration, reflected in PET . There are two spots of soil water reduction recognizable that extend to a depth of 2 m: The first one is located between $x=0$ to $x=2$ m, the second one between $x=6$ m and $x=10$ m. Those locations are obviously related to the positions of two trees ($x=-2.5$ m and $x=8.6$ m, respectively, Fig. 2.3) and demonstrate their root water uptake during the dry spell in summer 2006. Although the northern tree is positioned beyond the field plot ($x=-2.5$ m), its root system is assumed to influence the soil water distribution in the inner part of the field plot due to the tall habitus of the tree. After this dry spell the water content within the top soil obviously rises during August 2006. Those locations where tree roots predominate remain still dry during precipitation events in beginning of August. On the other hand, there are again indications of preferential flow given: Locations between $x=4$ m and $x=8$ m show higher water contents in a depth of 3 m than the surrounding area (Fig. 5.16b, 2006/08/11). Those spots coincide exactly with those which were assumed to be connected to preferential flow paths during the passage of a windstorm with considerable rain events (Fig. 5.14b, 2007/01/23). Additionally, those positions were characterized by high peak velocities, v_p , in a tracer experiment (analyzed in chapter 6, also depicted in Fig. 5.14c), supporting the assumption that preferential flow is the reason for rapidly rising water contents at these locations. Finally, decreasing depths to groundwater table, GWL , during August 2006 (Fig. 5.16a) are reproduced well by higher water contents in lower depths (i.e., below 2.5 m, Fig. 5.16b).

In October to November 2006 the depth to groundwater table reaches a further maximum, reflected in a desaturation in depths below 2.5 m (Fig. 5.17). Also the net water supply, i.e., PET , decreases during this period, which is supported by decreasing soil water contents within the topmost two meters of the soil. In contrast to the dry spell in summer 2006 (2006/07/26, Fig. 5.16b), the location between $x=6$ m and $x=8$ m (i.e., below a tree) dries less out in a depth of about 2 m. This indicates that long-term soil water monitoring using ERT is capable to map tree root systems. Therefore, it is possible to separate soil water dynamics caused by soil heterogeneity (dominating water fluxes in winter) from dynamics caused by the heterogeneity of the root system (dominating water fluxes in summer).

In the beginning of 2007, *GWL* is decreasing continuously, attended by several rain events. The most apparent precipitation event at 2007/01/18 was analyzed in the previous chapter. Those conditions are represented by a continuous increase in soil water contents, reaching its maximum in 2007/03/30 (Fig. 5.17).

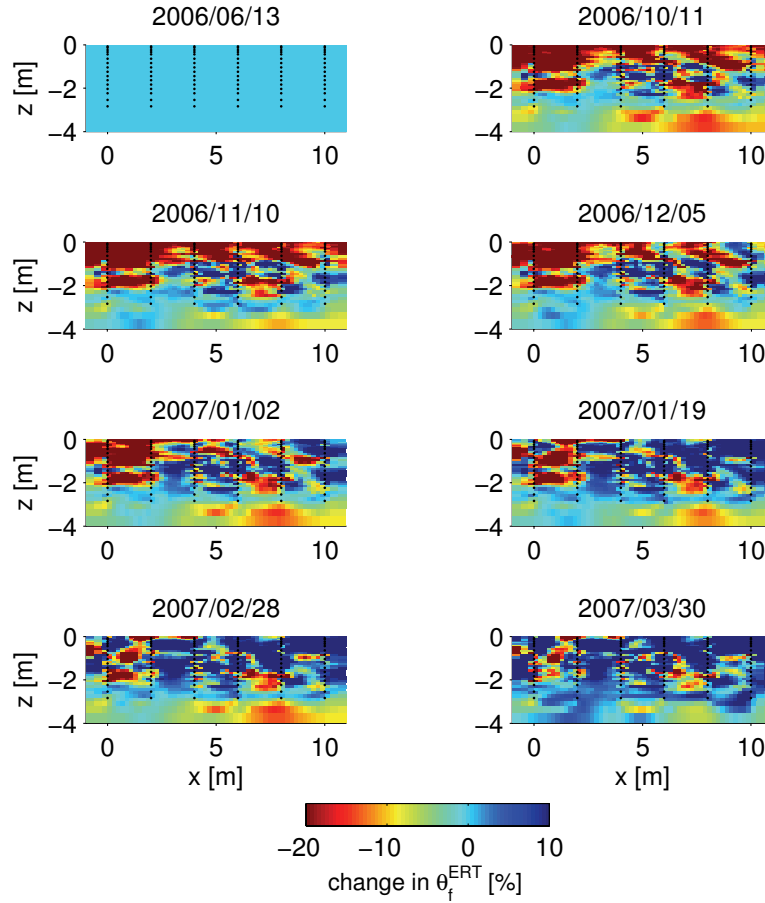


Fig. 5.17: Soil water content changes in the period between October 2006 and March 2007 for plane $y=6$ m with respect to a background taken at 2006/06/13.

5.5 Conclusions

Soil water content was monitored in several ERT sections in a forest stand during a nine months period, namely from the beginning of June 2006 until the end of March 2007. The two outer sections were used to calibrate the petrophysical relationship in order to derive water contents from ERT measurements. It turned out that a linear petrophysical model was sufficient to relate water contents to bulk soil electrical conductivity. Afterwards, a section located at the center of the field plot was used to validate previously derived relationships. For the geoelectrical inversion two different error models were used: one model that relates the error level to the measured resistance, REM, and one model that relates the error model to the electrode configuration, CEM. The mean ERT derived water content at a certain depth was recorded over time and plotted together with the average water contents obtained from TDR probes at the same depth. A median filter was used to reduce the noise of the time series of TDR and ERT measured moisture contents. The course of resulting water contents obtained for both error models was in high agreement with the TDR values. The CEM model seemed to describe the error level of the ERT measurements better than the REM model so that the correlation between ERT and TDR derived water contents was considerably larger for the CEM than for the REM model. Hence, the suitability of ERT to monitor soil water dynamics was further validated by means of the CEM model. Despite the use of a median filter which effectively reduced the noise level, short-term changes in water content resulting from extreme weather conditions could still be detected. A water balance was established where precipitation and evapotranspiration were opposed to changes in soil water storage measured by ERT and TDR. Here, ERT and TDR data were correlated well but evapotranspiration derived from eddy covariance method deviated during summer and autumn. But due to the fact that the agreement of ERT and TDR data was very good, ERT is assumed to be appropriate to estimate soil water balances. An underestimation of the sum of applied water as reported by other authors (Deiana et al., 2008) could not be observed. Finally, a heavy rainfall event in January 2007 was investigated by means of a 2D ERT section. Although a pixel wise median filter over time was applied, the rapid increase in soil water contents could still be detected. Furthermore, regions characterized by different soil water contents were observed to be consistent in time, pointing out the heterogeneity the water flow in the soil. Additionally, rapid transport into the subsoil indicated preferential flow. The

reliability of ERT measurements could be confirmed by the establishment of a water balance during and after the rainstorm although the real soil water storage was slightly underestimated. Furthermore, a long-term observation of soil water contents measured by ERT revealed locations of lower moisture during dry spells which could be assigned to tree roots.

Summing up, ERT turned out to be an appropriate means to observe soil water dynamics as well as tree root activity. Although the temporal variability in electrical resistivity was originally very large due to data noise, seasonal changes as well as spatial patterns of soil water contents could be described accurately when a simple median filter was applied. However, more elegant regularization techniques (e.g., time regularization or joint inversion) are required to smooth the final distribution of soil water contents.

6 Investigating Preferential Flow Processes in a Forest Soil Using Time Domain Reflectometry and Electrical Resistivity Tomography

6.1 Abstract

A comparison was made between the well-established time-domain reflectometry (TDR) method and electrical resistivity tomography (ERT) to monitor bulk electrical conductivity, σ_b , during a saline tracer experiment. The experiment was conducted at a forest site on the premises of the Forschungszentrum Jülich. To parameterize solute transport processes, the convection-dispersion equation (CDE) and the mobile-immobile model (MIM) were fitted to the data. Although σ_b derived from ERT was lower than TDR measurements in almost all depths, estimated pore water velocities of the CDE model were very similar. Early peak arrival times at lower depths and long tailings of the breakthrough curves (BTC) clearly indicated preferential flow phenomena which could not be described with an appropriate parameterization using classical transport approaches such as the CDE. Also the adaption of the MIM model did not lead to more reasonable solute transport parameters. Additionally, preferential flow was reflected in high peak velocities in the lower depths which exceeded piston flow velocities. The strong decline in peak σ_b with depth showed that the volume through which transport takes place decreased with depth. Typical features of preferential transport could be detected and the spatial variability of the preferential transport process could be imaged by ERT.

6.2 Introduction

Characterization of flow and transport processes in soils relies on measurements that capture relevant processes. Preferential flow and transport or rapid transport through a part of the soil volume is an example of a process that is difficult to observe with measurement techniques that sample the soil solution in situ. Using local observation methods such as suction samplers or TDR probes, only a part of the total soil volume is sampled and the representativeness of the observed transport may be limited. The problem of representativeness of the observed local concentrations is even more prominent when large water and solute fluxes occur through only a small part of the soil volume.

Bulk electrical conductivity, σ_b , is a proxy of salt tracer concentrations that can be monitored non-invasively using techniques like TDR (time-domain reflectometry) and ERT (electrical resistivity tomography). These techniques may, therefore, be used to track the movement of saline tracers. Since the sampling volume of TDR is limited to a certain soil volume around the rods of the TDR probes, TDR measurements represent rather local measurements (Ferre et al., 1998; Nissen et al., 2003). In contrast, resistances that are measured in an ERT survey integrate the electrical conductivity of the subsurface over a larger soil volume. By inverting a data set of resistance measurements, a map or 3-D distribution of the bulk electrical conductivity in a larger image plane or soil volume is obtained. However, the inversion process may have an important impact on the spatial resolution and the contrast or variability in the obtained electrical conductivity distribution (LaBrecque et al., 1996; Kemna et al., 2002; Day-Lewis et al., 2005).

In several studies TDR was used to monitor solute transport processes in soils on the laboratory scale (Vanclooster et al., 1993; Mallants et al., 1994; Ward et al., 1994; Risler et al., 1996; Vanderborght et al., 1996; Vogeler et al., 1997), the lysimeter scale (Vanclooster et al., 1995; Vanderborght et al., 1997; Vanderborght et al., 2000; Javaux and Vanclooster, 2003), and the field scale (Kachanoski et al., 1992; Kachanoski et al., 1994; Jacques et al., 1998; Noborio et al., 2006). Meanwhile, a number of studies reported on the application of ERT to monitor tracer experiments. They can also be summarized in terms of the scale on which they were carried out: Binley et al. (1996) and Olsen et al. (1999) derived tomographic images from ERT to analyze solute transport in undisturbed soil columns. On

the next larger scale, Köstel et al. (2008) recently monitored the movement of a calcium chloride tracer applied to an undisturbed soil monolith by means of ERT and TDR. Slater et al. (2000) and Slater et al. (2002) performed tracer experiments in large experimental tanks. On the field plot scale, Deiana et al. (2008) carried out a freshwater infiltration experiment using ERT and ground penetrating radar (GPR) and Looms et al. (2008) estimated solute transport parameters by monitoring a tracer plume. On the field scale, quantitative analysis of a tracer experiment was performed by Kemna et al. (2002). Most of the cited studies focussed on the deeper subsurface or sites with a rather coarse soil or sediment texture. In such soils or aquifers, flow heterogeneity is manifested on a relatively large scale, which can be resolved by ERT. In finer textured soils and closer to the soil surface, preferential flow and transport occurs through large inter-aggregate pores, cracks and biopores (Feyen et al., 1998). Therefore, we investigated in this study whether ERT could be used to image preferential flow processes in a forest soil with a fine texture. Imaging preferential flow and transport on the pore scale is however beyond the spatial resolution of field-scale ERT applications. However, the effect of the rapid saline tracer intrusion in the large inter-aggregate pores or macropores may be observed in the bulk electrical conductivity. Mass transfer processes were investigated by Singha et al. (2007) when they injected freshwater into a confined, brackish aquifer. They obtained a nonlinear, hysteretic relationship between fluid electrical conductivity, σ_w , and σ_b , which they interpreted as indication of mass transfer limitations between the mobile and immobile fractions of the pore water. Therefore, ERT might be used to monitor preferential transport and image its spatial variation. To describe preferential flow processes mathematically, van Genuchten and Wierenga (1976) proposed a mobile-immobile model (MIM) in which the pore water is divided into a mobile and an immobile fraction, respectively. Advective flow is assumed to occur only in the mobile pore region, whereas exchange between both regions is allowed by molecular diffusion. This concept has been the basis for the interpretation of many transport experiments conducted in soils. A detailed overview of model applications for structured soils is given by Köhne et al. (2009).

In this study, we investigate whether preferential flow that was induced during a tracer experiment in a fine textured forest soil can be monitored and imaged using ERT. First, σ_b values and transport model parameters that were derived from breakthrough curves obtained with ERT and TDR were compared. On the lysimeter scale, Köstel et al. (2008) already featured TDR to be a valuable reference which measurements agreed very well with ERT inverted σ_b . But the soil they investigated showed a rather homogeneous transport on the larger scale characterized by a relatively small effective dispersivity and a pore water velocity which was close to the mean flow rate divided by the volumetric

water content. Therefore, a second topic of this work is to investigate whether ERT is capable of detecting and imaging more heterogeneous transport or more outspoken preferential flow and transport processes, which can be expected in a fine textured forest soil when a high infiltration rate is applied.

6.3 Materials and Methods

6.3.1 Experimental Setup

A field plot was equipped with 36 ERT boreholes for monitoring of natural changes in soil water content. For the tracer experiment, only a plot with twelve boreholes out of the entire setup was selected (Fig. 6.1). Each borehole consists of 16 stainless steel electrodes, distributed over a depth from 7.5 cm to 284 cm (Tab. 2.2). On the east side of the plot, additional soil physical measurements were taken in different depths: The vertical trench wall (related to trench 3, Fig. 6.1) was equipped with 8 horizontally installed TDR probes, 5 suction samplers, and 6 temperature probes (Tab. 2.2).

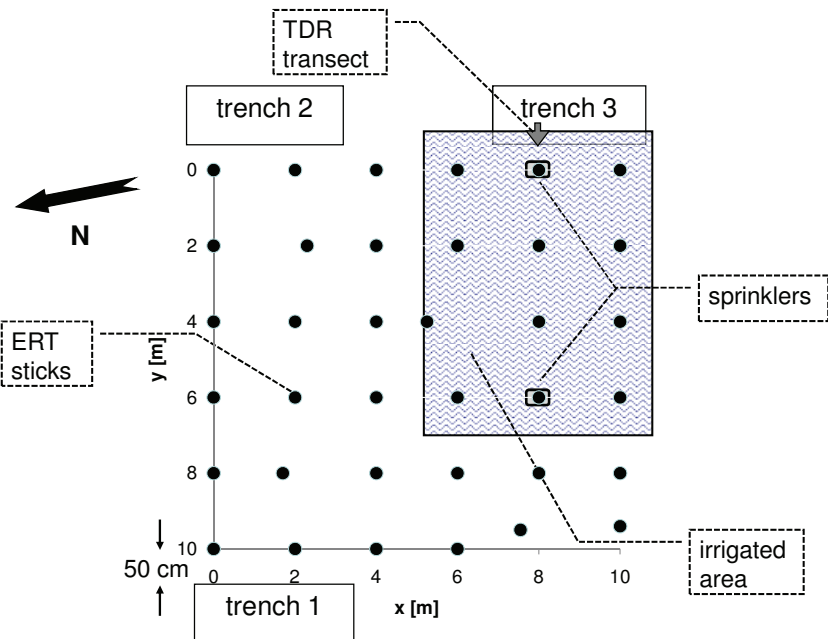


Fig. 6.1: Overview of field site with installed trenches, sprinklers, and irrigated area.

These soil physical data were recorded hourly, whereas ERT monitoring was restricted by the duration of one measurement cycle (i.e., 10 h 31 min) which led to two measurements per day. An eight channel apparatus “Resecs” (GeoServe GmbH, Kiel, Germany) was used for the geoelectrical measurements. Based on test measurements a dipole-dipole electrode configuration was used for ERT data acquisition. To obtain a strong signal in measured voltages (i.e., low geometric factors), the current was injected between two boreholes (i.e., 2 m apart). Due to internal restrictions of the device, the potential dipole had to be placed within one borehole (Fig. 6.2a).

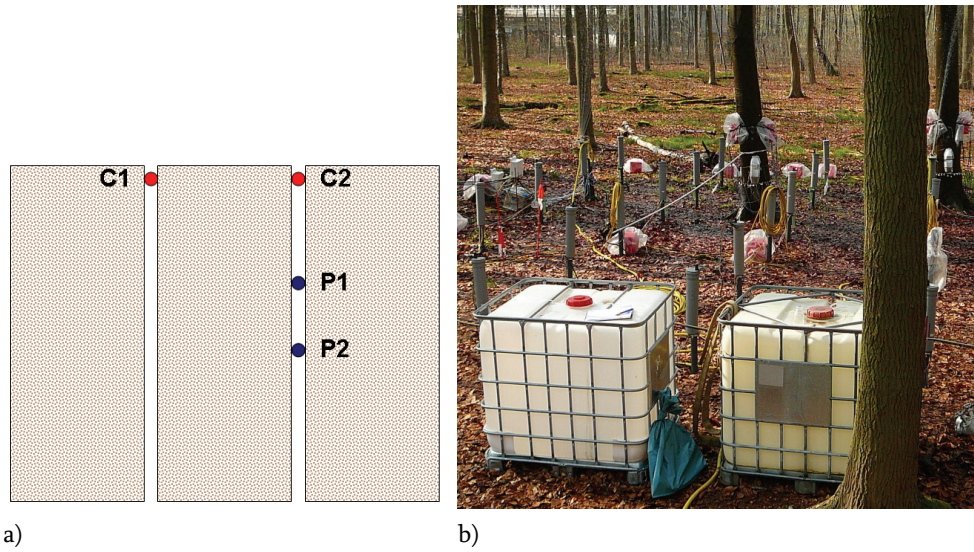


Fig. 6.2: a) Dipole-dipole configuration taken for the ERT measurements. C1, C2 denote current electrodes separated in two boreholes, and P1, P2 potential electrodes within one borehole. b) Experimental setup of the tracer experiment.

Two sprinklers were used for irrigation of an area of about 6 m x 8 m. Both sprinklers were located in the outer area of the irrigated site (Fig. 6.1). The sprinklers were supplied by a fire hydrant 200 meters away from the field site. The irrigation rate was controlled by an electromagnetic valve with a clock timer that opened the valve only 15 minutes per hour so that a mean irrigation rate of 9.6 cm d^{-1} was obtained. Two weeks before the tracer was applied, the irrigation with tap water was started to create a saturated soil profile with a homogeneous electrical conductivity of the pore water ($4.49 \cdot 10^{-2} \text{ S m}^{-1}$).

On April 15, 2007 at 5:45 p.m. the tracer application was initiated. The sprinklers were disconnected from the fire hydrant and connected by an electric pump to tanks (Fig. 6.2b) that were filled with a calcium chloride solution ($6.5 \cdot 10^{-3} \text{ g CaCl}_2 \text{ cm}^{-3}$, $9.87 \cdot 10^{-1} \text{ S m}^{-1}$) for 24 hours. The electric pump was adjusted to keep the same irrigation rate as before.

Afterwards, the tracer was leached by means of tap water irrigation for 40 days, again with an irrigation rate of $q_f = 9.6 \text{ cm d}^{-1}$. Fig. 6.3 shows the distribution of the irrigation rate that was measured in twelve rain gauges and which served as basis for the derivation of mean irrigation rates. The rain shadow in the lower right corner is caused by a tree trunk. Since trees were still not foliating at the time of the experiment, transpiration was assumed to be negligible.

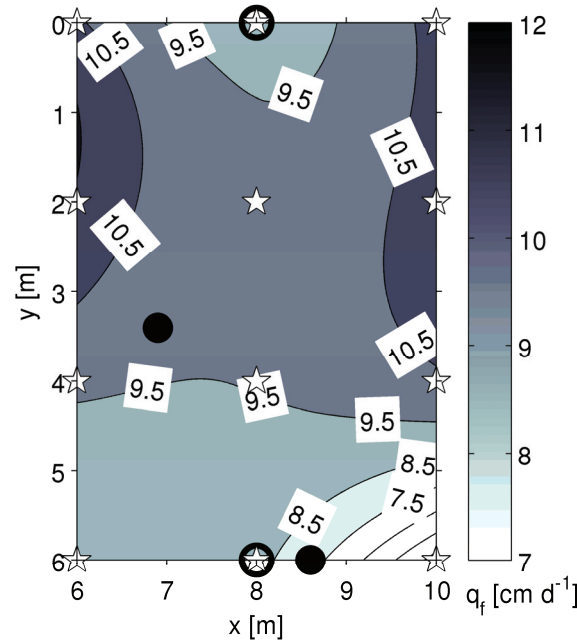


Fig. 6.3: Mean flux density, q_f , of tracer and tap water irrigation, respectively. Pentagrams denote rain gauges, open circles sprinklers, and closed circles trees.

6.3.2 Data Analysis

6.3.2.1 Derivation of Concentrations from Bulk Soil Electrical Conductivity Measurements

Both TDR and ERT result in bulk electrical conductivity values, σ_b , after post-processing. For constant soil water contents and σ_b values smaller than 5 S m^{-1} , a linear relation between σ_b and the salt tracer concentration, C_b , can be assumed (Ward et al., 1994):

$$C_b = \alpha_c \sigma_b + \beta_c \quad [6.1]$$

α_c and β_c are calibration constants. For the parameterization of solute transport models, also relative concentration changes can be used. If bulk electrical conductivities are linearly related to the salt tracer concentrations, this implies that transport model parameters can also be derived from relative changes in bulk electrical conductivity. Eq. [6.1] is valid for resident concentrations at time t , $C(t)$, for background concentration at time $t = 0$, C_0 , and for the tracer input concentration, C_{in} .

A relative concentration can be calculated which is independent on calibration parameters α_c and β_c :

$$\frac{C(t) - C_{in}}{C_0 - C_{in}} = \frac{\sigma_b(t) - \sigma_{b,in}}{\sigma_{b,0} - \sigma_{b,in}} \quad [6.2]$$

For a linear transport process, the relative concentration $[C(t) - C_{in}]/[C_0 - C_{in}]$ and relative bulk electrical conductivity are described by the same transport equation that is used for the absolute concentration C . When $\sigma_{b,0} - \sigma_{b,in}$ is unknown, it may be fitted from observed breakthrough curves. σ_b data (obtained from TDR or ERT) were standardized at a temperature of 25 °C according to Eq. [3.30].

6.3.2.2 Analysis of Solute Transport

Comparison Between ERT and TDR

First, a comparison was performed between ERT and TDR breakthrough curves (BTCs). Therefore, the “next neighbor pixel” to a respective TDR probe (8 in total) was taken out of a 2D distribution of background corrected ERT conductivities, $\sigma_b(t) - \sigma_{b,in}$. Here, plane $y=0$ (Fig. 6.1) was considered as reference, since boundary effects seemed to be too distinct when taking boundary elements out of plane $x=8$ m. First, BTCs derived from both TDR and ERT were compared in terms of peak arrival times, t_p . This information was used to derive peak velocities, $v_p = z/t_p$, where z is the observation depth. The peak velocity, v_p , was compared with the piston flow velocity,

$$v_q = \frac{q_f}{\theta}, \quad [6.3]$$

where q_f is the applied irrigation rate of 9.6 cm d^{-1} . The soil water content, $\bar{\theta}$, was derived as mean of all available TDR water contents from the top surface to the respective depth of interest. Piston flow velocity was calculated assuming that the water flux was homogeneous in the soil profile and that the entire water-filled pore space contributed to the transport process. When preferential flow occurs, local water fluxes can be considerably larger than the mean water flux and parts of the pore volume may be bypassed by rapid transport in preferential flow zones or macropores. This rapid transport corresponds with a considerable tracer breakthrough that is much earlier than expected when flow is uniform and flow takes place uniformly in the entire water filled pore volume. Hence, a peak velocity that is much larger than the piston flow velocity is an indicator of preferential flow.

To illustrate the spatial variability of the transport process and the resulting breakthrough curves (BTCs) of bulk soil electrical conductivities, TDR values were also compared with the mean and the 10th and 90th percentiles of all ERT derived σ_b BTCs calculated from all available inverted ERT planes (namely $x=6 \text{ m}$, $x=8 \text{ m}$, $x=10 \text{ m}$, $y=0$, $y=2 \text{ m}$, $y=4 \text{ m}$, $y=6 \text{ m}$, Fig. 6.1).

Comparison Between CDE and MIM Model

BTCs measured by TDR and ERT were analyzed by fitting the convection-dispersion equation (CDE):

$$\frac{\partial C}{\partial t} = D \frac{\partial^2 C}{\partial z^2} - v \frac{\partial C}{\partial z}, \quad [6.4]$$

where C is the resident concentration, D is the dispersion coefficient, v is the pore water velocity, z is depth, and t is time. Also the mobile-immobile transport model (MIM) which accounts for rapid transport in the mobile pore region and a long tailing of the breakthrough curve due to rate limited solute exchange between the immobile and mobile pore regions was applied. The MIM model is expressed by following equations (van Genuchten and Wierenga, 1976):

$$\theta_m \frac{\partial C_m}{\partial t} + \theta_{im} \frac{\partial C_{im}}{\partial t} = \theta_m D_m \frac{\partial^2 C_m}{\partial z^2} - \theta_m v_m \frac{\partial C_m}{\partial z} \quad [6.5]$$

$$\theta_{im} \frac{\partial C_{im}}{\partial t} = \alpha (C_m - C_{im}), \quad [6.6]$$

where the subscripts m and im denote “mobile” and “immobile”, respectively, θ is the volumetric water content, and α is a first-order mass transfer coefficient. For simplicity, mobile water content is often expressed by the dimensionless quantity $\beta = \theta_m / \theta$, where θ is the total volumetric water content.

The CDE model was fitted to both TDR and ERT data whereas the MIM model was only fitted to ERT data. Here, mean electrical conductivities of ERT data were taken from all imaged planes in a related TDR depth. To cover the entire profile investigated by ERT (electrodes were buried down to a depth of 284 cm, Tab. 2.2), depths 247 cm and 292 cm were included additionally. Generally, optimization was performed by means of the CXTFIT code (Toride et al., 1999). Concentration data were considered as resident concentrations or volume averages of the mobile and immobile pore region concentration. As boundary condition, a solute pulse with application time $t_0 = 1 d$ was used. The soil domain was assumed to be initially solute free. For the CDE model, fitted parameters were v , D , and $[\sigma_{b,0} - \sigma_{b,in}] t_0$. For the MIM model, pore water velocity, v , was fixed to the related piston flow velocity, v_q (Eq. [6.3]), and parameters D , α , β , and $[\sigma_{b,0} - \sigma_{b,in}] t_0$ were optimized.

6.4 Results and Discussion

Comparison Between ERT and TDR

Fig. 6.4 shows BTCs derived from TDR and from ERT data in “near neighbor pixels”. For almost all depths (except for 24 cm, 84 cm), electrical conductivities measured by TDR are considerably higher than ERT derived values, particularly at the top. This can be explained by the smoothing in the geoelectric inversion: σ_b rises rapidly in the top layer during tracer application, whereas σ_b is much smaller within lower soil horizons. However, the regularization of the Occam’s inversion (Eq. [3.15]) causes a smearing of the sharp boundary between high and low conductive regions. This issue is also pointed out by Day-Lewis et al. (2005) who investigated the limitations of geophysical data. Singha and Gorelick (2005) underestimated the total tracer mass in their experiment, too. Besides the already mentioned issue of regularization, they also referred to low measurement sensitivity far from the boreholes. Additionally, Vanderborght et al. (2005) pointed out this source of error in their synthetic studies. However, this phenomenon should be less pronounced for the differences shown in Fig. 6.4 since depicted BTCs of ERT are derived from pixels directly located at a borehole where the ERT sensitivity is high. Slater et al. (2002) explained the differences between ERT and direct solute concentration measurements based on the differences in support volume between both methods.

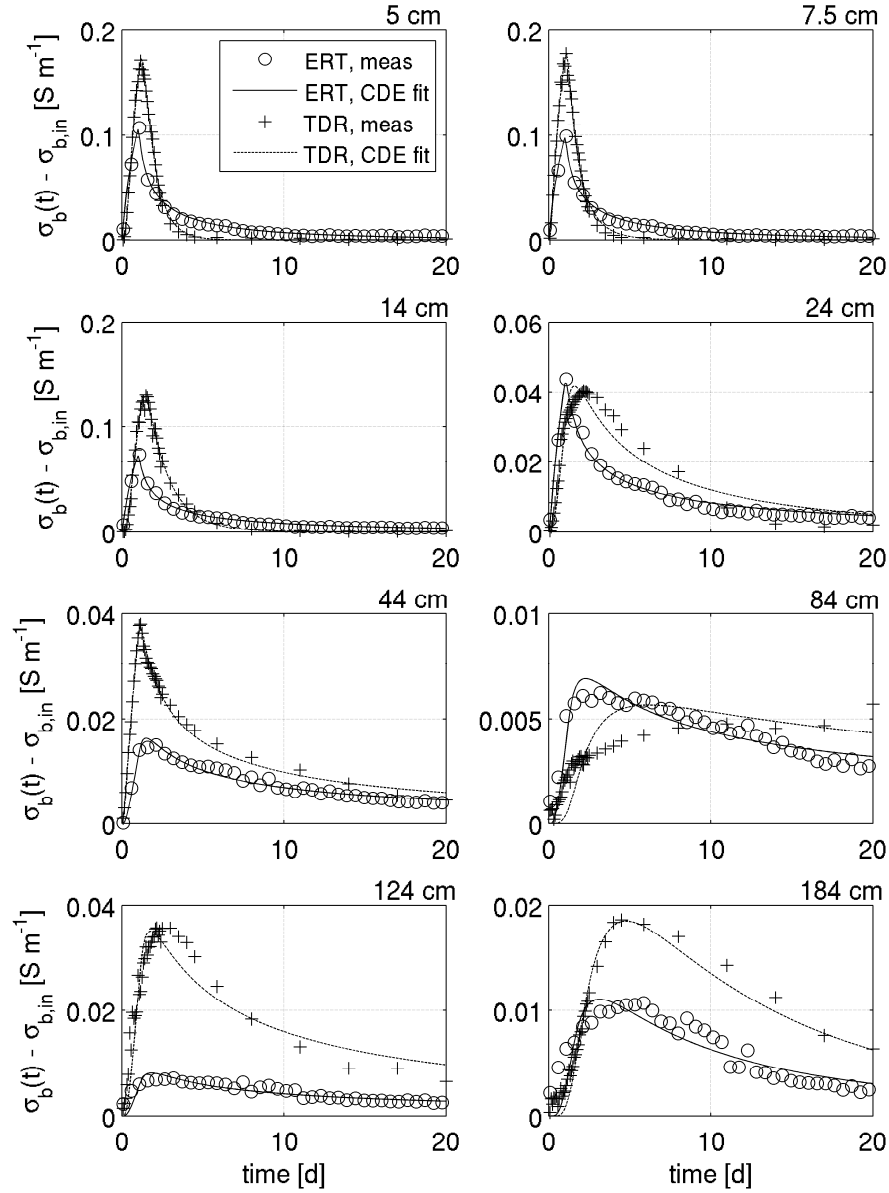


Fig. 6.4: Measured tracer breakthrough (symbols) derived from TDR and ERT. ERT values are taken from grid elements next to TDR probes. Lines indicate CDE model fits.

Hence, different tailings of TDR and ERT based BTCs can be interpreted similarly: In case of TDR, the sampling volume is very small, so preferential flow channels might or might not be included (Mallants et al., 1994). In the current study, TDR probes consisted of three rods with a length of 30 cm, a spacing of 3 cm, and a diameter of 0.3 cm. For three-rod probes, most of the measurement sensitivity is close to the rods (Ferre et al., 1998). The sampling volume of the TDR probe is roughly equal to the length of the rods multiplied by the area of a circle with a diameter that is equal to the distance between the two outer rods. Hence, the resulting sampling area of the TDR probes in a vertical ERT image plane amounts approximately 30 cm². The ERT images are a result of an inversion of resistance measurements and the spatial resolution of the inverted images depends mainly on the used configurations of the electrodes, the regularization that is used to constrain the ill-posed inversion problem, and the spatial distribution of the bulk electrical conductivity. For the used dipole-dipole measurement configuration, the resolution is generally larger close to the electrodes. However, the resolution is difficult to estimate and should in fact be reevaluated for each measurement when the distribution of the bulk electrical conductivity changes. The resolution of the parameter grid that we used (150 cm² at the soil surface to 200 cm² at 184 cm depth) represents an upper boundary of the obtained resolution in the ERT derived images. Therefore, the volume sampled by ERT is expected to include more preferential flow paths leading to more obvious phenomena such as longer tails of BTCs compared to TDR. To investigate whether the differences between TDR and ERT can be explained by spatial variability in transport properties, which should also be reflected in the distribution of ERT based σ_b , mean and percentiles (5th and 95th) of the bulk electrical conductivities are plotted in Fig. 6.5 for several depths.

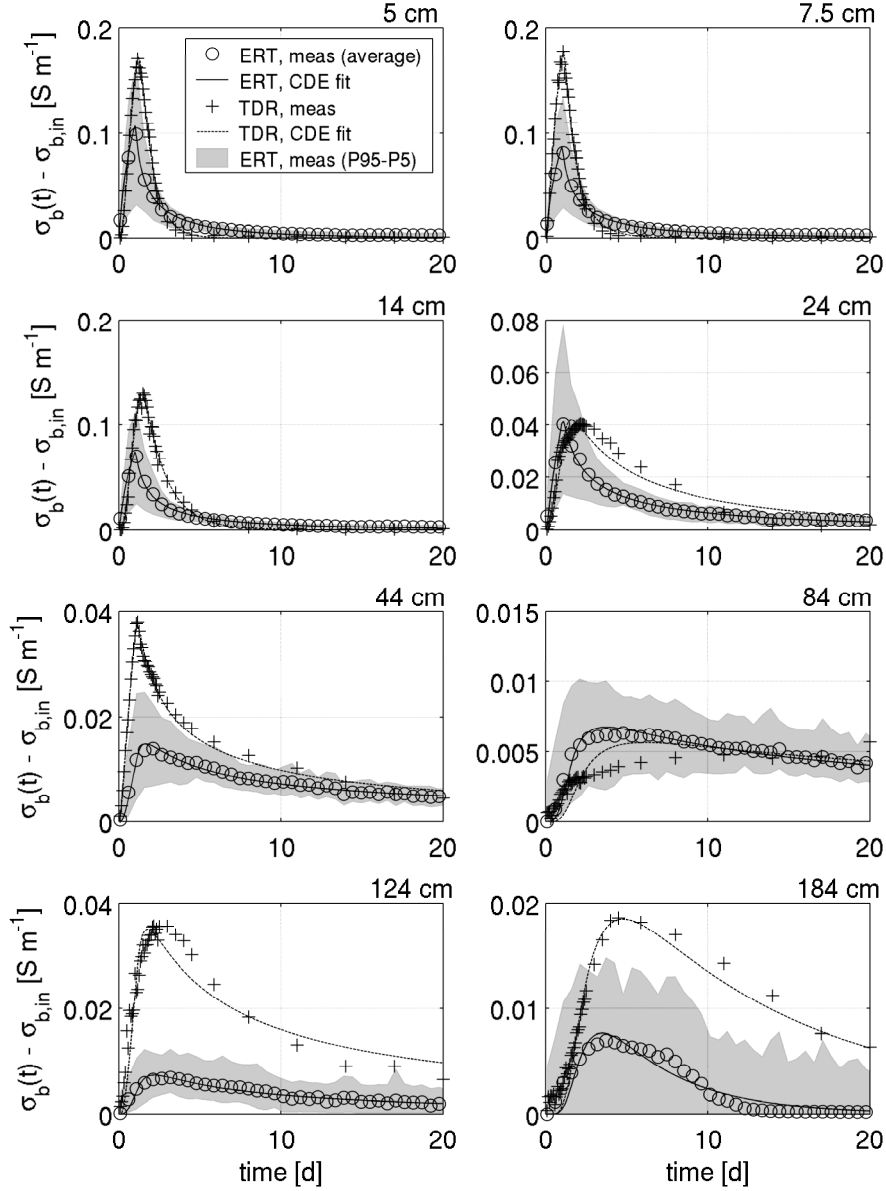


Fig. 6.5: Measured tracer breakthrough (symbols) derived from TDR and ERT, respectively. ERT conductivities are averaged values calculated from all grid elements of the respective depth. Range between 5th and 95th percentiles is plotted as shaded area. Lines indicate CDE model fits.

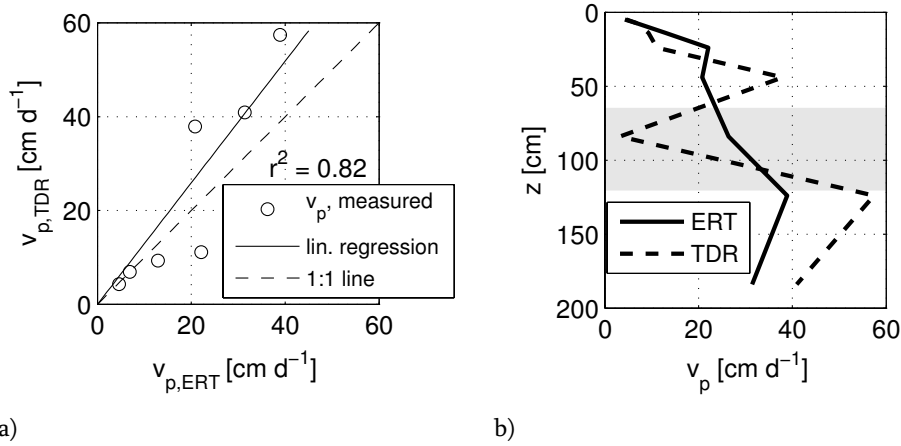
For almost all depths (except for 24 cm, 84 cm), TDR based peak conductivities are higher than ERT based values. For several BTCs (particularly in lower depths), TDR based

conductivities are found beyond the 90 percent range of ERT based values. Only in a depth of 84 cm TDR measurements are completely enclosed by the ERT percentiles. Therefore, it can be concluded that differences between TDR and ERT are not due to spatial variation of the transport process that exists at a scale that is larger than the support volume of the ERT derived conductivities. As a consequence, these differences are caused by the regularization during the ERT inversion or are due to variations of the transport process at a scale that is smaller than the support volume of the ERT derived conductivities.

Tab. 6.1: Flow velocities: piston flow velocity, v_q , peak velocity, v_p , and fitted CDE parameters: pore water velocity, v , dispersion coefficient, D , and the input conductivity, $[\sigma_{b,0} - \sigma_{b,in}] t_0$, derived from ERT and TDR measured BTCs at different depths, z .

z [cm]	v_q [cm d ⁻¹]	v_p [cm d ⁻¹]		v [cm d ⁻¹]		D [cm ² d ⁻¹]		$[\sigma_{b,0} - \sigma_{b,in}] t_0$ [S m ⁻¹ d]	
		ERT	TDR	ERT	TDR	ERT	TDR	ERT	TDR
5	21.53	4.61	4.31	6.04	6.24	185	11	0.33	0.26
7.5	21.72	6.91	6.94	8.26	12.17	425	62	0.34	0.27
14	22.17	12.90	9.33	10.24	10.73	1319	67	0.35	0.29
24	22.43	22.11	11.11	6.54	5.07	1921	250	0.44	0.39
44	22.33	20.79	37.93	2.55	6.26	1144	3034	0.59	0.61
84	22.27	26.37	3.23	0.15	0.05	2093	626	7.82	20.00
124	22.27	38.92	57.41	5.04	9.88	6087	6215	0.42	0.90
184	22.27	31.40	40.90	20.14	17.64	4712	2371	0.19	0.33

Computed peak velocities, v_p , measured by ERT coincide fairly well with those derived from TDR for all depths (Tab. 6.1). An exception is the depth of 84 cm where TDR based v_p is much smaller than the value derived from ERT. But here, TDR measurements were very noisy leading to an apparently late breakthrough. This also leads to a much smaller peak conductivity measured by TDR in a depth of 84 cm (Fig. 6.4). Performing a linear regression between ERT- and TDR- v_p leads to a coefficient of determination of $r^2 = 0.82$ if noisy TDR data in a depth of 0.84 cm are omitted (Fig. 6.6a).



a)

b)

Fig. 6.6: a) Linear regression between peak velocities, v_p , derived from ERT and TDR, respectively. Noisy TDR data in a depth of 0.84 cm are omitted. b) Depth profile of peak velocities, v_p , derived from ERT and TDR, respectively. Shaded area denotes Bt horizon.

Generally, it is obvious from both TDR and ERT measurements that peak velocities in larger depths are much higher than in the uppermost regions, indicating a very fast tracer breakthrough in deeper soil layers (Tab. 6.1, Fig. 6.6b). A rapid change between 84 cm and 124 cm depth is apparent, indicating an acceleration of the fluid from the fine-textured Bt horizon to Bg horizon. This acceleration coincides with a strong decrease in the peak of the electrical conductivity change. This suggests that the acceleration is caused by a considerable decrease in the effective pore volume through which tracer transport takes place. Additionally, below a depth of 124 cm the calculated peak velocity, v_p , significantly exceeds the piston flow velocity, v_q , derived from Eq. [6.3]. A depth profile of ERT based v_p is shown in Fig. 6.10b in comparison with a profile of v_q and will be discussed later on in more detail. This aspect is obviously a further indication of preferential flow processes which are clearly related to horizons underneath the clayey Bt horizon. In order to investigate whether v_p derived in this study (Tab. 6.1) are reasonable, they were cross-checked with values taken from literature. Nimmo (2007) provided a detailed analysis of 64 studies addressing preferential flow. He analyzed solute transport in terms of the fastest portion of the flow, v_{max} , defined as distance traveled divided by the first arrival time of a tracer. For experiments where a continuous water infiltration was applied at the land surface, he obtained a geometric mean $v_{max} = 129 \text{ cm d}^{-1}$ with standard

deviation 53 cm d^{-1} . Germann and Hensel (2006) performed infiltration tests at 25 different sites, leading to 215 v_{\max} values derived from TDR measurements. The majority of velocities ranged between $v_{\max} = 1728 \text{ cm d}^{-1}$ and $v_{\max} = 3456 \text{ cm d}^{-1}$. In contrast, maximal v_p observed in the current study only amounted 31.4 cm d^{-1} for ERT and 40.9 cm d^{-1} for TDR, respectively (Tab. 6.1). Those considerable deviations originate from the fact that we calculated v_p on the basis of the peak arrival time instead of the first arrival time. This was done with respect to the relatively low temporal and spatial resolution of ERT which makes it difficult to derive first arrival times from BTCs.

ERT based BTCs lead to higher dispersion coefficients than the TDR based BTCs, except for depths 44 cm and 124 cm (Tab. 6.1). Köstel et al. (2008) also report on higher dispersivities obtained from ERT compared to those derived from TDR. Here, this aspect is especially conspicuous at the top and can be explained by longer tailings of BTCs (Fig. 6.4). Vanderborght et al. (2005) found that dispersivity derived from ERT data might be overestimated due to loss of spatial resolution in the ERT images. Kemna et al. (2002) pointed out that the estimation of dispersivity is sensitive to the regularization chosen in the geophysical inversion.

Comparison Between CDE and MIM Model

The CDE fits the observed BTCs generally well (Fig. 6.4). The misfit between the CDE model and the measurements is considerably smaller than the difference between the ERT and TDR measurements. Despite the relatively good fit by the CDE model, the fitted parameters indicate that the CDE is not an adequate model to explain the observed transport process (Tab. 6.1): The fitted pore water velocity is considerably smaller than the piston flow velocity and fitted dispersion coefficients are unrealistically high. Therefore, the MIM model (Eqs. [6.5], [6.6]) was fitted to ERT data. For comparison, Fig. 6.7 shows mean ERT σ_b together with the CDE and MIM fits. Parameters of both models are summarized in Tab. 6.2.

In the uppermost depths there is no significant difference recognizable between the fits of the CDE and MIM models. The MIM, in which the pore water velocity was fixed to the piston flow velocity, could equally well describe the breakthrough as the CDE model with a pore water velocity that was considerably smaller than the piston flow velocity. The slower breakthrough in the top soil layer could therefore be explained by rapid transport through only a small part of the pore volume in combination with a rapid mass exchange between the mobile and immobile pore regions.

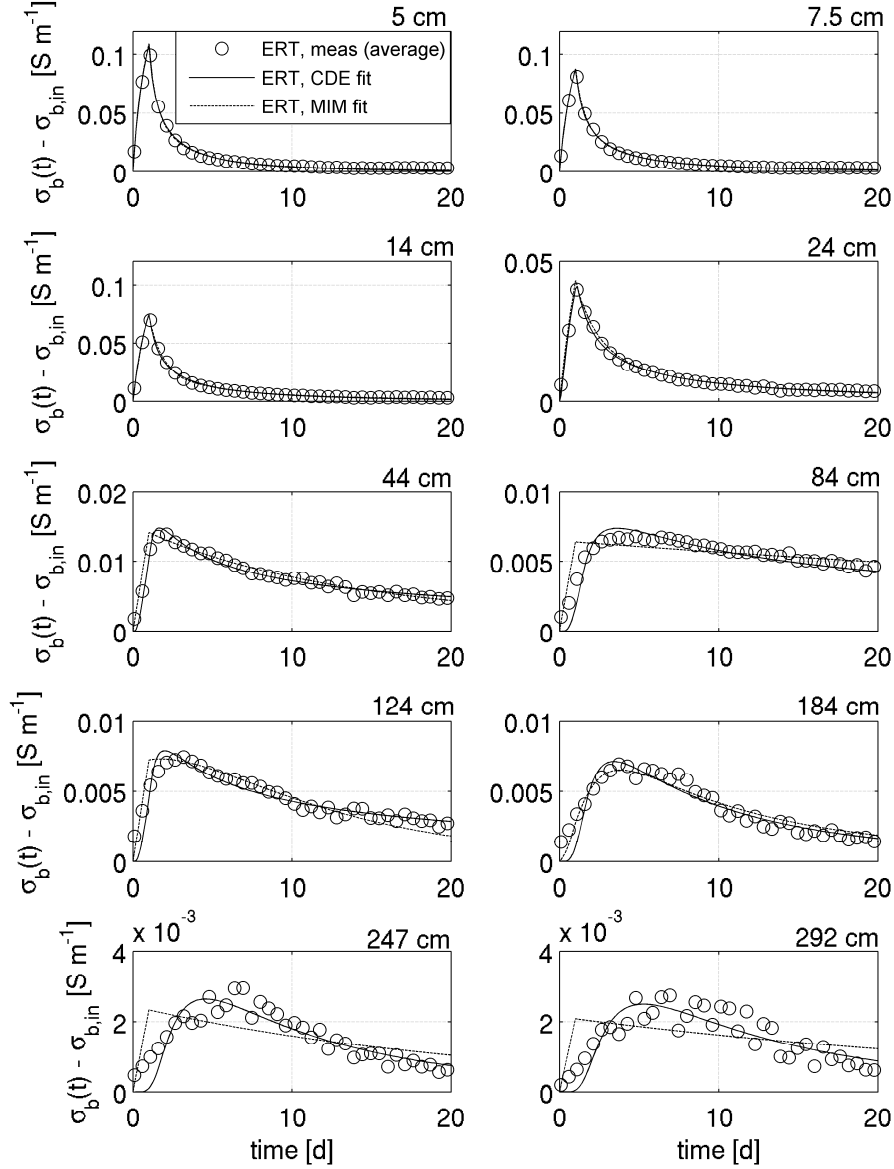


Fig. 6.7: Measured tracer breakthrough (open circles) derived from ERT. Conductivities are averaged values calculated from all grid elements of the respective depth. Solid lines represent fits of the CDE model, dashed lines fits of the MIM model, where pore water velocity is fixed to piston flow velocity.

Such a rapid mass exchange can be linked to the structure of the top soil layer which consists of loose and well aggregated soil. Below a depth of 84 cm, the quality of the MIM

fit is clearly worse than that of the CDE model (except for 184 cm). This is due to the lower degree of freedom caused by fixed pore water velocities.

Tab. 6.2: CDE (v pore water velocity, D dispersion coefficient, and $[\sigma_{b,0} - \sigma_{b,in}]t_0$ input conductivity) and MIM transport parameters (D dispersion coefficient, $[\sigma_{b,0} - \sigma_{b,in}]t_0$ input conductivity, α mass transfer coefficient, and β relative mobile water content) derived from fits to average BTCs at different depths, z , obtained with ERT. For the MIM model, v was not fitted but fixed to piston flow velocity.

$z [cm]$	$v [cm d^{-1}]$		$D [cm^2 d^{-1}]$		$\beta = \theta_m / \theta$ [-]	$\alpha [d^{-1}]$	$[\sigma_{b,0} - \sigma_{b,in}]t_0$ [$S m^{-1} d$]	
	CDE	MIM ⁺	CDE	MIM	MIM	MIM	CDE	MIM
5	8.97	21.53	229	1643	0.0001 ^l	0.1773	0.26	0.26
7.5	10.60	21.72	452	2286	0.0001 ^l	0.1367	0.24	0.24
14	15.87	22.17	1334	3403	0.0024	0.3794	0.24	0.24
24	9.95	22.43	1443	10000 ^u	0.0001 ^l	0.0479	0.26	0.28
44	1.22	22.33	950	10000 ^u	0.0001 ^l	0.0053	1.11	0.27
84	0.84	22.27	1114	6329	0.0001 ^l	0.0007	1.51	0.50
124	5.11	22.27	5272	1801	0.0001 ^l	0.0168	0.39	0.11
184	23.27	22.27	3775	3994	0.0001 ^l	0.1017	0.10	0.11
247	26.61	22.27	4276	527	0.0001 ^l	0.0020	0.04	0.06
292	27.22	22.27	5015	856	0.0001 ^l	0.0013	0.05	0.07

⁺ fixed

^l lower bound

^u upper bound

Noticeable is the dramatic decrease of the mass transfer coefficient, α , in the soil profile, exhibiting a minimum in a depth of 84 cm (Fig. 6.8). This means that the exchange into the immobile phase is significantly reduced here (Tab. 6.2). The depth of 84 cm is located within the Bt horizon indicating that this horizon is the initiator of preferential flow processes (Fig. 6.8).

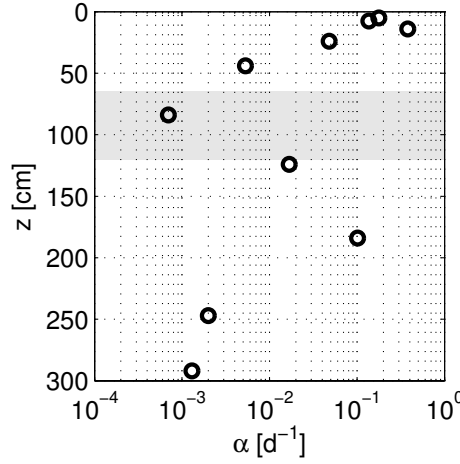


Fig. 6.8: Depth profile of mass transfer coefficient, α , taken from Tab. 6.2. Shaded area denotes the Bt horizon.

In this study, BTCs of volume averaged or resident concentrations were measured. Derivation of pore water velocities from BTCs of resident concentrations requires a translation of resident to flux concentrations since pore water velocity is inverse proportional to the first temporal moment of the flux concentration breakthrough curve. This translation depends on the transport model. A corner stone assumption of the CDE model is that solute fluxes are linearly related to a concentration gradient of resident concentrations. In the MIM, the flux concentrations are related only to the resident concentrations in the mobile pore region, which may be a small part of the total pore region. As a consequence, small total resident concentrations may be linked with large flux concentrations when the solute mass is mainly in the mobile pore region and the volume of this pore region is small. To illustrate the difference between the two models, which predict very similar resident concentration breakthrough curves, breakthrough curves of flux concentrations that are predicted by both models are shown in Fig. 6.9.

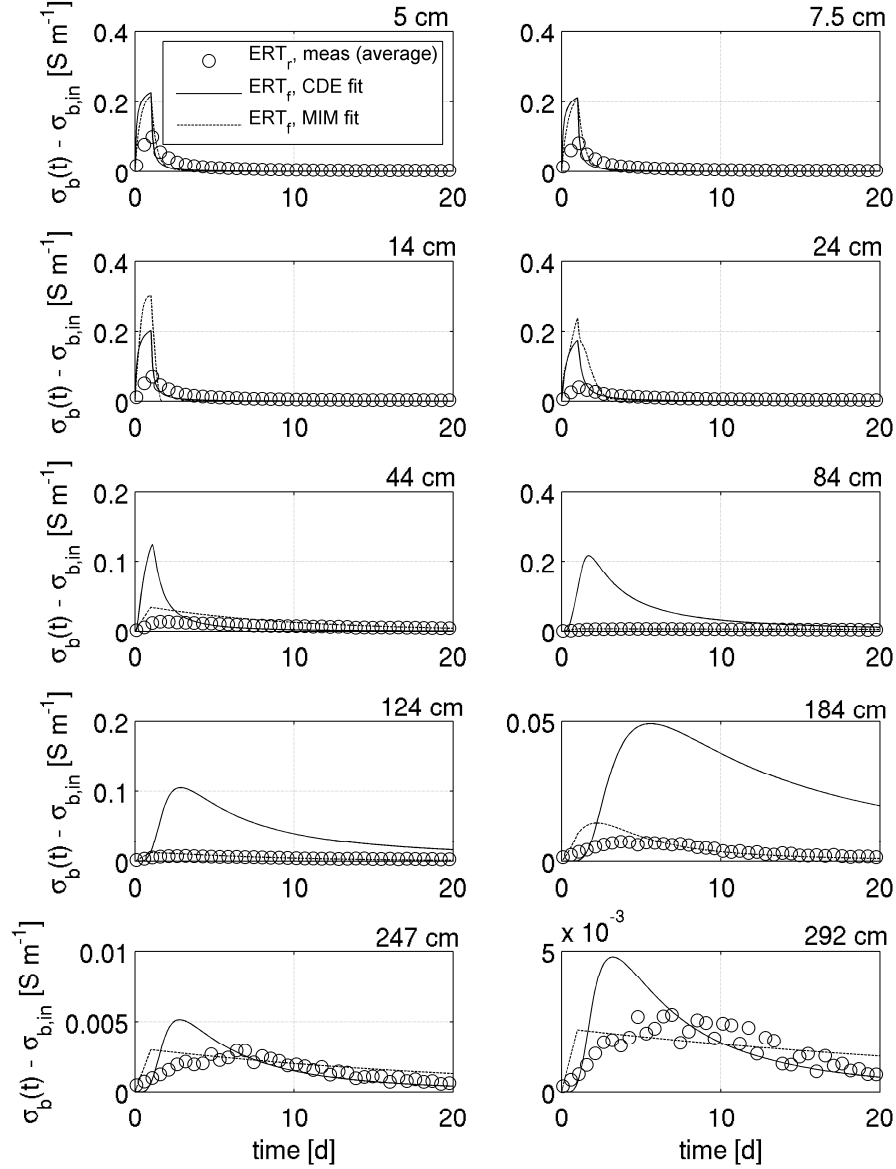


Fig. 6.9: Measured resident concentrations (open circles) and flux concentrations predicted by CDE and MIM models that were fitted to resident concentrations. Concentrations are expressed in terms of σ_b , resident concentrations are denoted by index “r”, flux concentrations by index “f”.

These predicted flux concentration BTCs show large differences between the MIM and CDE, particularly in lower depths. Hence, they demonstrate the impact of the transport

model that is assumed when resident concentration BTCs are interpreted. Since the fitted pore water velocity is considerably smaller than the expected piston flow velocity and since the fitted dispersion coefficients are unrealistically high (Tab. 6.1), it is questionable whether the CDE model that was fitted to resident concentration BTCs can predict flux concentrations when preferential flow occurs. Underestimation of the pore water velocity that was derived from a CDE fit to a resident concentration breakthrough curve was also observed in other studies and attributed to preferential transport through a small fraction of the pore space (Vanderborght et al., 2000).

Spatial Analysis of ERT based Solute Transport

Although the BTCs can be fitted fairly well by the CDE model, the obtained CDE parameters appear to be non realistic. Therefore, the spatial distributions of the peak velocity and the peak soil bulk conductivities are considered in a further analysis of the transport heterogeneity. Fig. 6.10a shows the mean peak conductivities, $\sigma_{b,p} - \sigma_{b,in}$, with 10th and 90th percentiles derived for each depth of the geophysical inversion grid. At locations with very low $\sigma_{b,p} - \sigma_{b,in}$, very high peak velocities were derived. Although the values are still within the range of v_{max} reported by Nimmo (2007) and Germann and Hensel (2006), they have to be interpreted as artifacts: These result from changes in electrical conductivity in the upper part of the soil profile due to the smoothness constraint in the ERT inversion. Those BTCs were identified by a low plateau concentration after short time instead of a peak concentration. Hence, only BTCs were considered for further analysis in which $\sigma_{b,p} - \sigma_{b,in}$ exceeded a threshold of $\sigma_t = 8.4 \cdot 10^{-4} \text{ S m}^{-1}$. This value is the 5th percentile of the distribution of all $\sigma_{b,p} - \sigma_{b,in}$.

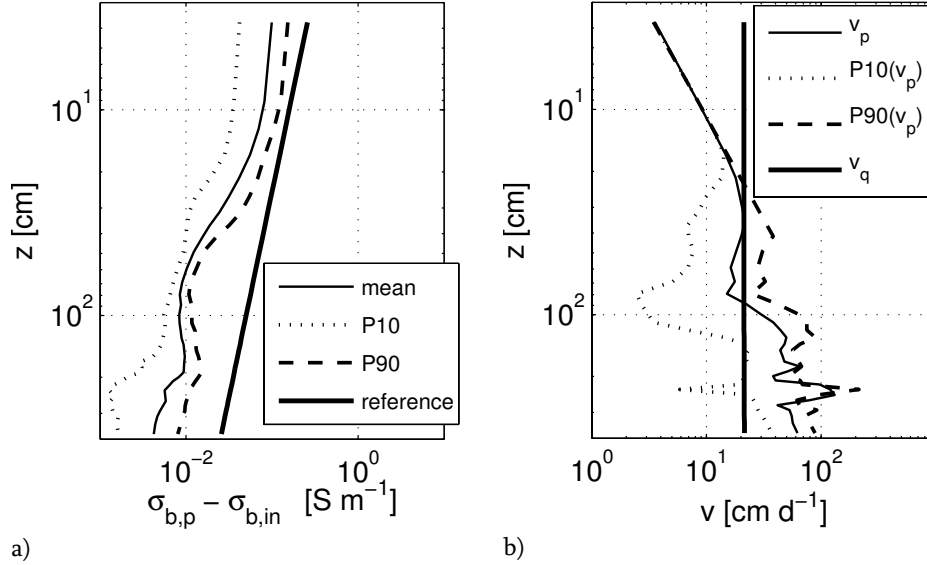


Fig. 6.10: a) Corrected mean peak conductivity, $\sigma_{b,p} - \sigma_{b,in}$, and its 10th and 90th percentiles, indicated by P10 and P90, respectively. Thick black line represents a reference illustrating a decrease with $1/z^{0.5}$. b) Mean peak velocity, v_p , and its 10th and 90th percentiles, indicated by P10(v_p) and P90(v_p), respectively. Piston flow velocity, v_q , is shown for comparison.

For a constant dispersion coefficient, the peak concentration is expected to decrease with $1/z^{0.5}$ due to dilution. But here, it is evident that peak conductivities decrease dramatically below a depth of about 20 cm (i.e., underneath the A horizon). On the other hand, the peak conductivity remains almost constant below 65 cm, which is the upper boundary of the Bt horizon. Furthermore, a rapid reduction is observed in a depth of about 190 cm. Those strong declines can be caused by two mechanisms. The first is a “non-Fickian” transport process in which the dispersion coefficient increases with depth. A second is a change of the pore volume in which transport takes place with depth. The peak σ_b represents a volume weighted average of the concentrations in the mobile and immobile pore regions (Singha et al., 2007). A decrease with depth of the pore volume with mobile water also results in a decrease in peak σ_b with depth. This relationship may also explain an increase of σ_b with depth: Below the Bt horizon, i.e., below a depth of 120 cm, a slight increase in peak σ_b can be observed. This increase cannot be explained by a transport process but it can be attributed to a rise in the pore volume of mobile water. As a

consequence, spatial patterns of peak conductivities also contain indirect information about the pore volume in which transport takes place.

In contrast to the peak conductivities, the mean peak velocities are low at the top and increase rapidly within the uppermost 25 cm, as shown in Fig. 6.10b. Additionally, mean piston flow velocity, v_q , interpolated from data provided in Tab. 6.1 was plotted. It can be seen that below 90 cm depth, the peak velocities become significantly larger than the piston flow velocities. This supports the conclusion drawn from the analysis of mass exchange coefficients, α , (Tab. 6.2) where the initialization of preferential flow was also related to a depth of 80 cm, located within the compacted Bt horizon.

Generally, it is obvious that the spread around the mean illustrated by the range between the percentiles (Fig. 6.10b) is very high. Most apparent is the depth between 200 cm and 300 cm. This can be linked to the lithology since below a depth of 200 cm gravel of a river terrace was found, causing partially high velocities.

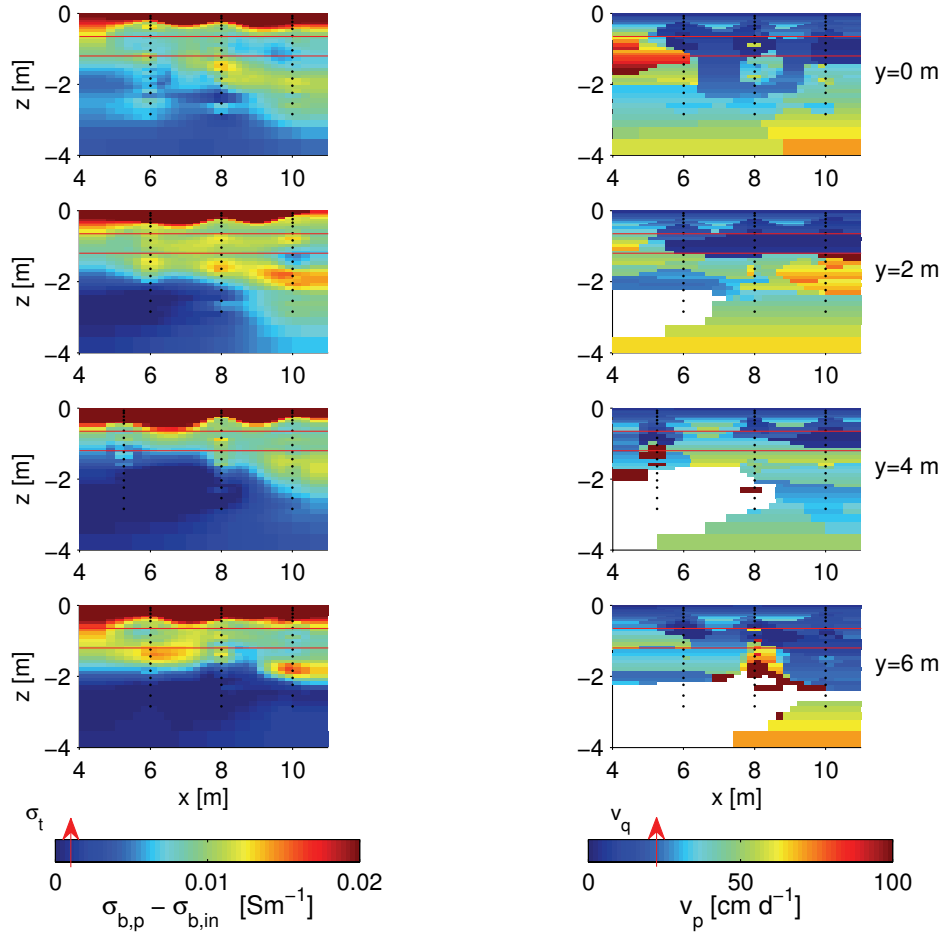


Fig. 6.11: Two-dimensional distributions of corrected peak electrical conductivities, $\sigma_{b,p} - \sigma_{b,in}$, (left) and peak velocities, v_p , (right). v_p related to $\sigma_{b,p} - \sigma_{b,in} < 8.4 \cdot 10^{-4} \text{ S m}^{-1}$ (denoted by σ_t in the left colorbar) are blanked out. Mean piston flow velocity ($v_q = 22 \text{ cm d}^{-1}$) is marked in the right colorbar. Maps are shown exemplary for planes in x-direction. Black dots represent electrode positions, Bt horizon is denoted by red lines.

To discuss the spatial variation of peak concentrations and peak velocities in more detail 2D-maps of $\sigma_{b,p} - \sigma_{b,in}$ and v_p for the different planes in x-direction are illustrated in Fig. 6.11. Similar to Fig. 6.10, the 2D-maps also reflect a rapid decrease of peak σ_b within the uppermost 30 to 60 cm. This large peak conductivity at the top (i.e., in the A horizon) can be explained by a lower dry bulk density, $\rho_{d,b}$, (Tab. 2.1) caused by coarser material and organic matter. The drop in peak σ_b is clearly related to the upper bound of the Bt horizon although it is evident that this limit cannot be drawn sharply within one depth. It can also be seen that the volume in which transport takes place rises again underneath the Bt horizon (yellowish to red spots below Bt horizon, Fig. 6.11, left). But it is obvious that the locations of these zones are variable in vertical as well as horizontal direction. However, these locations are consistent in each plane (e.g., by anomaly with coordinates $x=10$ m, $z=-2$ m), indicating partly homogeneous soil structures in y-direction. In a depth of about 200 cm, where the dense river terrace is present, peak σ_b drops enormously. This is again information about preferential flow phenomena appearing in this layer. However, the depth of the top of the buried river terrace increases in all planes for $x=8$ m to 10 m.

As already mentioned, at locations with very low peak concentrations, very high v_p may be due to artifacts and pixels with $\sigma_{b,p} - \sigma_{b,in} < 8.4 \cdot 10^{-4} \text{ S m}^{-1}$ were blanked out in Fig. 6.11 (right). Contrary to the peak σ_b , the peak velocities, v_p , are low at the surface (Fig. 6.11, right). In particular for $y=0$ m and $y=2$ m, a belt of low velocities is cognizable which coincides with the Bt horizon. This is also the boundary below which the peak velocities get larger than the mean piston flow, meaning again that preferential flow is initiated here. Generally, the variability of v_p is much higher compared to the variability of peak σ_b . Spots of high peak velocities occur within the Bt horizon as well as in deeper horizons (i.e., the dense river terrace), but they are never found in the uppermost 60 cm.

6.5 Conclusions

A tracer experiment was performed at a forest site with a structured soil. To derive solute transport properties of the soil from breakthrough curves, TDR as well as ERT measurements were conducted. The comparison between both techniques showed that bulk electrical conductivity, σ_b , derived from ERT underestimated that derived from TDR. This deviation could not only be explained by different sample locations and spatial variability of soil properties. Therefore, differences between TDR and ERT are assumed to be caused by regularization effects induced by the geophysical inversion and by differences in support volume. Nevertheless, relative changes of bulk electrical conductivities contain valuable information about solute transport: BTCs obtained from both techniques illustrated preferential flow phenomena indicated by rapid peak arrival times in lower depths and long tailings. To parameterize BTCs the convection-dispersion equation (CDE) was fitted to both TDR and ERT based data. Pore water velocities, v , derived from CDE fits to BTCs obtained with ERT and TDR were in good agreement (Tab. 6.1). Long tailings could properly be described by higher dispersion coefficients. However, the fitted CDE parameters lacked a physical meaning, i.e., the obtained dispersion coefficients were very large. If a dispersivity length, D/v , is calculated, the obtained values are much larger than those typically observed in soils (Vanderborght and Vereecken, 2007). Therefore, it was investigated whether the application of a mobile-immobile model (MIM) to ERT data led to a more reasonable parameterization. Here, the pore water velocity was fixed to the piston flow velocity according to the irrigation rate and the water content. Although the MIM fitted the resident concentration BTCs worse than the CDE model due to the fixed pore water velocity, the correspondence between the two model fits was relatively large. However, the BTCs of predicted flux concentrations by the two models differed considerably. This illustrates that the parameterization of transport models on the basis of resident concentration breakthrough curves is problematic when preferential flow occurs.

Therefore, we used the peak bulk conductivity and peak velocity of observed resident concentration BTCs from ERT to characterize the preferential transport that was observed in this study. Comparing peak velocities with piston flow velocities, it was obvious that below a depth of 80 cm the peak velocity exceeded the piston flow velocity. This

corresponds with the depth of a compacted Bt horizon which has a considerably lower hydraulic conductivity of the soil matrix than the top soil. Besides an increase in peak velocity from the surface to the Bt horizon, a drastic decrease in the peak electrical bulk conductivity was observed, which is attributed to a smaller pore volume in which rapid tracer transport takes place. Additionally, a conspicuous drop in fitted mass transfer coefficient, α , between the top soil and the Bt horizon indicated that preferential flow was initiated at the top of the Bt horizon. Finally, local structures of peak σ_b and peak v_p could be identified in 2D maps derived from ERT. Due to the fact that similar structures often occurred in independently inverted ERT planes, it can be concluded that those anomalies represented indeed geologic realities which have an impact on the spatial variability of the preferential transport process. Hence, ERT turned out to be a promising means to map preferential flow. Although the method cannot resolve the tracer movement on the scale of the individual preferential flow paths, it offers the possibility to image the spatial distribution of the volume through which transport takes place and the related velocity within the flow paths. The results of our study indicated that the preferential flow process is spatially variable. It varies with depth due to soil layers with different properties and it also varies laterally with larger zones that are bypassed by preferential flow which furthermore varies from location to location. Implementation of these vertical and lateral variations in an effective parameterization of preferential transport models remains a challenge.

7 Summary and Conclusions

Three main issues were addressed in this thesis: First of all, an analysis of data errors was conducted to describe them statistically and to investigate their impact on the inversion results (chapter 4). This information was incorporated in a study where the seasonal variation of soil water content was observed by means of real measured ERT data (chapter 5). Finally, a tracer experiment was interpreted where ERT was used to monitor changes in electrical conductivity both temporally and spatially (chapter 6).

In the study dealing with data errors (chapter 4) earth models were derived from real measured TDR measurements for a dry and a wet scenario, respectively. Corresponding ERT resistances were calculated and finally noised by means of an error distribution which was obtained from real measured ERT data sets. There were three main conclusions derived from this Monte Carlo experiment: First of all, it was obvious that there was a certain “overlap” between the standard deviations of the respective realizations obtained from both scenarios. Hence, theoretically it can happen that an ERT data set taken in a wet soil leads to more resistive results than a data set taken in a desiccated soil. This uncertainty was effectively reduced when those data with the highest data error were eliminated prior to inversion. Finally, it turned out that for high error levels as present in the current data and a layered earth model, the error is dependent on electrode configurations rather than on resistances. This justified the idea to apply also error models within the geophysical inversion which are specifically related to each configuration. In fact, the difference of the mean electrical conductivity taken from both scenarios, dry and wet, was more significant compared to the “classical” approach of error treatment.

Therefore, this error model dependent on electrode configurations was also adapted to a study where real measured ERT data were tested to describe naturally occurring changes in soil water contents (chapter 5). For the calibration of the petrophysical relationship, a relatively short time window was used to derive a function which describes the relationship between TDR- θ and ERT- σ_b . ERT resistances were inverted twice, once by means of the “classical” error model dependent on resistances and once by means of the error model dependent on electrode configurations. After that, water contents were achieved from ERT over a period of nine months. Unlike the results of the synthetic experiment, the difference between water contents obtained from both error models was not that pronounced in this case. However, there were far less outliers when the error model dependent on electrode configurations was used. The fact that the benefit of adopting this model was more distinct within the synthetic experiment (chapter 4), can be explained by the respective levels of data errors: If the error was calculated in dependence of the amount of the resistance, a relative error of about 13 % was obtained for the synthetic experiment, whereas a mean relative error of only 6 % was achieved for the experiment to monitor the seasonal soil water changes. The most obvious explanation for

this huge difference is that for the latter case the filter conditions were stricter. Here, data with a variability of the potential trace, CV_t , (Eq. [3.4]) exceeding 5 % were not considered in the inversion. Hence, it can be concluded that an inversion with an error model dependent on the electrode configuration makes sense for very noisy data. However, removal of noisy data is even more important to obtain unique inversion results. Additionally, it turned out that for time-lapse monitoring of soil water contents the application of a median filter was highly effective when it has to be dealt with considerable ERT data errors. This could be verified by the comparison with a time series of water contents which were obtained from TDR measurements. Although a median filter cuts off the peaks occurring in a time series of water contents, it could be shown that there is still enough information contained in the filtered data to describe single but heavy rain events. Furthermore, a long-term observation of soil water contents measured by ERT revealed locations of lower moisture during dry spells which could be assigned to tree roots. Hence, ERT turned out to be an appropriate means to observe soil water dynamics as well as tree root activity spatially.

In chapter 6 a tracer experiment was analyzed which was also observed by means of ERT. Due to a new measurement configuration, i.e., cross-hole current injection, smaller geometry factors led to optimized signal to noise ratios, making an additional smoothing with a median filter dispensable. However, TDR based breakthrough curves, which served again as reference, were underestimated in several depths. Peak bulk electrical conductivity and peak velocity of observed resident concentration BTCs were used to demonstrate preferential flow: High peak velocities and low peak electrical conductivities, which are related to a smaller pore volume where rapid tracer transport occurs, could be clearly assigned to the compacted Bt-horizon of the soil profile. Furthermore, similar anomalies in soil properties, again characterized by peak velocity and peak electrical conductivity, could be verified in different parallel 2D sections. This shows that those structures are really existent perpendicular to the investigated planes rather than exhibiting only artifacts in the different sections. Therefore, it can be concluded that preferential flow can be detected indirectly by means of ERT by using peak σ_b as a proxy which illustrates the volume of rapid tracer transport.

Finally, the following overall conclusions can be summarized from the analysis of time-lapse ERT measurements: ERT data generally contained valuable information in terms of state variables of the soil such as water content but also in terms of solute transport properties. A further essential feature consisted in the more dimensional mapping of those quantities. To obtain inversion results as reliable as possible, it turned out that it is crucial to discard noisy data prior to inversion. A “cleaned” data set with few data contained more information than a large data set including measurements of low-quality. This could be

accomplished either by means of a threshold regarding the stacking error of the voltage traces, which was delivered from the measurement device, or by means of reciprocal measurements, if available. Hence, it was important to visualize and inspect already raw data. Furthermore, it was important to evaluate the data error level and to incorporate this information in an appropriate error model rather than the error estimation using a rule of thumb. For smaller relative errors in resistance (i.e., smaller than 7 %) it was sufficient to calibrate a commonly used error model for the entire data set which assumes a linear relationship between resistance and the error in resistance. For larger errors (i.e., larger than 10 %) and a layered earth model it turned out that the error depends on the electrode configuration rather than on the resistance. To weight those data accurately within the inversion, the error should be determined specifically for each measurement geometry. Finally, the development of time-lapse parameters could be improved considerably if a median filter over time was applied. But if that approach is adapted, it is advisable to increase the temporal measurement density as much as possible to still capture natural soil water dynamics.

However, future activities should still be focussed on an improved quality of raw data and on the further development of inversion techniques such as joint inversion, stochastic inversion, and time-lapse inversion, which all include additional information to constrain the final model parameters.

8 Bibliography

- al Hagrey, S. A., and J. Michaelson, 1999, Resistivity and percolation study of preferential flow in vadose zone at Bokhorst, Germany, *Geophysics*, **64**, 746-753.
- Alumbaugh, D. L., and G. A. Newman, 2000, Image appraisal for 2D and 3D electromagnetic inversion, *Geophysics*, **65**, 18.
- Amidu, S. A., 2007, Geoelectric studies of seasonal wetting and drying of a Texas Vertisol, *Geoelectric studies of seasonal wetting and drying of a Texas Vertisol*.
- Ammann, C., 1999, *On the applicability of relaxed eddy accumulation and common methods for measuring trace gas fluxes*.
- Archie, G. E., 1942, The electrical resistivity log as an aid in determining some reservoir characteristics, *Trans. Am. Inst. Min. Metall. Pet. Eng.*, **146**, 54 - 67.
- Barker, R., 1998, The application of time-lapse electrical tomography in groundwater studies, *Geophysics*, **17**, 1454.
- Battle-Aguilar, J., S. Schneider, M. Pessel, P. Tucholka, Y. Coquet, and P. Vachier, 2009, Axisymmetrical Infiltration in Soil Imaged by Noninvasive Electrical Resistivity, *Soil Sci Soc Am J*, **73**, 510-520, doi: 10.2136/sssaj2007.0278.
- Binley, A., A. Ramirez, and W. Daily, 1995, Regularised image reconstruction of noisy electrical resistance tomography data, paper presented at 4th Workshop of the European Concerted Action on Process Tomography, Eur. Concerted Action on Process Tomography, Bergen.
- Binley, A., S. Henry Poulter, and B. Shaw, 1996, Examination of solute transport in an undisturbed soil column using electrical resistance tomography, *Water Resources Research*, **32**, 763-769.
- Binley, A., G. Cassiani, R. Middleton, and P. Winship, 2002a, Vadose zone flow model parameterisation using cross-borehole radar and resistivity imaging, *Journal of Hydrology*, **267**, 147-159.
- Binley, A., P. Winship, L. J. West, M. Pokar, and R. Middleton, 2002b, Seasonal variation of moisture content in unsaturated sandstone inferred from borehole radar and resistivity profiles, *Journal of Hydrology*, **267**, 160-172.
- Binley, A., and A. Kemna, 2005, Electrical Methods, in *Hydrogeophysics*, edited by R. a. Hubbard, pp. 129-156, Springer.
- Bogena, H., M. Herbst, J.-F. Hake, R. Kunkel, C. Montzka, T. Pütz, H. Vereecken, and F. Wendland, 2005, *MOSYRUR :Water balance analysis in the Rur basin*, Forschungszentrum, Zentralbibliothek, Jülich.

- Briggs, L. J., 1899, Electrical instruments for determining the moisture, temperature, and soluble salt content of soils, USDA Div. Soils Bull. 10. U.S. Gov. Print. Office, Washington, DC.
- Cassiani, G., A. Godio, S. Stocco, A. Villa, R. Deiana, P. Frattini, and M. Rossi, 2009, Monitoring the hydrologic behaviour of a mountain slope via time-lapse electrical resistivity tomography, *Near surface geophysics*, **7**, 475-486.
- Daily, W., W. Lin, and T. Buscheck, 1987, Hydrological Properties of Topopah Spring Tuff - Laboratory Measurements, *Journal of Geophysical Research-Solid Earth and Planets*, **92**, 7854-7864.
- Daily, W., A. Ramirez, D. LaBrecque, and J. Nitao, 1992, Electrical-Resistivity Tomography of Vadose Water-Movement, *Water Resources Research*, **28**, 1429-1442.
- Daily, W., A. Ramirez, A. Binley, and D. LaBrecque, 2004, Electrical resistance tomography, *The Leading Edge*, **23**, 438-442.
- Day-Lewis, F. D., K. Singha, and A. M. Binley, 2005, Applying petrophysical models to radar travel time and electrical resistivity tomograms: Resolution-dependent limitations, *Journal of Geophysical Research*, **110**, B08206, doi: 10.1029/2004jb003569.
- Deiana, R., G. Cassiani, A. Villa, A. Bagliani, and V. Bruno, 2008, Calibration of a vadose zone model using water injection monitored by GPR and electrical resistance tomography, *Vadose Zone Journal*, **7**, 215-226.
- FAO/ISRIC/ISSS, 1998, World Reference Base for Soil Resources, World Soil Resources Report, **84**, FAO, Rome.
- Ferre, P. A., J. H. Knight, D. L. Rudolph, and R. G. Kachanoski, 1998, The sample areas of conventional and alternative time domain reflectometry probes, *Water Resources Research*, **34**, 2971-2979.
- Feyen, J., D. Jacques, A. Timmerman, and J. Vanderborght, 1998, Modelling water flow and solute transport in heterogeneous soils: A review of recent approaches, *Journal of Agricultural Engineering Research*, **70**, 231-256.
- Franson, M. A. H., 1985, *Standard methods for the examination of water and wastewater. 16th ed. Am. Public Health Assoc.*, Washington, DC.
- Germann, P. F., and D. Hensel, 2006, Poiseuille Flow Geometry Inferred from Velocities of Wetting Fronts in Soils, *Vadose Zone Journal*, **5**, 867-876, doi: 10.2136/vzj2005.0080.
- Huisman, J., S. Hubbard, J. Redman, and A. Annan, 2003, Measuring Soil Water Content with Ground Penetrating Radar A Review, *Vadose Zone Journal*, **2**, 476-491.
- Jacques, D., D. J. Kim, J. Diels, J. Vanderborght, H. Vereecken, and J. Feyen, 1998, Analysis of steady state chloride transport through two heterogeneous field soils, *Water Resources Research*, **34**, 2539-2550.

- Javaux, M., and M. Vanclooster, 2003, Scale- and rate-dependent solute transport within an unsaturated sandy monolith, *Soil Science Society of America Journal*, **67**, 1334-1343.
- Kachanoski, R. G., E. Pringle, and A. Ward, 1992, Field Measurement of Solute Travel-Times Using Time Domain Reflectometry, *Soil Science Society of America Journal*, **56**, 47-52.
- Kachanoski, R. G., J. L. Thony, M. Vauclin, G. Vachaud, and R. Laty, 1994, Measurement of Solute Transport during Constant Infiltration from a Point-Source, *Soil Science Society of America Journal*, **58**, 304-309.
- Kaimal, J. C., and J. J. Finnigan, 1994, *Atmospheric boundary layer flows: their structure and measurements*, Oxford University Press, New York.
- Kemna, A., 2000, Tomographic inversion of complex resistivity—Theory and application, Ph.D. thesis, Bochum University.
- Kemna, A., A. Binley, A. Ramirez, and W. Daily, 2000, Complex resistivity tomography for environmental applications, *Chemical Engineering Journal*, **77**, 11-18.
- Kemna, A., J. Vanderborght, B. Kulesa, and H. Vereecken, 2002, Imaging and characterisation of subsurface solute transport using electrical resistivity tomography (ERT) and equivalent transport models, *Journal of Hydrology*, **267**, 125-146.
- Knaps, A., 2006, knusalic: Eddy-Kovarianz-Messung mit USA-1 und LI-7500, edited.
- Köhne, J. M., S. Köhne, and J. Simunek, 2009, A review of model applications for structured soils: a) Water flow and tracer transport, *Journal of Contaminant Hydrology*, **104**, 4-35, doi: DOI 10.1016/j.jconhyd.2008.10.002.
- Köstel, J., A. Kemna, M. Javaux, A. Binley, and H. Vereecken, 2008, Quantitative imaging of solute transport in an unsaturated and undisturbed soil monolith with 3-D ERT and TDR, *Water Resources Research*, **44**, 12.
- Köstel, J., J. Vanderborght, M. Javaux, A. Kemna, A. Binley, and H. Vereecken, 2009, Noninvasive 3-D Transport Characterization in a Sandy Soil Using ERT: 1. Investigating the Validity of ERT-derived Transport Parameters, *Vadose Zone J*, **8**, 711-722, doi: 10.2136/vzj2008.0027.
- Kuhr, M., 2000, Grobwurzelarchitektur in Abhängigkeit von Baumart, Alter, Standort und sozialer Stellung, Niedersächsische Staats-und Universitätsbibliothek Göttingen.
- LaBrecque, D. J., and S. H. Ward, 1991, Two-dimensional cross-borehole resistivity model fitting, *Investigations in Geophysics*, **5**, 51.
- LaBrecque, D. J., M. Miletto, W. Daily, A. Ramirez, and E. Owen, 1996, The effects of noise on Occam's inversion of resistivity tomography data, *Geophysics*, **61**, 538-548.

- Linnemann, V., 2001, Oral Presentation: ECHO: Ergebnisse zu den Bodenuntersuchungen und Planungen, edited.
- Looms, M. C., K. H. Jensen, A. Binley, and L. Nielsen, 2008, Monitoring unsaturated flow and transport using cross-borehole geophysical methods, *Vadose Zone Journal*, **7**, 227-237.
- Mallants, D., M. Vanclooster, M. Meddahi, and J. Feyen, 1994, Estimating Solute Transport in Undisturbed Soil Columns Using Time-Domain Reflectometry, *Journal of Contaminant Hydrology*, **17**, 91-109.
- Mauder, M., and T. Foken, 2004, *Documentation and instruction manual of eddy covariance software package TK2*, Department of Micrometeorology, University of Bayreuth, Bayreuth.
- Michot, D., Y. Benderitter, A. Dorigny, B. Nicoullaud, D. King, and A. Tabbagh, 2003, Spatial and temporal monitoring of soil water content with an irrigated corn crop cover using surface electrical resistivity tomography, *Water Resources Research*, **39**.
- Miller, C. R., P. S. Routh, T. R. Brosten, and J. P. McNamara, 2008, Application of time-lapse ERT imaging to watershed characterization, *Geophysics*, **73**, G7-G17.
- Moore, C., 1986, Frequency response corrections for eddy correlation systems, *Boundary-Layer Meteorology*, **37**, 17-35.
- Mualem, Y., and S. P. Friedman, 1991, Theoretical Prediction of Electrical-Conductivity in Saturated and Unsaturated Soil, *Water Resources Research*, **27**, 2771-2777.
- Nadler, A., 1982, Estimating the Soil-Water Dependence of the Electrical-Conductivity Soil Solution Electrical-Conductivity Bulk Soil Ratio, *Soil Science Society of America Journal*, **46**, 722-726.
- Nimmer, R. E., J. L. Osiensky, A. M. Binley, and B. C. Williams, 2008, Three-dimensional effects causing artifacts in two-dimensional, cross-borehole, electrical imaging, *Journal of Hydrology*, **359**, 59-70, doi: DOI 10.1016/j.jhydrol.2008.06.022.
- Nimmo, J. R., 2007, Simple predictions of maximum transport rate in unsaturated soil and rock, *Water Resources Research*, **43**, W05426, doi: 10.1029/2006wr005372.
- Nissen, H. H., T. P. A. Ferre, and P. Moldrup, 2003, Sample area of two- and three-rod time domain reflectometry probes, *Water Resources Research*, **39**(10), 1289, doi: 10.1029/2002wr001303.
- Noborio, K., R. G. Kachanoski, and C. S. Tan, 2006, Solute Transport Measurement Under Transient Field Conditions Using Time Domain Reflectometry, 10.2136/vzj2005.0019, *Vadose Zone Journal*, **5**, 412-418.

- Oldenburg, D. W., and Y. G. Li, 1999, Estimating depth of investigation in dc resistivity and IP surveys, *Geophysics*, **64**, 403-416.
- Olsen, P. A., A. Binley, S. Henry-Poulter, and W. Tych, 1999, Characterizing solute transport in undisturbed soil cores using electrical and X-ray tomographic methods, *Hydrological Processes*, **13**, 211-221.
- Paas, W., and J. Schalich, 2005, *Böden am Niederrhein*, edited, Geologischer Dienst NRW.
- Park, S., 1998, Fluid migration in the vadose zone from 3-D inversion of resistivity monitoring data, *Geophysics*, **63**, 41-51.
- Park, S. K., and G. P. Van, 1991, Inversion of Pole-Pole Data for 3-D Resistivity Structure beneath Arrays of Electrodes, *Geophysics*, **56**, 951-960.
- Rhoades, J. D., P. A. C. Raats, and R. J. Prather, 1976, Effects of Liquid-Phase Electrical-Conductivity, Water-Content, and Surface Conductivity on Bulk Soil Electrical-Conductivity, *Soil Science Society of America Journal*, **40**, 651-655.
- Rings, J., A. Scheuermann, K. Preko, and C. Hauck, 2008, Soil water content monitoring on a dike model using electrical resistivity tomography, *Near surface geophysics*, **6**, 123-132.
- Risler, P. D., J. M. Wraith, and H. M. Gaber, 1996, Solute transport under transient flow conditions estimated using time domain reflectometry, *Soil Science Society of America Journal*, **60**, 1297-1305.
- Robinson, D. A., C. S. Campbell, J. W. Hopmans, B. K. Hornbuckle, S. B. Jones, R. Knight, F. Ogden, J. Selker, and O. Wendroth, 2008, Soil moisture measurement for ecological and hydrological watershed-scale observatories: A review, *Vadose Zone Journal*, **7**, 358-389, doi: 10.2136/Vzj2007.0143.
- Schalich, J. (1972), *Bodenkarte von NRW 1:25000, 5004 Jülich*, Geologischer Dienst NRW.
- Schotanus, P., F. Nieuwstadt, and H. Bruin, 1983, Temperature measurement with a sonic anemometer and its application to heat and moisture fluxes, *Boundary-Layer Meteorology*, **26**, 81-93.
- Schwartz, B. F., M. E. Schreiber, and T. Yan, 2008, Quantifying field-scale soil moisture using electrical resistivity imaging, *Journal of Hydrology*, **362**, 234-246.
- Singha, K., and S. M. Gorelick, 2005, Saline tracer visualized with three-dimensional electrical resistivity tomography: Field-scale spatial moment analysis, *Water Resources Research*, **41**, W05023, doi: 10.1029/2004wr003460.

- Singha, K., and S. M. Gorelick, 2006, Effects of spatially variable resolution on field-scale estimates of tracer concentration from electrical inversions using Archie's law, *Geophysics*, **71**, G83-G91.
- Singha, K., F. D. Day-Lewis, and J. W. Lane, 2007, Geoelectrical evidence of bicontinuum transport in groundwater, *Geophysical Research Letters*, **34**, L12401, doi: 10.1029/2007gl030019.
- Slater, L., A. M. Binley, W. Daily, and R. Johnson, 2000, Cross-hole electrical imaging of a controlled saline tracer injection, *Journal of Applied Geophysics*, **44**, 85-102.
- Slater, L., A. Binley, R. Versteeg, G. Cassiani, R. Birken, and S. Sandberg, 2002, A 3D ERT study of solute transport in a large experimental tank, *Journal of Applied Geophysics*, **49**, 211-229.
- Tikhonov, A. N., and V. Y. Arsenin, 1977, *Solutions of Ill-Posed Problems*, W.H. Winston and Sons.
- Topp, G. C., J. L. Davis, and A. P. Annan, 1980, Electromagnetic Determination of Soil-Water Content - Measurements in Coaxial Transmission-Lines, *Water Resources Research*, **16**, 574-582.
- Toride, N., F. J. Leij, and M. T. van Genuchten, 1999, The CXTFIT Code for Estimating Transport Parameters from Laboratory or Field Tracer Experiments, U.S. Salinity Laboratory, Riverside, California, Research Report, **No. 137**.
- Van Dijk, A., A. F. Moene, and H. A. R. De Bruin, 2004, The principles of surface flux physics: theory, practice and description of the ECPACK library, Internal Report, Meteorology and Air Quality Group, Wageningen University, Wageningen.
- van Genuchten, M. T., and P. J. Wierenga, 1976, Mass-Transfer Studies in Sorbing Porous-Media .1. Analytical Solutions, *Soil Science Society of America Journal*, **40**, 473-480.
- Vanclooster, M., D. Mallants, J. Diels, and J. Feyen, 1993, Determining Local-Scale Solute Transport Parameters Using Time-Domain Reflectometry (TDR), *Journal of Hydrology*, **148**, 93-107.
- Vanclooster, M., D. Mallants, J. Vanderborght, J. Diels, J. Vanorshoven, and J. Feyen, 1995, Monitoring Solute Transport in a Multilayered Sandy Lysimeter Using Time-Domain Reflectometry, *Soil Science Society of America Journal*, **59**, 337-344.
- Vanderborght, J., M. Vanclooster, D. Mallants, J. Diels, and J. Feyen, 1996, Determining convective lognormal solute transport parameters from resident concentration data, *Soil Science Society of America Journal*, **60**, 1306-1317.
- Vanderborght, J., C. Gonzalez, M. Vanclooster, D. Mallants, and J. Feyen, 1997, Effects of soil type and water flux on solute transport, *Soil Science Society of America Journal*, **61**, 372-389.

- Vanderborght, J., A. Timmerman, and J. Feyen, 2000, Solute transport for steady-state and transient flow in soils with and without macropores, *Soil Science Society of America Journal*, **64**, 1305-1317.
- Vanderborght, J., A. Kemna, H. Hardelauf, and H. Vereecken, 2005, Potential of electrical resistivity tomography to infer aquifer transport characteristics from tracer studies: A synthetic case study, *Water Resources Research*, **41**, W06013, doi: 10.1029/2004wr003774.
- Vanderborght, J., and H. Vereecken, 2007, Review of dispersivities for transport modeling in soils, *Vadose Zone Journal*, **6**, 29-52.
- Vereecken, H., A. Kemna, H. Münch, A. Tillmann, and A. Verweerd, 2005, Aquifer characterization by geophysical methods, MG Anderson (ed.-in-chief) *Encyclopedia of hydrological sciences*, **4**, 2265–2284.
- Vereecken, H., J. A. Huisman, H. Boga, J. Vanderborght, J. A. Vrugt, and J. W. Hopmans, 2008, On the value of soil moisture measurements in vadose zone hydrology: A review, *Water Resources Research*, **44**, -, doi: 10.1029/2008wr006829.
- Vickers, D., and L. Mahrt, 1997, Quality control and flux sampling problems for tower and aircraft data, *Journal of Atmospheric and Oceanic Technology*, **14**, 512-526.
- Vogeler, I., B. E. Clothier, and S. R. Green, 1997, TDR estimation of the resident concentration of electrolyte in the soil solution, *Australian Journal of Soil Research*, **35**, 515-526.
- Ward, A. L., R. G. Kachanoski, and D. E. Elrick, 1994, Laboratory Measurements of Solute Transport Using Time-Domain Reflectometry, *Soil Science Society of America Journal*, **58**, 1031-1039.
- Webb, E. K., G. I. Pearman, and R. Leuning, 1980, Correction of Flux Measurements for Density Effects Due to Heat and Water-Vapor Transfer, *Quarterly Journal of the Royal Meteorological Society*, **106**, 85-100.
- Zhou, B., and S. A. Greenhalgh, 2000, Cross-hole resistivity tomography using different electrode configurations, *Geophysical Prospecting*, **48**, 887-912.
- Zhou, B., and T. Dahlin, 2003, Properties and effects of measurement errors on 2D resistivity imaging surveying, *Near Surface Geophysics*, **1**, 105-117.
- Zhou, Q. Y., J. Shimada, and A. Sato, 2001, Three-dimensional spatial and temporal monitoring of soil water content using electrical resistivity tomography, *Water Resources Research*, **37**, 273-285.
- Zhou, Q. Y., J. Shimada, and A. Sato, 2002, Temporal variations of the three-dimensional rainfall infiltration process in heterogeneous soil, *Water Resources Research*, **38**.

1. **Einsatz von multispektralen Satellitenbilddaten in der Wasserhaushalts- und Stoffstrommodellierung – dargestellt am Beispiel des Rureinzugsgebietes**
von C. Montzka (2008), XX, 238 Seiten
ISBN: 978-3-89336-508-1
2. **Ozone Production in the Atmosphere Simulation Chamber SAPHIR**
by C. A. Richter (2008), XIV, 147 pages
ISBN: 978-3-89336-513-5
3. **Entwicklung neuer Schutz- und Kontaktierungsschichten für Hochtemperatur-Brennstoffzellen**
von T. Kiefer (2008), 138 Seiten
ISBN: 978-3-89336-514-2
4. **Optimierung der Reflektivität keramischer Wärmedämmschichten aus Yttrium-teilstabilisiertem Zirkoniumdioxid für den Einsatz auf metallischen Komponenten in Gasturbinen**
von A. Stuke (2008), X, 201 Seiten
ISBN: 978-3-89336-515-9
5. **Lichtstreuende Oberflächen, Schichten und Schichtsysteme zur Verbesserung der Lichteinkopplung in Silizium-Dünnschichtsolarzellen**
von M. Berginski (2008), XV, 171 Seiten
ISBN: 978-3-89336-516-6
6. **Politiksznarien für den Klimaschutz IV – Szenarien bis 2030**
hrsg.von P. Markewitz, F. Chr. Matthes (2008), 376 Seiten
ISBN 978-3-89336-518-0
7. **Untersuchungen zum Verschmutzungsverhalten rheinischer Braunkohlen in Kohledampferzeugern**
von A. Schlüter (2008), 164 Seiten
ISBN 978-3-89336-524-1
8. **Inorganic Microporous Membranes for Gas Separation in Fossil Fuel Power Plants**
by G. van der Donk (2008), VI, 120 pages
ISBN: 978-3-89336-525-8
9. **Sinterung von Zirkoniumdioxid-Elektrolyten im Mehrlagenverbund der oxidkeramischen Brennstoffzelle (SOFC)**
von R. Mücke (2008), VI, 165 Seiten
ISBN: 978-3-89336-529-6
10. **Safety Considerations on Liquid Hydrogen**
by K. Verfondern (2008), VIII, 167 pages
ISBN: 978-3-89336-530-2

11. **Kerosinreformierung für Luftfahrtanwendungen**
von R. C. Samsun (2008), VII, 218 Seiten
ISBN: 978-3-89336-531-9
12. **Der 4. Deutsche Wasserstoff Congress 2008 – Tagungsband**
hrsg. von D. Stolten, B. Emonts, Th. Grube (2008), 269 Seiten
ISBN: 978-3-89336-533-3
13. **Organic matter in Late Devonian sediments as an indicator for environmental changes**
by M. Kloppisch (2008), XII, 188 pages
ISBN: 978-3-89336-534-0
14. **Entschwefelung von Mitteldestillaten für die Anwendung in mobilen Brennstoffzellen-Systemen**
von J. Latz (2008), XII, 215 Seiten
ISBN: 978-3-89336-535-7
15. **RED-IMPACT**
Impact of Partitioning, Transmutation and Waste Reduction Technologies on the Final Nuclear Waste Disposal
SYNTHESIS REPORT
ed. by W. von Lensa, R. Nabbi, M. Rossbach (2008), 178 pages
ISBN 978-3-89336-538-8
16. **Ferritic Steel Interconnectors and their Interactions with Ni Base Anodes in Solid Oxide Fuel Cells (SOFC)**
by J. H. Froitzheim (2008), 169 pages
ISBN: 978-3-89336-540-1
17. **Integrated Modelling of Nutrients in Selected River Basins of Turkey**
Results of a bilateral German-Turkish Research Project
project coord. M. Karpuzcu, F. Wendland (2008), XVI, 183 pages
ISBN: 978-3-89336-541-8
18. **Isotopengeochemische Studien zur klimatischen Ausprägung der Jüngerer Dryas in terrestrischen Archiven Eurasiens**
von J. Parplies (2008), XI, 155 Seiten, Anh.
ISBN: 978-3-89336-542-5
19. **Untersuchungen zur Klimavariabilität auf dem Tibetischen Plateau - Ein Beitrag auf der Basis stabiler Kohlenstoff- und Sauerstoffisotope in Jahrringen von Bäumen waldgrenznaher Standorte**
von J. Griessinger (2008), XIII, 172 Seiten
ISBN: 978-3-89336-544-9

20. **Neutron-Irradiation + Helium Hardening & Embrittlement Modeling of 9%Cr-Steels in an Engineering Perspective (HELENA)**
by R. Chaouadi (2008), VIII, 139 pages
ISBN: 978-3-89336-545-6
21. **in Bearbeitung**
22. **Verbundvorhaben APAWAGS (AOEV und Wassergenerierung) – Teilprojekt: Brennstoffreformierung – Schlussbericht**
von R. Peters, R. C. Samsun, J. Pasel, Z. Porš, D. Stolten (2008), VI, 106 Seiten
ISBN: 978-3-89336-547-0
23. **FREEVAL**
Evaluation of a Fire Radiative Power Product derived from Meteosat 8/9 and Identification of Operational User Needs
Final Report
project coord. M. Schultz, M. Wooster (2008), 139 pages
ISBN: 978-3-89336-549-4
24. **Untersuchungen zum Alkaliverhalten unter Oxycoal-Bedingungen**
von C. Weber (2008), VII, 143, XII Seiten
ISBN: 978-3-89336-551-7
25. **Grundlegende Untersuchungen zur Freisetzung von Spurstoffen, Heißgaschemie, Korrosionsbeständigkeit keramischer Werkstoffe und Alkalirückhaltung in der Druckkohlenstaubfeuerung**
von M. Müller (2008), 207 Seiten
ISBN: 978-3-89336-552-4
26. **Analytik von ozoninduzierten phenolischen Sekundärmetaboliten in *Nicotiana tabacum* L. cv Bel W3 mittels LC-MS**
von I. Koch (2008), III, V, 153 Seiten
ISBN 978-3-89336-553-1
27. **IEF-3 Report 2009. Grundlagenforschung für die Anwendung**
(2009), ca. 230 Seiten
ISBN: 978-3-89336-554-8
28. **Influence of Composition and Processing in the Oxidation Behavior of MCrAlY-Coatings for TBC Applications**
by J. Toscano (2009), 168 pages
ISBN: 978-3-89336-556-2
29. **Modellgestützte Analyse signifikanter Phosphorbelastungen in hessischen Oberflächengewässern aus diffusen und punktuellen Quellen**
von B. Tetzlaff (2009), 149 Seiten
ISBN: 978-3-89336-557-9

30. **Nickelreaktivlot / Oxidkeramik – Fügungen als elektrisch isolierende Dichtungskonzepte für Hochtemperatur-Brennstoffzellen-Stacks**
von S. Zügner (2009), 136 Seiten
ISBN: 978-3-89336-558-6
31. **Langzeitbeobachtung der Dosisbelastung der Bevölkerung in radioaktiv kontaminierten Gebieten Weißrusslands – Korma-Studie**
von H. Dederichs, J. Pillath, B. Heuel-Fabianek, P. Hill, R. Lennartz (2009),
Getr. Pag.
ISBN: 978-3-89336-532-3
32. **Herstellung von Hochtemperatur-Brennstoffzellen über physikalische Gasphasenabscheidung**
von N. Jordán Escalona (2009), 148 Seiten
ISBN: 978-3-89336-532-3
33. **Real-time Digital Control of Plasma Position and Shape on the TEXTOR Tokamak**
by M. Mitri (2009), IV, 128 pages
ISBN: 978-3-89336-567-8
34. **Freisetzung und Einbindung von Alkalimetallverbindungen in kohle-befeuerten Kombikraftwerken**
von M. Müller (2009), 155 Seiten
ISBN: 978-3-89336-568-5
35. **Kosten von Brennstoffzellensystemen auf Massenbasis in Abhängigkeit von der Absatzmenge**
von J. Werhahn (2009), 242 Seiten
ISBN: 978-3-89336-569-2
36. **Einfluss von Reoxidationszyklen auf die Betriebsfestigkeit von anodengestützten Festoxid-Brennstoffzellen**
von M. Ettler (2009), 138 Seiten
ISBN: 978-3-89336-570-8
37. **Großflächige Plasmaabscheidung von mikrokristallinem Silizium für mikromorphe Dünnschichtsolarmodule**
von T. Kilper (2009), XVII, 154 Seiten
ISBN: 978-3-89336-572-2
38. **Generalized detailed balance theory of solar cells**
by T. Kirchartz (2009), IV, 198 pages
ISBN: 978-3-89336-573-9
39. **The Influence of the Dynamic Ergodic Divertor on the Radial Electric Field at the Tokamak TEXTOR**
von J. W. Coenen (2009), xii, 122, XXVI pages
ISBN: 978-3-89336-574-6

40. **Sicherheitstechnik im Wandel Nuklearer Systeme**
von K. Nünighoff (2009), viii, 215 Seiten
ISBN: 978-3-89336-578-4
41. **Pulvermetallurgie hochporöser NiTi-Legierungen für Implantat- und Dämpfungsanwendungen**
von M. Köhl (2009), XVII, 199 Seiten
ISBN: 978-3-89336-580-7
42. **Einfluss der Bondcoatzusammensetzung und Herstellungsparameter auf die Lebensdauer von Wärmedämmschichten bei zyklischer Temperaturbelastung**
von M. Subanovic (2009), 188, VI Seiten
ISBN: 978-3-89336-582-1
43. **Oxygen Permeation and Thermo-Chemical Stability of Oxygen Permeation Membrane Materials for the Oxyfuel Process**
by A. J. Ellett (2009), 176 pages
ISBN: 978-3-89336-581-4
44. **Korrosion von polykristallinem Aluminiumoxid (PCA) durch Metalljodidschmelzen sowie deren Benetzungseigenschaften**
von S. C. Fischer (2009), 148 Seiten
ISBN: 978-3-89336-584-5
45. **IEF-3 Report 2009. Basic Research for Applications**
(2009), 217 Seiten
ISBN: 978-3-89336-585-2
46. **Verbundvorhaben ELBASYS (Elektrische Basissysteme in einem CFK-Rumpf) - Teilprojekt: Brennstoffzellenabgase zur Tankinertisierung - Schlussbericht**
von R. Peters, J. Latz, J. Pasel, R. C. Samsun, D. Stolten
(2009), xi, 202 Seiten
ISBN: 978-3-89336-587-6
47. **Aging of ¹⁴C-labeled Atrazine Residues in Soil: Location, Characterization and Biological Accessibility**
by N. D. Jablonowski (2009), IX, 104 pages
ISBN: 978-3-89336-588-3
48. **Entwicklung eines energetischen Sanierungsmodells für den europäischen Wohngebäudesektor unter dem Aspekt der Erstellung von Szenarien für Energie- und CO₂ - Einsparpotenziale bis 2030**
von P. Hansen (2009), XXII, 281 Seiten
ISBN: 978-3-89336-590-6

49. **Reduktion der Chromfreisetzung aus metallischen Interkonnektoren für Hochtemperaturbrennstoffzellen durch Schutzschichtsysteme**
von R. Trebbels (2009), iii, 135 Seiten
ISBN: 978-3-89336-591-3

50. **Bruchmechanische Untersuchung von Metall / Keramik-Verbundsystemen für die Anwendung in der Hochtemperaturbrennstoffzelle**
von B. Kuhn (2009), 118 Seiten
ISBN: 978-3-89336-592-0

51. **Wasserstoff-Emissionen und ihre Auswirkungen auf den arktischen Ozonverlust**
Risikoanalyse einer globalen Wasserstoffwirtschaft
von T. Feck (2009), 180 Seiten
ISBN: 978-3-89336-593-7

52. **Development of a new Online Method for Compound Specific Measurements of Organic Aerosols**
by T. Hohaus (2009), 156 pages
ISBN: 978-3-89336-596-8

53. **Entwicklung einer FPGA basierten Ansteuerungselektronik für Justageeinheiten im Michelson Interferometer**
von H. Nöldgen (2009), 121 Seiten
ISBN: 978-3-89336-599-9

54. **Observation – and model – based study of the extratropical UT/LS**
by A. Kunz (2010), xii, 120, xii pages
ISBN: 978-3-89336-603-3

55. **Herstellung polykristalliner Szintillatoren für die Positronen-Emissions-Tomographie (PET)**
von S. K. Karim (2010), VIII, 154 Seiten
ISBN: 978-3-89336-610-1

56. **Kombination eines Gebäudekondensators mit H₂-Rekombinatorelementen in Leichtwasserreaktoren**
von S. Kelm (2010), vii, 119 Seiten
ISBN: 978-3-89336-611-8

57. **Plant Leaf Motion Estimation Using A 5D Affine Optical Flow Model**
by T. Schuchert (2010), X, 143 pages
ISBN: 978-3-89336-613-2

58. **Tracer-tracer relations as a tool for research on polar ozone loss**
by R. Müller (2010), 116 pages
ISBN: 978-3-89336-614-9

59. **Sorption of polycyclic aromatic hydrocarbon (PAH) to Yangtze River sediments and their components**
by J. Zhang (2010), X, 109 pages
ISBN: 978-3-89336-616-3
60. **Weltweite Innovationen bei der Entwicklung von CCS-Technologien und Möglichkeiten der Nutzung und des Recyclings von CO₂**
Studie im Auftrag des BMWi
von W. Kuckshinrichs et al. (2010), X, 139 Seiten
ISBN: 978-3-89336-617-0
61. **Herstellung und Charakterisierung von sauerstoffionenleitenden Dünnschichtmembranstrukturen**
von M. Betz (2010), XII, 112 Seiten
ISBN: 978-3-89336-618-7
62. **Politiksznarien für den Klimaschutz V – auf dem Weg zum Strukturwandel, Treibhausgas-Emissionsszenarien bis zum Jahr 2030**
hrsg. von P. Hansen, F. Chr. Matthes (2010), 276 Seiten
ISBN: 978-3-89336-619-4
63. **Charakterisierung Biogener Sekundärer Organischer Aerosole mit Statistischen Methoden**
von C. Spindler (2010), iv, 163 Seiten
ISBN: 978-3-89336-622-4
64. **Stabile Algorithmen für die Magnetotomographie an Brennstoffzellen**
von M. Wannert (2010), ix, 119 Seiten
ISBN: 978-3-89336-623-1
65. **Sauerstofftransport und Degradationsverhalten von Hochtemperaturmembranen für CO₂-freie Kraftwerke**
von D. Schlehuber (2010), VII, 139 Seiten
ISBN: 978-3-89336-630-9
66. **Entwicklung und Herstellung von foliengegossenen, anodengestützten Festoxidbrennstoffzellen**
von W. Schafbauer (2010), VI, 164 Seiten
ISBN: 978-3-89336-631-6
67. **Disposal strategy of proton irradiated mercury from high power spallation sources**
by S. Chiriki (2010), xiv, 124 pages
ISBN: 978-3-89336-632-3
68. **Oxides with polyatomic anions considered as new electrolyte materials for solid oxide fuel cells (SOFCs)**
by O. H. Bin Hassan (2010), vii, 121 pages
ISBN: 978-3-89336-633-0

69. **Von der Komponente zum Stack: Entwicklung und Auslegung von HT-PEFC-Stacks der 5 kW-Klasse**
von A. Bendzulla (2010), IX, 203 Seiten
ISBN: 978-3-89336-634-7
70. **Satellitengestützte Schwerewellenmessungen in der Atmosphäre und Perspektiven einer zukünftigen ESA Mission (PREMIER)**
von S. Höfer (2010), 81 Seiten
ISBN: 978-3-89336-637-8
71. **Untersuchungen der Verhältnisse stabiler Kohlenstoffisotope in atmosphärisch relevanten VOC in Simulations- und Feldexperimenten**
von H. Spahn (2010), IV, 210 Seiten
ISBN: 978-3-89336-638-5
72. **Entwicklung und Charakterisierung eines metallischen Substrats für nanostrukturierte keramische Gastrennmembranen**
von K. Brands (2010), vii, 137 Seiten
ISBN: 978-3-89336-640-8
73. **Hybridisierung und Regelung eines mobilen Direktmethanol-Brennstoffzellen-Systems**
von J. Chr. Wilhelm (2010), 220 Seiten
ISBN: 978-3-89336-642-2
74. **Charakterisierung perowskitischer Hochtemperaturmembranen zur Sauerstoffbereitstellung für fossil gefeuerte Kraftwerksprozesse**
von S.A. Möbius (2010) III, 208 Seiten
ISBN: 978-3-89336-643-9
75. **Characterization of natural porous media by NMR and MRI techniques: High and low magnetic field studies for estimation of hydraulic properties**
by L.-R. Stingaciu (2010), 96 pages
ISBN: 978-3-89336-645-3
76. **Hydrological Characterization of a Forest Soil Using Electrical Resistivity Tomography**
by Chr. Oberdörster (2010), XXI, 151 pages
ISBN: 978-3-89336-647-7

Energie & Umwelt / Energy & Environment
Band / Volume 76
ISBN 978-3-89336-647-7

